NANYANG TECHNOLOGICAL UNIVERSITY

STUDY OF NANO-INCLUSIONS ON THE THERMOELECTRIC PROPERTIES OF COBALT TRIANTIMONIDE-BASED NANOCOMPOSITES

Yang Lan

School of Materials Science and Engineering

2012

Study of Nano-inclusions on the Thermoelectric Properties of Cobalt Triantimonide-based Nanocomposites

Yang Lan

School of Materials Science and Engineering

A thesis submitted to the Nanyang Technological University
in partial fulfillment of the requirement for the degree of
Doctor of Philosophy

2012

Acknowledgement

I am indeed grateful to my supervisor, Professor Hng Huey Hoon, for the vision, guidance and independence she provides to me, and for her patience and encouragement throughout my candidature. Thanks to School of Materials Science and Engineering for providing such a good research environment. Thanks to my thesis advisory committee members, Prof. Ma Jan and Prof. Lim Geok Kieng for their invaluable suggestions. I also want to thank DSO (Singapore) for their funding support on my project. I owe my appreciation to Prof. Yan Qingyu for his valuable discussion and guidance in my experiments. Thanks also go to Ms Han Mandi and Dr Liu Qing for their help on the characterizations.

I am also thankful for the other research staffs / students from MSE, Dr. Cheng Hao, Dr. Yang Kai, Dr. Sun Ting, Dr. Du Zehui, Dr. Huang Hui, Dr. Gong Hua, Dr. Zhang Jian, Dr Jiang Hao, Zhu Jixin, Zhou Wenwen, Chen Jing, Zhao Weiyun, Shi Wenhui, Sim Daohao, Lin Mengfang, Song Xiaochao, Shen Yiqiang, for their help, discussion and friendship. I would also like to express my appreciation to the technicians in MSE for their support and assistance.

Last but not least, I would like to thank my husband, Shen Hongliang, for his encouragement and assistance during my writing of this thesis. I am always in debt to my parents, for their continuous support and understanding.

Abstract

Thermoelectric materials can convert heat into electricity and vice versa for use as power generator and cooler. Skutterudite, CoSb$_3$-based materials are particularly promising thermoelectric (TE) material used in the intermediate temperature range (600～900K), due to its reasonably large Seebeck coefficient (α) and high electrical conductivity (σ), resulting in high power factor ($\alpha^2\sigma$), which are comparable to the state-of-art TE materials. However, its thermal conductivity (κ) is too high to make it an effective TE material. In this work, nanocomposite approach, in which nanoscaled structures (nano-inclusions) are incorporated into the matrix of a conventional micron-sized material, is attempted in order to reduce its thermal conductivity and improve the overall thermoelectric properties of skutterudite. The effects of nano-inclusion on the electrical properties of nanocomposites were also investigated.

The work started with the synthesis of p-type pure CoSb$_3$ nanoparticles via a modified polyol process. Systematic experimental results indicated a high purity of CoSb$_3$ phase could be obtained at a relatively low temperature of 195 °C for 15 mins. N-type Ni-doped CoSb$_3$ nanoparticles were also synthesized using the same reaction conditions with the doping amount optimized. It was found that the Ni$_{1.25}$Co$_{6.75}$Sb$_{24}$ sample possessed the maximum power factor, and the highest *ZT* value of 0.33 was achieved at around 480 °C which is much higher than that of undoped CoSb$_3$ of 0.067 at around 450 °C. The nanoparticles obtained were also used as dispersants to prepare both p-type and n-type nanocomposites.

The p-type nanocomposite with undoped CoSb$_3$ acting both as nano-inclusions and micron-sized matrix were prepared. The results showed that both the total and lattice thermal conductivity were reduced after introducing nano-inclusions due to its high density of grain boundaries. Besides thermal conductivity, the electrical properties of the

nanocomposite were also found to be improved by the nano-inclusions due to the different electrical properties of these two phases, where the nano-inclusions have a much higher carrier concentration than that of micron-sized matrix. Furthermore, another two types of p-type nanocomposites whose nano-inclusions have much lower or comparable carrier concentration than that of micron-sized matrix were prepared and the effects of these nano-inclusions on both thermal and electrical properties were investigated. The results indicated that nanostructures with higher carrier concentration and lower thermal conductivity than that of micron-sized matrix are the most suitable for use as nano-inclusions. The most *ZT* value improvement happened in the nanocomposite with undoped $CoSb_3$ acting both as nano-inclusion and micron-sized matrix. Comparing with the micron-sized matrix, the *ZT* value of nanocomposite with 10wt% of nano-inclusions is nearly doubled as compared to the sample without nano-inclusions.

Based on the results of p-type nanocomposites, n-type nanocomposites were also prepared and $Ni_{1.25}Co_{6.25}Sb_{24}$ with the highest carrier concentration among the Ni-doped $CoSb_3$ nanostructures was chosen as the nano-inclusions. The *ZT* value reached a value of 0.71 at 450 °C for the nanocomposite sample with 10wt% nano-inclusions which is the highest figure-of-merit of unfilled $CoSb_3$ reported so far.

In conclusion, nanocomposite approach has been proven to be a promising way to improve the thermoelectric properties of $CoSb_3$-based materials. The results of p-type and n-type nancomposites are in a good agreement that nanostructures with higher carrier concentration and lower thermal conductivity than that of micron-sized matrix are effective in improving the overall thermoelectric properties of nanocomposites.

Table of Contents

Chapter 1
Introduction

1.1 Background

The unprecedented energy crisis and the accompanying detrimental environmental consequences placed great emphasis on renewable and sustainable energy materials. More than 60% of the energy generated from primary energy sources is lost during the heat conversion process. Thermoelectric (TE) devices can reliably convert heat into useful electricity and is one of the research focuses aimed at improving sustainability. The basic idea is to use TE modules to convert part of the waste heat back into useful electricity, thereby improving the overall energy efficiency. They are noiseless and vibration free as there are no mechanical moving parts, and small in size as well as lightweight [1]. Heat can come either from the Sun or waste heat generated by a variety of sources including power plants, chemical plants, or automobiles. As power generators, the net result is to be more fuel efficient in the case of heat recovery from the exhaust pipe of cars. Besides functioning as a power generator, the TE can act in the reverse, i.e. as refrigerator. As refrigerators, they are environmentally friendly as CFC and other refrigerant gas are not used [2,3]. Due to these advantages, TE devices have found a large range of potential applications. The main problem with today's TE materials is poor efficiency leading their narrow application in niche markets where small size and light weight are more important than the performance and cost. Therefore, the design of more efficient thermoelectric materials is designated as a priority research direction [4].

The efficiency of a TE material is determined by the dimensionless figure of merit, ZT, where $ZT=\alpha^2\sigma T/\kappa$ and α is the Seebeck coefficient, σ is the electrical conductivity, T is the absolute temperature in Kelvin and κ is the total thermal conductivity. The total thermal conductivity is often approximately described as $\kappa = \kappa_l + \kappa_e$, where κ_l is the heat conducted by phonons (lattice vibration) and κ_e is the heat conducted by mobile electrons [5]. Over the past ten years or so, intensive research efforts worldwide has identified several novel TE materials that, with further development, could bring about the breakthrough and open up new horizons for a widespread use of thermoelectricity. Meanwhile, tremendous efforts are also focused on improving existing TE materials through various methods either to reduce the thermal conductivity or to increase the electrical conductivity and Seebeck coefficient.

As proposed by Slack [6,7], a good thermoelectric material should follow the phonon-glass electron-crystal (PGEC) model, i.e. the thermal conductivity of the materials is as low as a glass, and electrical conductivity is as high as a perfect single crystal. Promising PGEC bulk TE materials include materials from the skutterudites, clathrates, half-Heusler alloys, Zn_4Sb_3 alloys and Chalcogenides families. Among these TE materials, skutterudites lead the way in the temperature range between 600 and 900 K [8]. Of the different types of skutterudites, $CoSb_3$-based materials have attracted the greatest attention due to their promising electrical properties, i.e. large Seebeck coefficient and high electrical conductivity [9]. However, the lattice thermal conductivity of $CoSb_3$-based materials is relatively high as compared to other TE materials. Hence, the aim of this work is on the reduction of lattice thermal conductivity of $CoSb_3$-based materials.

Many methods have been proposed to reduce the lattice thermal conductivity of skutterudite such as filling, doping, nanostructuring and preparation of nanocomposites with the ultimate aim to improve the overall thermoelectric properties of $CoSb_3$. Among these methods, nanocomposite approach attracts a lot of research attentions and many TE nanocomposites have been reported, such as PbTe nanocomposites with coated nanostructures on the surface of the bulk [10], Bi_2Te_3 nanotube-containing nanocomposites [11]. All these nanocomposites have a reduced thermal conductivity, and show great potential in improving the TE properties.

1.2 Objective

Due to the fact that $CoSb_3$ possesses good electrical properties but poor thermal conductivity, the main objective of this work is to decrease the thermal conductivity of $CoSb_3$-based skutterudites and improve the overall thermoelectric properties through nanocomposite approach in which nano-scaled structures are incorporated into the matrix of a conventional micron-sized material. Both p- and n-type $CoSb_3$-based nancomposites will be prepared. The electrical properties difference between the nano-inclusion and micron-sized matrix can also play an important role on the final electrical properties of the nanocomposite samples. In order to study this effect, three types of nanocomposites whose nano-inclusion possessing much higher, lower or comparable carrier concentration with that of micron-sized matrix are prepared for comparison. Finally, a general rule for the choice of nano-inclusion from both thermal and electrical properties considerations will be proposed.

1.3 Organization of the thesis

There are seven chapters in this report.

In Chapter 1, the background of this project is depicted, along with the objective of this work. And the organization of this thesis outlined.

Chapter 2 gives the fundamental theories of thermoelectric materials. An introduction to skutterudites is also included. Finally, the possible approaches to improve the thermoelectric properties of $CoSb_3$-based skutterudites are reviewed.

In Chapter 3, the detailed synthesis procedures and characterization methods of $CoSb_3$-based nanostructures and nanocomposites are presented.

In Chapter 4, the synthesis of p-type undoped $CoSb_3$ and n-type Ni-doped $CoSb_3$ nano-particles by polyol method are presented. In this chapter, the reaction conditions such as temperature and dwelling time are optimized. For the n-type Ni-doped $CoSb_3$ nano-particles, the effects of doping on the electrical and thermal properties are investigated. The as-synthesized nano-particles will be used as nano-inclusion in Chapter 5 and Chapter 6.

Chapter 5 details the investigation of three types of p-type $CoSb_3$-based nanocomposites with various nano-inclusions and micron-sized matrix. The effect of nano-inclusion on the final electrical properties of nanocomposite samples is investigated by choosing nano-inclusions with carrier concentration much higher (undoped nanostructured $CoSb_3$) and lower (nanostructured ZrO_2) than the micron-sized matrix (undoped micron-sized $CoSb_3$). The case of nano-inclusions (undoped nanostructured $CoSb_3$) and micron-sized matrix (micron-structured filled $CoSb_3$) which have comparable carrier concentration are also studied. Besides electrical properties, the effect of nano-inclusion on the thermal conductivity of these three types of nanocomposite samples is also analyzed. And a general rule for the choice of nanocomposite is proposed.

In Chapter 6, n-type nanocomposites are prepared. Based on the experimental results in Chapter 5, $Ni_{1.25}Co_{6.75}Sb_{24}$ which has the highest carrier concentration among the Ni-doped $CoSb_3$ nanostructures is chosen as nano-inclusion. The effects of nano-inclusion on the final electrical as well as thermal properties of nanocomposites are discussed.

Chapter 7 summarises the results achieved in this thesis. Future work will also be proposed.

Chapter 2
Literature review

2.1 Thermoelectric phenomena

2.1.1 Seebeck effects

Thermoelectric materials have been extensively researched and developed since late 1950s. Thermoelectricity was first discovered by Thomas Seebeck in the early 1800s [12-14]. He observed that when two dissimilar materials a and b are joined together and the junctions held at different temperature (T_h and T_c), a voltage difference (ΔV) that is proportional to the temperature difference ($\Delta T= T_h- T_c$) will result. As shown in Figure 2.1-1, the ratio of the voltage developed to the temperature gradient ($\Delta V/\Delta T$) is related to an intrinsic property of the material known as the Seebeck coefficient, $\alpha_{ab}=\alpha_a-\alpha_b$, i.e.

$$\Delta V = \alpha_{ab} \times \Delta T \qquad (2.1\text{-}1)$$

The Seebeck coefficient is very low for metals (only a few $\mu V/K$) but much larger for semiconductors (typically several hundred $\mu V/K$) [15].

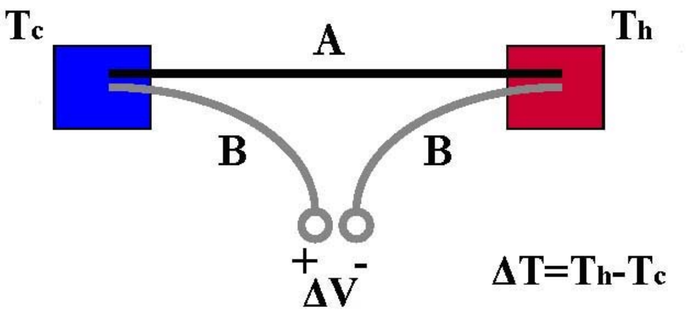

Figure 2.1-1: Schematic diagram of Seebeck effect.

The Seebeck effect is mainly caused by charge carrier diffusion. Hot carriers diffuse from the hot end to the cold end and the cold carriers diffuse from the cold end to the hot end when one end of a conductor is at a different temperature than the other. The illustration is as shown in Figure 2.1-2.

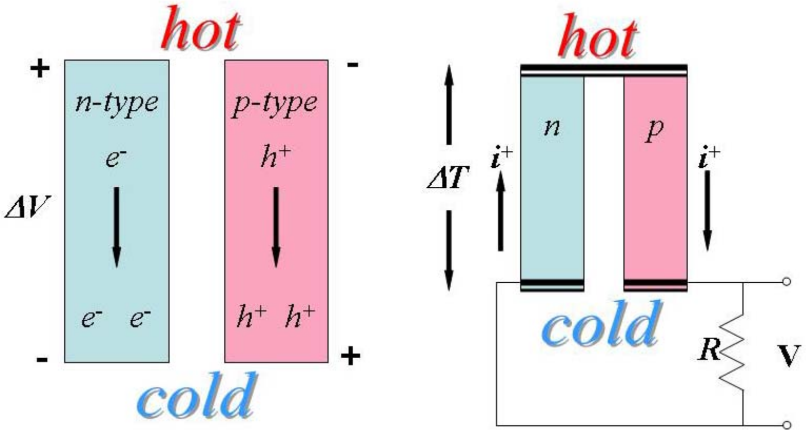

Figure 2.1-2: Illustration of the causes of Seebeck effect.

2.1.2 Peltier effects

A few years after the discovery of Seebeck effect, a related effect— the Peltier effect, was discovered. Peltier showed that when an electrical current is passed through the junction of two dissimilar materials, heat is either absorbed or rejected at the junction, depending on the direction of the current (shown in Figure 2.1-3). The Peltier effect reflects the fact that when carriers flow through a conductor, they also carry heat. The heat current Q is proportional to the charge current I and the proportional constant Π_{ab} called the Peltier coefficient, the unit of Π is V [5,7,12-14]:

$$Q = \Pi_{ab} \times I \qquad (2.1\text{-}2)$$

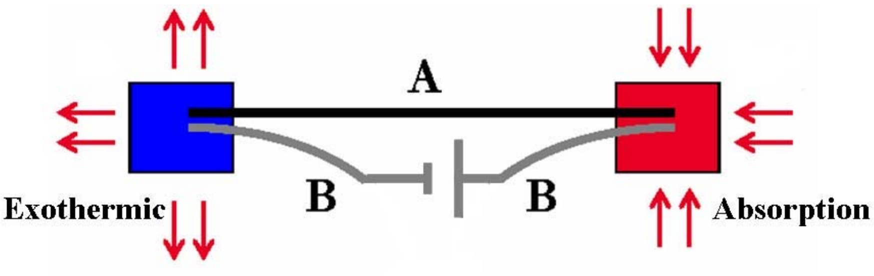

Figure 2.1-3: Schematic diagram of Peltier effect.

2.1.3 Thomson effect

This phenomenon was first discovered in 1854 by William Thomson and later by Lord Kelvin. For the Thomson effect, consider a material with a current flowing through it and a temperature gradient applied to it. In this situation, thermal energy is generated (or absorbed) all along the sample. The reason for this is similar to the reasoning behind the Peltier effect, if one realizes that the Seebeck coefficient for this material depends on temperature. This means that the Seebeck coefficient is different at different places along the sample. So the sample can be thought of as a series of many small Peltier junctions, each of which is generating (or absorbing) heat. The Thomson effect does not occur in a current-carrying conductor which is initially at uniform temperature. The rate of generating (or absorbing) heat q is proportional to the charge current I and the temperature gradient. The proportional constant β which have the same unit as Seebeck coefficient (α), is called the Thomson coefficient [5,7]:

$$q = \beta \times I \times \Delta T \qquad (2.1\text{-}3)$$

When the charge current and the temperature gradient have the same direction, the material absorbs heat and β has a positive value. Otherwise, β is negative. The illustration of Thomson effect is shown in Figure 2.1-4.

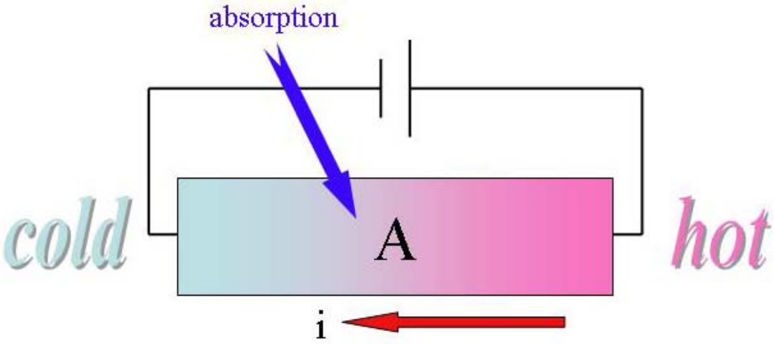

Figure 1.2-4: Schematic diagram of Thomson effect.

2.1.4 Relations of thermoelectric effects

The Seebeck, Peltier and Thomson effect are related by the following equations [5,7], where T is the absolute temperature:

$$\Pi = \alpha \times T \qquad (2.1\text{-}4)$$

$$\frac{d\alpha_{ab}}{dT} = \frac{\beta_a - \beta_b}{T} \qquad (2.1\text{-}5)$$

2.2 Evaluation of thermoelectric device

2.2.1 Efficiency of thermoelectric device

A typical thermoelectric cooler based on the Peltier effect is shown in Figure 2.2-1(a). P-type and n-type semiconductor elements are interconnected thermally in parallel and electrically in series. In a Peltier cooler, the external circuit is a D.C. power supply, which drives the electric current (I) and heat flow (Q), thereby cooling the top surface due to the Peltier effect. Energy conversion based on the Seebeck effect for power generation is as shown in Figure 2.2-1(b). A thermoelectric generator uses heat flow across a temperature gradient to power an electric load through the external circuit. The temperature difference provides the voltage ($V=\alpha\Delta T$) from the Seebeck effect while the heat flow drives the electrical current, which determines the power output. Figure 2.2-1(c) shows a practical device, which contains many thermoelectric couples which consist of n-type (containing free electrons) and p-type (containing free holes) thermoelectric elements wired electrically in series and thermally in parallel. In both devices, the heat rejected must be removed through a heat sink to maintain the temperature gradient.

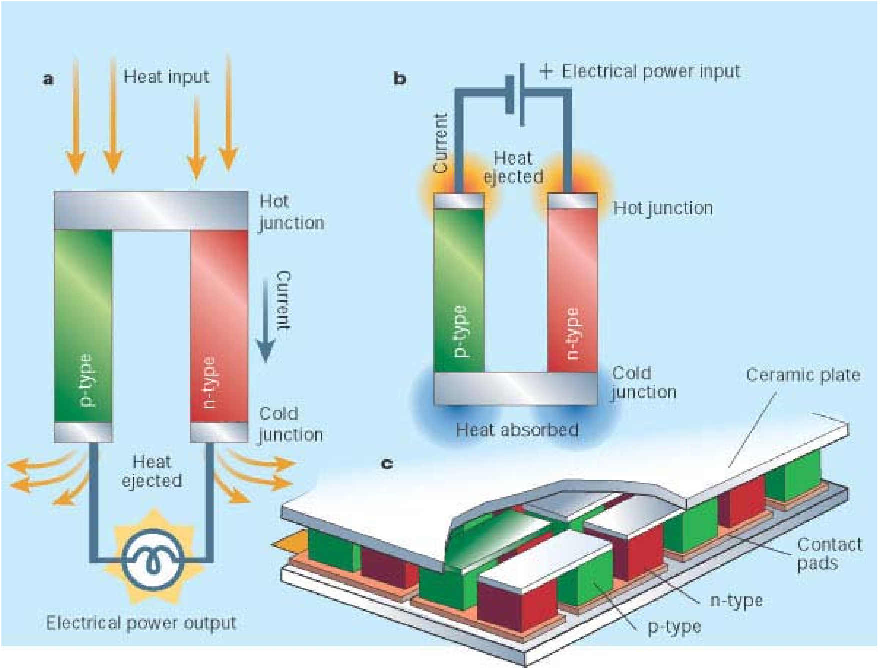

Figure 2.2-1: Illustration of the thermoelectric devices: power generator (a), cooler (b), actual device (c) [16].

In general, the thermoelectric conversion efficiency depends on the figure-of-merit, ZT as well as the temperature difference between the two ends of the TE device. The generating efficiency can be express as [5,7]:

$$\eta_{TEG} = \frac{T_h - T_c}{T_h} \cdot \frac{\sqrt{1+Z_{ab}T} - 1}{\sqrt{1+Z_{ab}T} + T_c/T_h} \qquad (2.2\text{-}1)$$

And the device figure of merit as [5,7]:

$$Z_{ab}T = \frac{\alpha_{ab}^2 T}{(\sqrt{\rho_a \kappa_a} + \sqrt{\rho_b \kappa_b})^2} \qquad (2.2\text{-}2)$$

where η_{TEG} is the conversion efficiency, T_h is the absolute hot-junction temperature, T_c is the absolute cold-junction temperature, T is the mean absolute temperature, $T = (T_h + T_c)/2$, $Z_{ab}T$ is the figure-of-merit of the couple where α_{ab} is the Seebeck coefficient of the couple, ρ_a and ρ_b are the electrical resistivity of materials a and b, and κ_a and κ_b are the thermal conductivity of materials a and b. From these equations, one can see that, in order to improve the conversion efficiency, the thermocouple must have a large temperature difference between the two ends as well as a high ZT.

2.2.2 Figure-of-Merit

The figure-of-merit of a single material can be written as [5,7]:

$$ZT = \frac{T\alpha^2\sigma}{\kappa} \qquad (2.2\text{-}3)$$

where T is the absolute temperature, α is the Seebeck coefficient, σ is the electrical conductivity, and κ is the total thermal conductivity. In order to maximize ZT, large values for the Seebeck coefficient and electrical conductivity, and low value of the thermal conductivity are necessary.

2.2.2.1 Seebeck coefficient

Based on the theoretical analysis by solving the Boltzmann transport equation with a relaxation time approximation, the Seebeck coefficient can be expressed as follows [5,7,15,17]:

$$\alpha = \pm \frac{k_B}{e}(\delta - \eta) \qquad (2.2\text{-}4)$$

where $$\delta = \frac{(s+\frac{5}{2})F_{s+\frac{3}{2}}(\eta)}{(s+3)F_{s+\frac{1}{2}}(\eta)} \tag{2.2-5}$$

The value of *s* varies with the scattering mechanism: for acoustic lattice scattering, *s=-1/2*; for polar, optical mode lattice scattering, *s=+1/2*; and for ionized impurity scattering, *s=+3/2*. η is the reduced Fermi energy, F_x is the Fermi integral of order *x*. The Seebeck coefficient is positive, when the major carriers are holes, and is negative, when the major carriers are electrons.

In general, the Seebeck coefficient is related to carrier concentration and effective mass. For highly degenerate semiconductors and metals, i.e. parabolic band, energy-dependent scattering approximation, the Seebeck can be also expressed as [16]:

$$\alpha = \frac{8\pi^2 k_B^2}{3eh^2} m^* T \left(\frac{\pi}{3n}\right)^{2/3} \tag{2.2-6}$$

Where, *n* is the carrier concentration, m^* is the effective mass of the carrier, and k_B is the Boltzmann constant. From equation (2.2-6), one can see that Seebeck coefficient decreases with increasing carrier concentration and decreasing effective mass of the carriers.

2.2.2.2Electrical resistivity[18]

The electrical conductivity (σ) is related to carrier concentration *n* (for electrons) and *p* (for holes) through the carrier mobility μ, and can be expressed as:

$$\sigma = ne\mu_n + ph\mu_p \tag{2.2-7}$$

$$\mu_n = \frac{e\langle \tau_n \rangle}{m_n^*}\,;\ \mu_p = \frac{h\langle \tau_p \rangle}{m_p^*} \tag{2.2-8}$$

Where, *e* and *h* are electronic charge of electrons and holes, *n* and *p* are n-type and p-type carrier concentrations, the μ_n and μ_p are the mobility of the carriers, m_n^* and m_p^* are effective mass, and τ_n and τ_p are average relaxation time, respectively. The average relaxation time for both electrons and holes can be expressed as :

$$\tau = \frac{2}{3}\Phi(T)\left(s+\frac{3}{2}\right)(k_B T)^s \left(\frac{F_{s+\frac{1}{2}}(\eta)}{F_{\frac{1}{2}}(\eta)}\right) \qquad (2.2\text{-}9)$$

For electron scattering by either acoustical or optical lattice scattering, *Φ(T)* is proportional to T^1. However, for the ionized impurity lattice scattering mode, *Φ(T)* is relatively independent of temperature.

For a semiconductor in the high temperature range, where intrinsic conduction is the dominating mechanism, the carrier concentration (holes or electrons) are expressed as follows [15-17]:

$$n = 2\left(\frac{2\pi m_n^* k_B T}{h^2}\right)^{3/2} e^{(E_F - E_C)/k_B T} \qquad (2.2\text{-}10)$$

$$p = 2\left(\frac{2\pi m_p^* k_B T}{h^2}\right)^{3/2} e^{(E_V - E_F)/k_B T} \qquad (2.2\text{-}11)$$

where, *h* is the reduced Planck constant.

From equations (2.2-7), (2.2-8) and (2.2-9), one can see that, the electrical conductivity are related to the scattering mechanism, relaxation time, effective mass and Fermi energy. Even though the mobility decreases with increasing effective mass, but after combining with the carrier concentration which is also a function of effective mass, the overall electrical conductivity increases with increasing effective mass. From the equation of Seebeck coefficient, which also indicates that a larger effective mass will lead to higher Seebeck coefficient, it can be concluded that in order to obtain excellent TE properties, the material needs to possess large effective mass.

2.2.2.3 Thermal conductivity

In general, the total thermal conductivity has contributions from both charge carriers κ_e and lattice waves (or phonons) κ_l, i.e:

$$\kappa_{total} = \kappa_e + \kappa_l \qquad (2.2\text{-}12)$$

The electrical contribution to thermal conductivity is related to the electrical conductivity through the Wiedemann-Franz law [5], where *L* is the Lorenz number:

$$\kappa_e = LT\sigma \qquad (2.2\text{-}13)$$

And *L* is equal to:

$$L = \gamma\left(\frac{k_B}{e}\right)^2 \qquad (2.2\text{-}14)$$

where γ can be expressed as:

$$\gamma = \frac{3F_0(\eta)F_2(\eta) - 4F_1^2(\eta)}{F_0^2(\eta)} \qquad (2.2\text{-}15)$$

In some extreme cases, for highly degenerated semiconductor and metal, $\gamma = \pi^2/3$, and for non-degenerated semiconductor, $\gamma = s + 5/2$.

The lattice thermal conductivity is the major contribution to the total thermal conductivity due to the small value of *L* and relative low conductivity of semiconductor. A general expression of lattice thermal conductivity at high temperature range (above Debye temperature) is [19]:

$$\kappa_l = \frac{1}{3} C_v \upsilon_s l \qquad (2.2\text{-}16)$$

Where C_v is the lattice heat capacity per unit volume, v_s is the velocity of sound in the crystal, and l is the phonon mean free path.

According to Callaway's model [20], the theoretical expression for thermal conductivity can be written as follows:

$$\kappa = \frac{k_B}{2\pi^2 \upsilon_s}\left(\frac{k_B T}{\hbar}\right)^3 \left\{ \int_0^{\theta_D/T} \frac{x^4 e^x}{\tau_C^{-1}\left(e^x - 1\right)^2} dx + \frac{\left[\int_0^{\frac{\theta_D}{T}} \frac{\tau_C}{\tau_N} \frac{x^4 e^4}{\left(e^x - 1\right)^2} dx\right]^2}{\int_0^{\frac{\theta_D}{T}} \frac{1}{\tau_N}\left(1 - \frac{\tau_C}{\tau_N}\right) \frac{x^4 e^x}{\left(e^x - 1\right)^2} dx} \right\} \qquad (2.2\text{-}17)$$

where the dimensionless $x = \hbar\omega / k_B T$ is the normal frequency, ω is the phonon frequency, k_B is the Boltzmann constant, $\hbar$ is the reduced Planck constant, θ_D is the Debye temperature, υ_s is the velocity of sounds, and τ_C is the combined phonon scattering relaxation time and the phonon scattering relaxation rate τ_C^{-1} using Matthiessen's rule can be expressed as:

$$\tau_C^{-1} = \tau_B^{-1} + \tau_U^{-1} + \tau_N^{-1} + \tau_A^{-1} + \tau_{e-ph}^{-1} + \tau_D^{-1} \qquad (2.2\text{-}18)$$

Where boundary scattering τ_B, phonon-phonon Umklapp scattering τ_U, phonon-phonon normal scattering τ_N, defect or alloy scattering τ_A, electron-phonon scattering τ_{e-ph}^{-1}, introduction of second phase such as the nanoparticles τ_D, all contributed to the phonon scattering relaxation rate.

All the three parameters (α, σ and κ) that define the figure-of-merit are functions of the carrier concentration as shown by equations (2.2-6), (2.2-7) and (2.2-17). The dependences of the figure-of-merit, *ZT*, Seebeck coefficient α, electrical conductivity σ, and total thermal conductivity κ on carrier concentration n are shown in Figure 2.2-2. Hence, in order to satisfy the requirements of high Seebeck coefficient and electrical conductivity, but at the same time low thermal conductivity, the ideal carrier concentration should be kept at ～10^{19} cm^{-3}, which is found mostly in heavily-doped semiconductors [21].

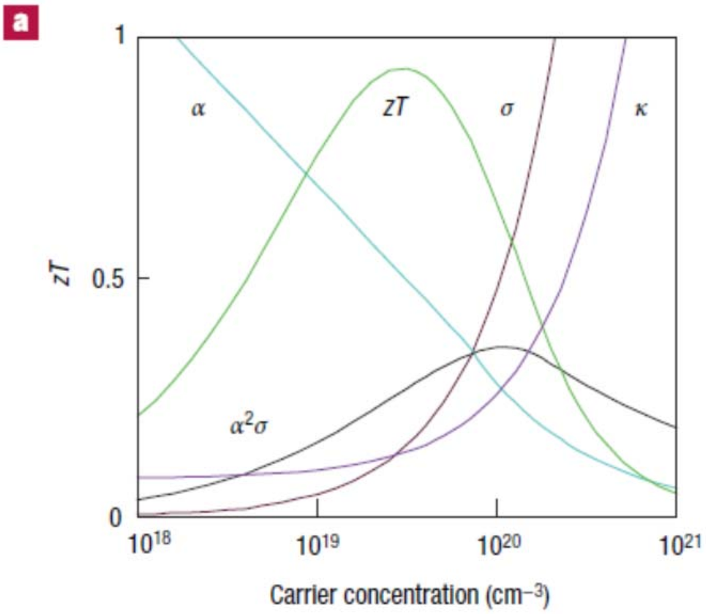

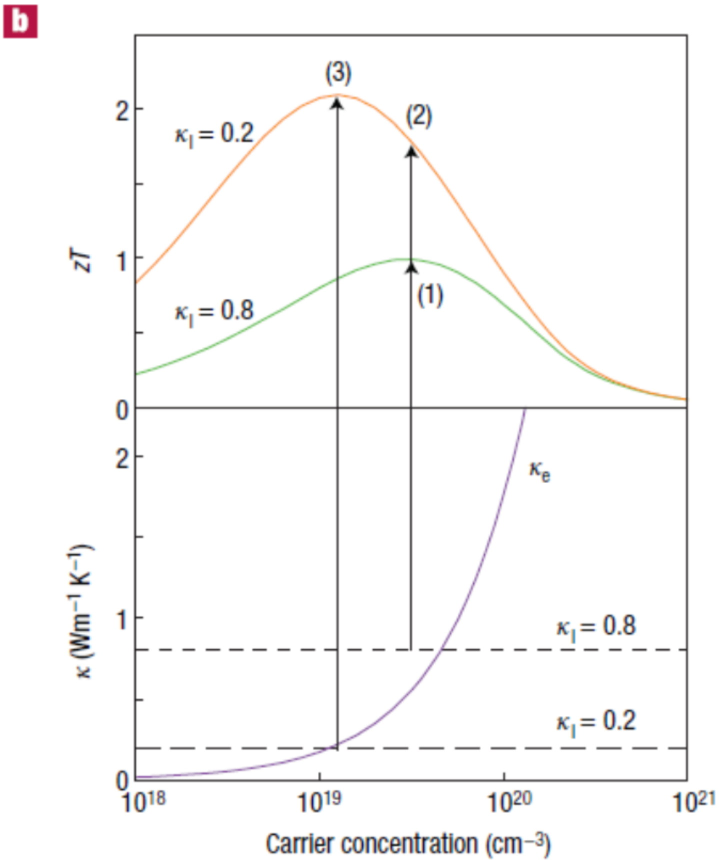

Figure 2.2-2: Dependence of figure-of-merit *ZT*, Seebeck coefficient, electrical conductivity, electrical thermal conductivity and lattice thermal conductivity on carrier concentration [16].

2.2.3 Development of TE materials

Figure 2.2-3 shows *ZT* as a function of temperature for bulk TE materials that have been developed over the last half century. Due to the difference in TE performance, different materials will need to be chosen for different application temperature. Hence, according to their application temperature, TE materials can be classified as low temperature, intermediate temperature and high temperature TE materials. One of the most widespread applications is refrigeration and presently the state-of-art materials are the alloys of Bi_2Te_3 system [22-25]. For near-room-temperature applications, such as refrigeration and waste heat recovery up to 200 °C, Bi_2Te_3 alloys have been proven to possess the best thermoelectric properties. For mid-temperature power generation (500-

900 K), materials based on group-IV telluride are typically used, such as Zn_4Te_3 [26], PbTe and its similar compounds $AgPb_mSbTe_{2+m}$ [15,27-30]. Skutterudites family also shows a great potential in the moderate temperature power generation application [31,32]. For even higher temperature (>900 K), thermoelectric generators have typically used silicon-germanium alloys for both n- and p-type legs [33]. The *ZT* value of these materials is fairly low, especially for the p-type materials, because of the relatively high lattice thermal conductivity induced by the diamond structure.

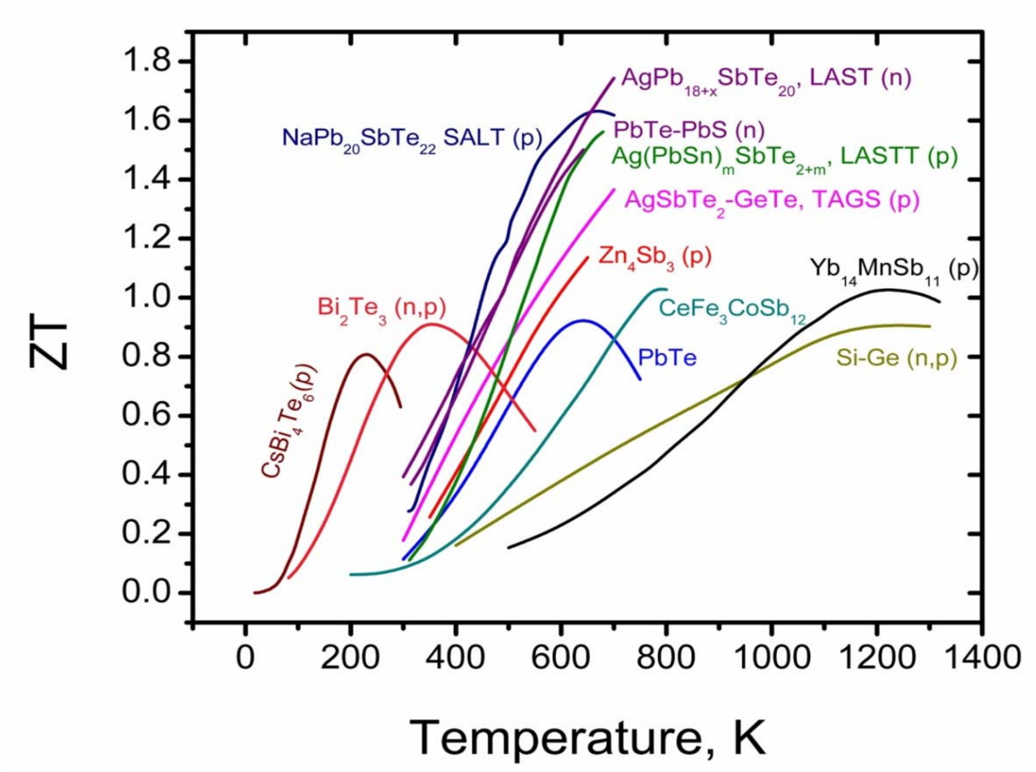

Figure 2.2-3: Dimensionless figure-of-merit ZT as a function of temperature for state of the art materials [34].

In 1990s, two promising methods to improve the thermoelectric properties are proposed. An ideal model of “Phonon-Glass and Electronic-Crystal” (PGEC) was proposed by Slack [7]. In this model, the thermal conductivity of the materials will be close to a glass, and electrical conductivity as high as a perfect single crystal. Promising PGEC bulk thermoelectric materials include skutterudites, clathrates, half-Heusler alloys,

Zn_4Sb_3 alloys, Chalcogenides and so on. At around the same time, Dresselhaus and Hicks [35] proposed a new direction for low-dimensional thermoelectric materials, i.e. introducing quantum-confinement effect to enhance the Seebeck coefficient α. Meanwhile, for the thermal property, the many internal interfaces due to the low-dimensional structures can scatter phonons more effectively than that of electrons based on the differences in their respective scattering wave-length and reduce thermal conductivity. These two proposed methods developed in different ways until more recently where they seem to converge together to born new kind of nanostructured thermoelectric materials, such as Bi_2Te_3 nanotubes, PbTe nanowires [11,10]. Based on the nanostructuring, nanocomposites were further exploited in the hope of reaching a combination of the outstanding TE properties of the nanoscaled structures as well as the proven performance of the bulk materials. In a nanocomposite, the bulk thermoelectric materials act as host materials containing nano-inclusions prepared by chemical method, or, low dimensional nano-scaled inclusions assembling as nano-clusters embedded into a traditional bulk material.

2.3 Skutterudites

2.3.1 Crystal structure

The name of skutterudite comes from a natural mineral, $CoAs_3$, first found in Skutterud, Norway. Skutterudites have a body-center-cubic (BCC) crystal structure and in the space group *Im3* with 32 atoms in per unit cell. The typical and basic structure of the skutterudite unit cell is shown in Figure 2.3-1. In the skutterudite structure (indicated by MX_3, where M represents a metal atom and X a pnictide atom), each X atom has four nearest neighbors, two metal atoms and two pnictide atoms situated at the corners of a distorted tetrahedron. The M atoms are octahedrally coordinated to X atoms, and form the tilted MX_6 octahedrons which share corners with the neighboring octahedrons centered at the position (000), illustrated more clearly in Figure 2.3-2. It is the tilting of these octahedrons that results in a planar X_4 ring structure of pnicogen atoms. The resulting structures resemble a cage with a large void occupying the body-centered position in the cubic lattice. For binary $CoSb_3$ the void radius is 1.892 Å [9, 36-38]. As predicted by Slack, these voids can be filled by guest atoms and the interstitial atoms in the voids could reduce the thermal conductivity, which will be discussed later in section 2.4.2 [5].

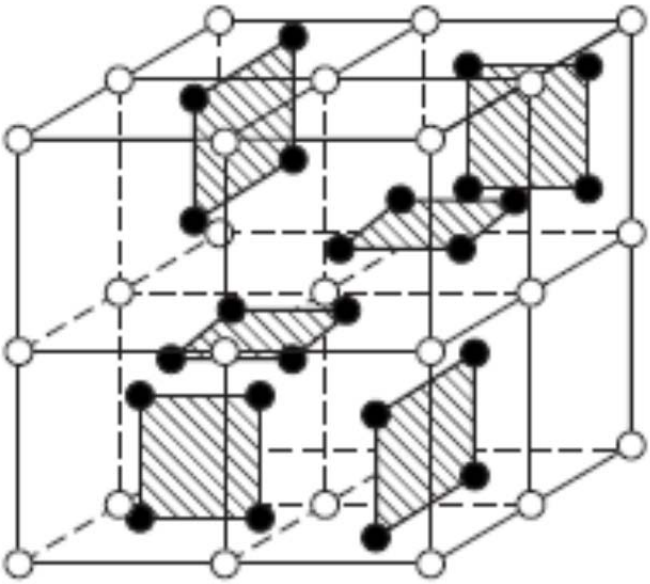

Figure 2.3-1: The skutterudite structure with the metal M (open circles) forming a simple cubic sublattice, and pnicogen atoms X (solid circles) arranged in planar, near-square four-member rings [37].

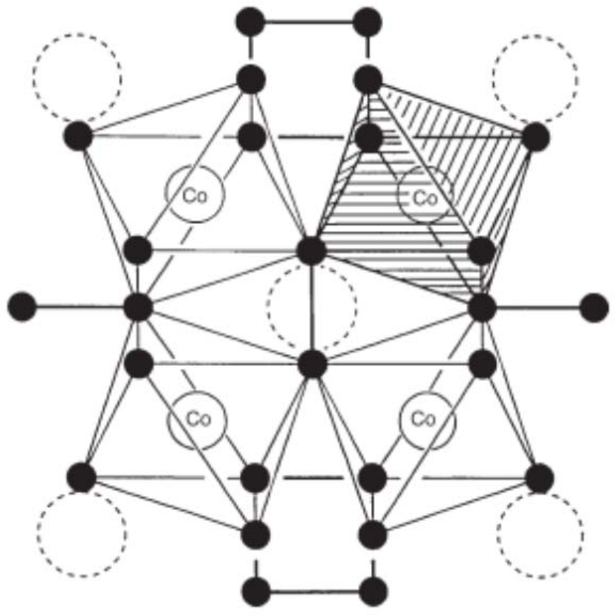

Figure 2.3-2: The unit cell of the skutterudite structure centered at the position (000). Metal atoms (Co in this case) are octahedrally coordinated by the pnicogen atoms and one of the octahedrons is highlighted. Dashed circles represent the voids where the filler ions occupy [37].

2.3.2 Crystal chemistry

The bonding arrangement of skutterudite is believed [9, 39] as follows: every X atom has 5 valence electrons. Two of them have σ bond with two nearest X of the X_4 groups. The other three valence electrons join the M-X bonds. In the MX_6 octahedron, one M (metal atom) is coordinated by 6 X atom leading to a total of (3/2)×6=9 X electrons for M-X bonding. And the M atoms of a s^2d^7 configuration provides another 9 electrons resulting to a total of 18 electrons for M-X arrangement. These electrons are available to form d^2sp^3 hybrid bonds. The octahedral ligand field of the X atoms is believed to split the degenerate d-level into three lower energy non-bonding orbitals and two higher energy orbitals which hybridize the metal atom s as well as p states to form the dps orbital complex to provide the M-X bonding [40]. In these 18 electrons, 6 of them occupy the nonbonding orbitals with a spin-paired arrangement, and the other 12 electrons occupy the hybridized dps complex. These compounds with no unpaired spins are believed to be diamagnetic semiconductors [37].

2.3.3 Electronic transport properties of $CoSb_3$-based skutterudites

Of the different members of the skutterudites family, $CoSb_3$-based compounds have attracted of the most attention. This family of materials possess not only some of the best TE characteristics, but also the constituents are abundant, less volatile and less expensive than most of the alternative skutterudite structures. For $CoSb_3$ containing elements with low electronegativity differences, there is a high degree of covalent bonding, enabling high carrier mobilities and therefore good electron-crystal properties. Compared with other members in the skutterudite family, the Seebeck coefficient of $CoSb_3$ is very competitive , as shown in Figure 2.3-3 [41, 42].

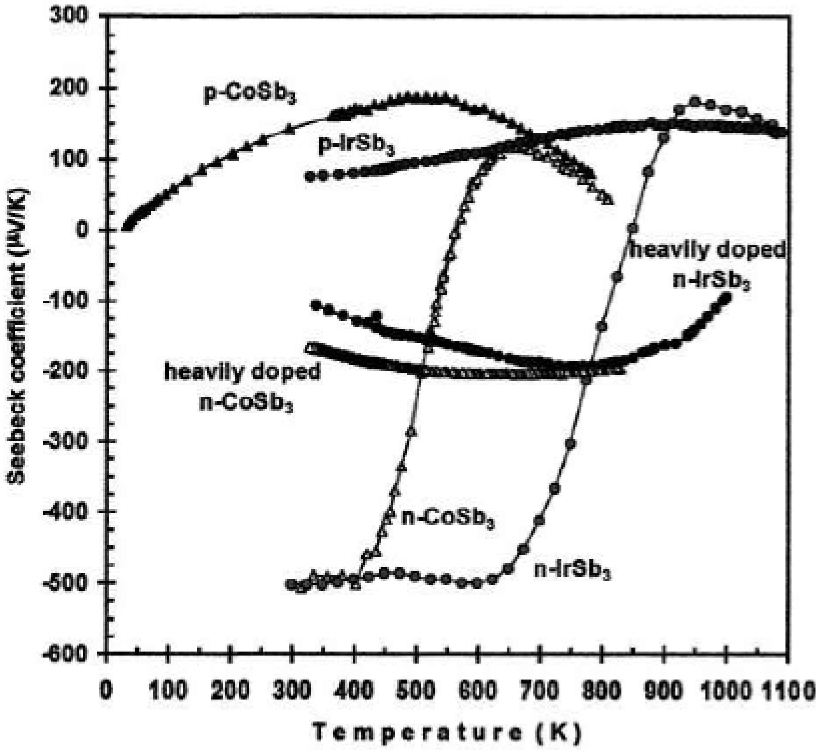

Figure 2.3-3: Seebeck coefficient as a function of temperature for binary skutterudite compounds [41].

2.3.4 Thermal conductivity of $CoSb_3$-based skutterudites

Unfortunately, the thermal conductivity of binary $CoSb_3$ is too high (around 10 W/m·K at room temperature. In comparison, the thermal conductivity of the Bi_2Te_3 system is less than 2 W/m·K at room temperature) to make it efficient and competitive with the classical thermoelectric materials. Although the power factor $P=\alpha^2/\rho$ is relatively high for binary skutterudites, its thermal conductivity must be reduced to that of the theoretical minimum in order for it to be used as a TE material.

According to Equation (2.2-18), the fundamental method to reduce the lattice and hence the total thermal conductivity is to introduce phonon-scatterers. The known methods for scattering phonons in skutterudite compounds are: point defect scattering, charge carriers from dopants, void fillers, and structural defects (including grain boundary and precipitates). All these methods mentioned above introduce scatterers to scatter phonons. The scatterers can be electron, defects (including point and structural defects), guest atoms and so on. According to Rayleigh scattering regime, the scattering cross section varies as $\delta \propto b^6 / \lambda^4$, where b is the size of the scattering particle and λ is the phonon wavelength [20, 43]. Each scatterer has a particular scattering cross section and scatter phonons of a corresponding wavelength. Hence, the combination of more than one phonon-scatterer together can scatter more phonons in a broader wavelength range and can reduce the lattice thermal conductivity more effectively.

2.4 Possible strategies to improve the thermoelectric properties of $CoSb_3$

2.4.1 Doping (Substituting)

The major purpose of doping is to alter the carrier density of the semiconductor [37, 44]. The substitution of Co or Sb by dopants can influence the electronic structure and electrical properties, in particular to substantially change the carrier masses. Here, doping can be considered as alloying. A solid solution reaction in $CoSb_3$ can be described as [45]:

$$(1-x)CoSb_3 + xMSb_3 \rightarrow (M)_x Co_{1-x} Sb_3 \qquad (2.4\text{-}1)$$

for Co substitution, and:

$$(1-x)CoSb_3 + xCoX_3 \rightarrow Co(X_{3x})Sb_{3-3x} \qquad (2.4\text{-}2)$$

for Sb substitution. From thermoelectricity point of view, substitution of Co on the 8c site is more preferable as one does not destroy the integrity of the pnicogen rings and consequently preserves a reasonably high mobility of the structure [9].

Effects of substituting Co with magnetic ions, such as Fe and Ni, have been widely investigated [46-48]. Even a relatively small fraction of Co sites substituted by an impurity such as Ni seems to have a highly beneficial effect on the figure-of-merit [49, 50]. It is also reported that electron-phonon scattering is responsible for the large decrease in lattice thermal conductivity in the Ni doped $CoSb_3$ [51]. Furthermore, it can be expected that doping can affect the lattice thermal conductivity due to the phonon scattering on the point defects caused by the impurity atoms.

Fe is commonly used as the dopant to create p-type $CoSb_3$ materials [52]. The creation of lattice defects by Fe-substitution in $CoSb_3$ is the main cause for the reduction in thermal conductivity [53]. A similar phenomenon of reducing thermal conductivity due to the point-defect scattering also occurs in the As-doped solid solution $Co(Sb_{1-x}As_x)_3$ [54].

2.4.2 Single and double filling

As shown in Figure 2.3-1 and 2.3-2, there are two relatively large voids at the *a* positions of the unit cell which can be filled readily with additional atoms to form filled skutterudites. The cubic unit cell can be written in general as $\square_2Co_8Sb_{24}$, where □ stands for the guest atoms [55]. Many filled $CoSb_3$-based skutterudites have been formed, with lanthanide, actinide, and alkaline-earth ions interstitially occupying these voids [39]. X-ray and neutron structure refinements indicate that for many of the compounds, the guest atoms (such as rare earth or alkaline earth atom) tend to exhibit exceptionally large thermal parameters, corresponding to the "rattling" of these atoms in an oversized atomic cage [56,57]. This rattling atoms, acting as the scatterers, markedly reduce the thermal conductivity of these filled skutterudite compounds. The smaller and more massive ions are promising candidates because they are much freer inside the voids of the skutterudite structures than the bigger ones, and are thereby able to interact with lower-frequency phonon. The smaller ions may also introduce a static disorder in the lattice because they are more off-center than the larger ones, hence further reducing the thermal conductivity [58, 59].

Since each filler ion has its own characteristic Einstein frequency that reflects its mass, size and the strength of bonding with the cage atoms, it makes sense to consider filling the voids with more than one filler species. The different filler atoms should lead to different Einstein frequencies and therefore a broader spectrum of phonons should be affected, further reducing the lattice thermal conductivity [37, 60]. This approach could be also viewed as the forming solid solutions between $R_{1y}Fe_{4-x}Co_xSb_{12}$ and $R_{2y'}Fe_{4-x}Co_xSb_{12}$, where R_{1y} and $R_{2y'}$ are two different filler ions with the respective void occupancies y and y′. For example, the thermal conductivity of double filling $Ce_{1-y}Yb_yFe_4Sb_{12}$ is lower than that of the end members, $CeFe_4Sb_{12}$ and $YbFe_4Sb_{12}$, and the figure-of-merit of double filled skutterudite is significantly improved [37].

Single filled $Yb_{0.25}Co_4Sb_{12}$ has a *ZT* value of 1.1 at around 750K [61]. The highest *ZT* value of $Ca_xCo_4Sb_{12}$ is 0.45 at 800 K and $Ba_{0.3}Co_4Sb_{12}$ is 0.8 at 800 K, respectively [62,63]. Comparing only single filled skutterudite, samples with Ni doping possess better *ZT* value, such as $Ba_{0.3}Ni_{0.05}Co_{3.95}Sb_{12}$ with a *ZT* value of around 1.2 at 800 K which is higher than that of single filled skutterudite without doping [63]. For double filled skutterudite, the *ZT* values are even higher. A ZT of 1.36 at 800 K is achievable for *n*-type $BaxYb_yCo_4Sb_{12}$ without doping [64]. In this material, two types of fillers participate in the scattering of phonons and reduce the lattice thermal conductivity.

2.4.3 Nanostructured materials

The decrease in the grain size of the building block material to the nanometer range leads to a significant increase in the grain boundaries density [5, 9, 65]. Theoretical predictions have shown that nanostructuring reduces the thermal conductivity by the selective scattering of phonons as a result of a much higher density of grain boundaries [65]. According to Rayleigh scattering regime, mentioned before, the scattering cross section varies as $\sigma \propto b^6 / \lambda^4$, where b is the size of the scattering particle and λ is the phonon wavelength [20, 43]. The mid and long-wavelength phonons are greatly scattered by the dense grain boundaries. When the critical length scales of physical phenomena, such as mean-free path (mfp) of phonons and electrons become comparable with the building-blocks of structure, quantum size effect will become evident. Even larger effects on the reduction of thermal conductivity should be achieved for grain sizes of the order of the lattice parameter. In the situation that the mean-free path of phonons is comparable or even greater than that of the carriers, scattering of phonons by grain boundaries is stronger than that of charge carriers. Hence, grain boundary scattering is one of the effective methods in reducing the thermal conductivity of the material, thereby increasing its figure-of-merit, *ZT*.

Many methods such as a polyol method [66], ultrasonic spray pyrolysis (USP) [67], co-precipitation [68], sol-gel [69] and solvothermal method [70], have been used to synthesize nanostructured skutterudites. There are several studies of the grain-size effects on the transport properties of polycrystalline $CoSb_3$ [71]. The experimental data have shown that the thermal conductivity of nanocrystalline $CoSb_3$ samples can be lowered by nearly one order of magnitude as compared to high temperature annealed micron sized $CoSb_3$. The thermal conductivity of ball milled $CoSb_3$ falls from 10.67 $Wm^{-1}K^{-1}$ to 1.44 $Wm^{-1}K^{-1}$, when the grain size of $CoSb_3$ decreases from 10 μm to 100 nm at room temperature [72]. The figure-of-merit is improved by reducing the grain size.

2.4.4 Nanocomposites

As mentioned in the previous section, nanostructure materials exhibit different properties from its corresponding bulk parent. The decrease in the grain size of the material lead to an increase in the density of grain boundaries, which brings about a significant reduction in the thermal conductivity, and hence improve the value of thermoelectric figure-of-merit, *ZT*. However, the decreased grain size also reduces the electrical conductivity at the same time. Based on this shortcoming, nanocomposite TE materials approaches are being explored [73, 74-77]. A nanocomposite TE material is one in which nano-scaled structures are incorporated into the matrix of a conventional bulk TE material in the hope of reaching a compromise between the outstanding TE properties of the nano-scaled structures and the proven performance of the bulk materials. Nanoparticles prepared by solvothermal methods [78-80], chemical reactions [81-83] or even traditional ball-milling [84,85] can be mixed with grinded bulk powders, and subsequently consolidated into a pellet using hot pressing or spark plasma sintering techniques. As shown in Figure 2.4-1, it is presumed that the nanocomposite sample should have better thermoelectric properties than just solely micron- or nano-structure. The path of carrier remains unchanged due to the good connectivity of the micron-sized grains. However, unlike electronic carriers, the phonons cannot select its path, hence, the phonons are scattered by the high density of grain boundaries introduced by nanostructures leading to the reduction of lattice thermal conductivity [86].

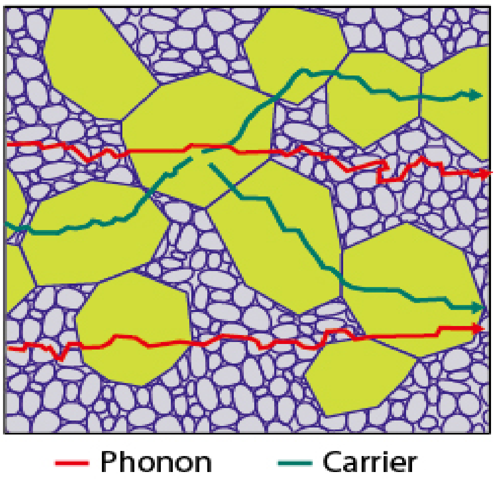

Figure 2.4-1: The presumed carrier and phonon transport path in nanocomposite [87].

Many kinds of TE nanocomposites have been reported, such as PbTe nanocomposites with coated nanostructures on the surface of the bulk material [88], Bi_2Te_3 nanotube-containing nanocomposites [11], and also $CoSb_3$ nanocomposites containing ZrO_2 [73, 75, 59], Yb_2O_3 [90], CeO_2 [91], TiO_2 [92], $FeSb_2$ [93]and $CoSb_3$ [74, 76,77]. All these nanocomposites exhibits reduced thermal conductivity, and shows great potential in improving the TE properties.

2.5 Summary

$CoSb_3$ is a promising TE material for mid range temperature applications due to its large Seebeck coefficient and high electrical conductivity. However, its thermal conductivity remains too high to be used as an efficient thermoelectric material. So far, many efforts using approaches listed in this section have been made to lower its thermal conductivity. In this work, we propose to investigate the reduction of thermal conductivity via the nanocomposites approach. Upon the previous research, it is believed that reduction in thermal conductivity can be achieved after introducing nano-inclusion into micron-sized matrix. However, the effect of nano-inclusion on the electrical properties of final composites is not systematically investigated and reported yet. Hence, in this work, three types of $CoSb_3$-based nanocomposites with distinct electrical properties between nano-inclusion and micron-sized matrix were prepared for comparison. The effects of nano-inclusion on both electrical and thermal properties of nanocomposites will be systematically investigated.

Chapter 3
Experimental Methods

3.1 Sample Preparation

Sample preparation in this work includes: (1) synthesis of pure and Ni-doped $CoSb_3$ nano-particles by a modified polyol process; (2) solid state reaction to synthesize micron-size $CoSb_3$-based materials; (3) mixing of different weight ratio of nano-inclusions and micron-sized matrix by horizontal ball milling; and (4) preparation of the final composite pellets using hot press.

3.1.1 Synthesis of nano-inclusions

3.1.1.1 Synthesis of undoped $CoSb_3$ nano-particles

A modified polyol process was used to synthesize pure $CoSb_3$ nanoparticles. The reaction precursors consisted of a well-defined mixture of 9.2 mM $CoCl_2{\cdot}6H_2O$ and 46 mM $SbCl_3$. Poly-vinylpyrrolidone (PVP) and tetra-ethylene glycol (TEG) were used as surfactant and solvent, respectively. $CoCl_2{\cdot}6H_2O$, $SbCl_3$ and proper amount of PVP were first dissolved in TEG. Then the mixed solution was stirred at 70 °C and deaerated with high purity argon for 20 mins. After that, in order to make sure all the reactant would be reduced, sufficient amount of reducing agent sodium borohydride ($NaBH_4$) was then added. The solution with the reducing agent was heated up slowly to the desired reaction temperature (165 °C – 240 °C) and held for various period of time, whereby black powders would precipitate from the solution. The synthesized powders were washed several times with ethanol and distilled water, and finally dried in oven.

3.1.1.2 Synthesis of Ni-doped $CoSb_3$ nano-particles

For the synthesis of Ni-doped $CoSb_3$ nanoparticles, the experimental procedures are almost same as that of pure $CoSb_3$ nanoparticle, except that $NiCl_2$ was added as an additional reactant according to the nominal composition ($Ni_xCo_{8-x}Sb_{24}$).

3.1.1.3 Synthesis of ZrO_2 nano-particles

In order to reduce the particle size, the ZrO_2 powder (5 µm, 99%) was pulverized by planetary ball-milling at 200 rpm for 2 hours.

3.1.2 Synthesis of micron-size $CoSb_3$-based matrix

3.1.2.1 Synthesis of pure $CoSb_3$ micron-sized powders

The nano-sized $CoSb_3$ prepared by polyol method are p-type semiconductor due to the excess Sb in the chemical reaction. Excess Sb shots were added in order to obtain p-type micron-sized $CoSb_3$. The bulk materials were prepared by solid-state reactions. Co powders (99.995%), and Sb shots (99.99%) were used as the starting materials. Powder mixtures were loaded into a quartz ampoule in an argon-atmosphere glove box. The ampoules were sealed under the vacuum of 10^{-3} Pa. They were heated up to 750 °C at a rate of 1 °C/min and kept at 750 °C for 84 hours.

3.1.2.2 Synthesis of p-type filled skutterudite micron-sized powders

$La_{0.35}Ca_{0.35}Fe_{1.5}Co_{2.5}Sb_{12.03}$ double filled skutterudites were also synthesized by the solid-state reaction method. High purity Ca granules (99%), La powder (99.9%), Fe powder (99.99%), Co powder (99.995%) and Sb shots (99.99%) were used as the starting materials. Stoichiometrically determined portions of these elements were mixed in a carbon-coated quartz tube in an Ar-atmosphere glove box. The tube was sealed under vacuum and heated up to 1000 ºC. The quartz ampoule was held at 1000 ºC for 48 hours and then quenched in a water bath. The same ampoule was then further annealed at 650 ºC for another 240 hours.

3.1.2.3 Synthesis of n-type Te-doped $CoSb_3$ micron-sized powders

Te-doped $CoSb_3$ ($Te_{0.03}Co_{0.97}Sb_3$) were synthesized by a solid-state reaction method. High purity Te powder (99%), Co powder (99.995%) and Sb shots (99.99%) were used as the starting materials. Similar to the procedures for the synthesis of filled skutterudites, stoichiometric determined portions of these elements were mixed in a carbon-coated quartz tube in an Ar-atmosphere glove box. The tube was sealed under vacuum and heated up to 1000 ºC. The quartz ampoule was held at 1000 ºC for 24 hours and then quenched into a water bath. The same ampoule was then further annealed at 650 ºC for another 150 hours.

3.1.3 Preparation of $CoSb_3$ nanocomposites

The ingots obtained from the solid state reaction were then grinded to obtain micron-size polycrystalline powders which would be used as the matrix of the nanocomposites. The micron-sized powders were then mixed with different weight ratio of nano-particles obtained by polyol method (the detailed experimental procedures were presented in Section 3.1.1.1). The mixed powder was horizontally ball-milled for 1 hour to make sure the nano-inclusions were evenly dispersed in the micron-sized matrix. The final composites were then formed by hot pressing at 500 °C for 2 hours under vacuum with a uniaxial pressure of approximately 100 MPa.

3.2 Sample characterization

The samples produced were subjected to various characterizations to verify the structure morphologies as well as to determine their thermoelectric properties.

3.2.1 Phase analysis using X-ray Diffractometer (XRD)

Phase determination was performed through XRD analysis using Shimadzu X6000 diffractometer. Monochromatic CuKα radiation with wavelength (λ) of 1.5406 Å was used with a voltage of 50 kV and current of 40 mA. The XRD data were collected over the 2θ range of 10°～80° at a scanning speed of 2 °/min with step width of 0.02°. The determination of the 2θ values and peak heights, as well as the phase analysis of the collected XRD data was achieved by using the Match!, XRD 6000 software and Topas 3.

3.2.2 Nanocomposites morphology analysis using Field Emission Scanning Electron Microscopy (FESEM)

The distribution of the nanoparticles in the nanocomposites was determined by observing the fractured cross-section of the samples using FESEM (JEOL JSM-6340F). Before the sample was subjected to FESEM observation, the sample was coated with platinum by ion beam sputtering for 60 s using SPI-Module Sputter Coater machine.

3.2.3 Nanoparticles and nanocomposites morphology analysis using Transmission Electron Microscopy (TEM)

TEM (JEOL JSM-2010) was used to study the microstructures of the synthesized nano-powders and hot pressed nancomposite samples. For nano-powders, the particle size was determined from the TEM images. The TEM specimens were prepared by dispersing the nano-powders in ethanol. The material was then ultrasonicated for 15mins, followed by collection using a carbon-coated copper grid. The TEM specimen was then dried in a dry keeper before characterizing under TEM. For hot pressed nanocomposite samples, the TEM specimens were prepared by focus ion beam (FIB) technique using a dual beam system (Helios Nanolab 600).

3.2.4 Thermoelectric properties measurement

The Seebeck coefficient and electrical resistivity were determined by a standard four probe method using ULVAC ZEM-3 between room temperature and 500 °C in a He atmosphere. The delta temperature was set as 10 °C, 15 °C and 20 °C intervals. The results were obtained by averaging the value taken at 3 delta temperatures for each base temperature.

The carrier concentration was determined by Hall system (HL 5500) at room temperature under the Van Der Pauw mode.

The diffusivity *D* was measured under argon atmosphere using laser flash (NETZSCH LFA 457). The sample was cylindrically shaped with a diameter of 12.7 mm. Specific heat capacity *Cp* was determined using the ratio method by comparing the temperature rise of the sample to the temperature rise of a standard sample of known specific heat tested under the same conditions. This temperature rise is recorded as the voltage rise during thermal diffusivity measurement. Assuming the laser pulse energy does not change between the test sample and the standard sample, so

$$Q = m_{st} Cp_{st} \Delta U_{st} = m_{sa} Cp_{sa} \Delta U_{sa} \qquad (3.1)$$

and,

$$Cp_{sa} = \frac{m_{st} \Delta U_{st} Cp_{st}}{m_{sa} \Delta U_{sa}} \qquad (3.2)$$

where, ΔU_{sa} = potential difference (sample) (μV)

ΔU_{st} = potential difference (standard) (μV)

m_{sa} = weight of sample (sample) (mg)

m_{st} = weight of standard (standard) (mg)

Cp_{st} = Cp literature values (standard) (J/g·K)

The density *ρ* was measured by Archimedes method. Thermal conductivity can then be calculated by the following function:

$$\kappa = D \times \rho \times Cp_{sa} \qquad (3.3).$$

Chapter 4
Synthesis of $CoSb_3$-based nano-particles

4.1 Introduction

As discussed in the literature review, nanocomposite is an effective way to reduce lattice thermal conductivity due to the high density of grain boundaries of nano-inclusion which can scatter more phonons, and at the same time maintain the good electrical properties of bulk materials due to the good connectivity of the micron-sized matrix. Therefore, the aim of this chapter is to synthesize both p- and n-type $CoSb_3$-based nano-particles which will be used as nano-inclusions in the preparation of p- and n-type nanocomposites that will be discussed in Chapters 5 and 6, respectively.

In this chapter, the polyol method was chosen to synthesize nano-crystalline $CoSb_3$-based nano-particles due to its rapid and simple procedures [94-99]. Furthermore, this method is also readily used for doping which can further alter the thermoelectric properties of the synthesized nanostructures. Even though, in the polyol process, the polyol acts both as solvent and reducing agent, in our experiments, a very strong reducing agent, $NaBH_4$ was also added to decrease the reaction temperature at which the precursors $CoCl_2{\cdot}6H_2O$ and $SbCl_3$ could be reduced into elemental Co and Sb for reaction to form Co-Sb compounds. A surfactant PVP is added to act as a capping agent to prevent the agglomeration of the nano-particles. From the Co-Sb phase diagram, three Co-Sb compounds, namely CoSb, $CoSb_2$ and $CoSb_3$, exist [100]. Excess Sb precursor was hence added in the reaction to prevent the formation of Sb-deficient phases such as CoSb and $CoSb_2$. Reaction conditions such as reaction temperature and duration are the most important parameters to affect the obtained phase of final products which have not been systematically investigated so far. Hence, in this chapter, the reaction conditions i.e. reaction temperature and duration were optimized in order to obtain the pure $CoSb_3$ phase.

And a possible phase development mechanism is also proposed. It should be noted that the $CoSb_3$ phase obtained in this work is Sb-rich phase, which is a p-type semiconductor with holes as the major carriers.

After the successful synthesis of undoped p-type $CoSb_3$, Ni-doped n-type $CoSb_3$ was prepared. Nickel possesses approximate covalent radii to that of Co, and has one more electron than Co at the outer shell to provide to the lattice, hence making it a promising n-type dopant candidate to substitute Co in the lattice. Ni-doped n-type $CoSb_3$ was prepared under the optimized reaction conditions of $CoSb_3$ synthesis. The experimental procedures were similar with the exception that $NiCl_2$ was added in the reaction precursor to obtain Ni-doped $CoSb_3$. The dopant content was also varied to optimize the thermoelectric properties of Ni-doped $CoSb_3$. Doping has the positive effect on both electrical properties and lattice thermal conductivity. The dopant can alter the major carrier and carrier concentration, and can give rise to a decrease in electrical resistivity. Meanwhile, in addition to the high density of grain boundaries present in nanostructures, the additional dopants can also aid in the scattering of phonons and further reduce the lattice thermal conductivity.

4.2 Synthesis of pure p-type $CoSb_3$ nano-particles by polyol method

In order to obtain $CoSb_3$ phase, reaction temperature and duration are two important parameters that has to be optimized. The temperature was varied from 165 °C to 240 °C. For reaction temperatures below 165 °C, the amount of powder precipitate was very little and the reaction is obviously incomplete. The reaction duration was varied from 5 mins to 30 mins, and in some experiments, the duration was prolonged to 60 mins.

4.2.1 Effects of reaction temperature

Figure 4.2-1 shows the XRD patterns of the products prepared at various temperatures (165 °C, 195 °C and 240 °C) with fixed reaction duration of 5 mins. It was observed that CoSb can be prepared at a relatively low temperature of 165 °C while higher temperatures (195 °C and 240 °C) are required to obtain the $CoSb_3$ phase. The peaks attributed to Sb for the sample prepared at 195 °C and attributed to both Sb and $CoSb_2$ for the sample prepared at 240 °C are observed with a reaction duration of 5 mins. From the experimental results, one can see a relatively high temperature (≥195 °C) is necessary to synthesize $CoSb_3$ phase. Furthermore, in order to obtain high purity $CoSb_3$ phase, optimizing the reaction duration is also necessary.

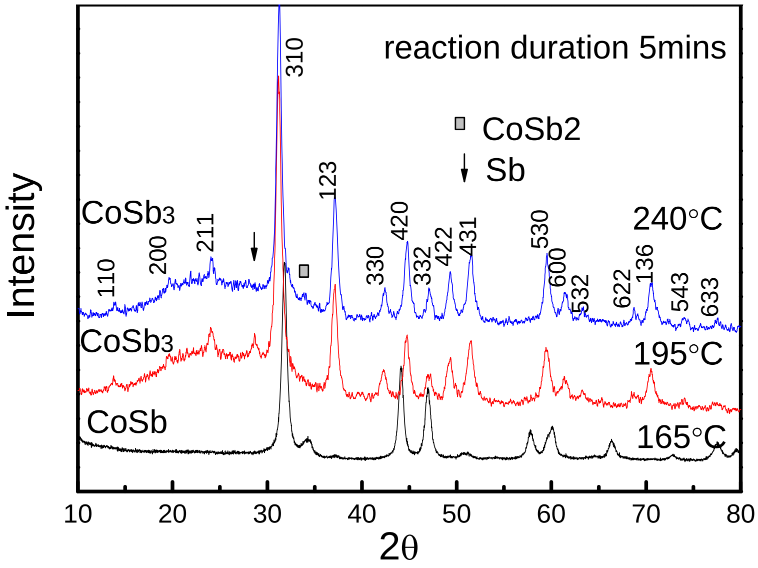

Figure 4.2-1: Powder XRD patterns for the products prepared at various temperatures with reaction duration of 5mins.

4.2.2 Effects of reaction duration

Other than the reaction temperature, another key parameter that determines the phase composition of the final products is the reaction duration. As shown from the XRD analysis in Figure 4.2-2, when the reaction was prolonged to 60 mins at 165 °C, CoSb phase was still the only phase that was formed. This indicates that CoSb is a stable phase in this reaction at a relative low temperature of 165 °C.

At higher reaction temperatures, the observations were different. When the reactions were carried out at 195 °C for 5 mins, $CoSb_3$ and a small amount of Sb appeared in the final products. This might be due to the excess Sb that was added in the precursory step and the reaction time was insufficient for the full reaction to occur. Hence, after the completion of the experiment, the unreacted element Sb precipitated and mixed with the synthesized $CoSb_3$. When the reaction duration was prolonged to 15 mins, pure phase of $CoSb_3$ were obtained as there was sufficient time for the reaction to occur. However, when the reaction duration was further extended to 30 mins at 195 °C, Sb reappeared with $CoSb_2$ in the final products. This suggests that the $CoSb_3$ phase is unstable with prolonged reaction time. A similar situation was also reported during the synthesis of $CoSb_3$ via mechanical alloying process [101]. It was reported that the amount of $CoSb_3$ initially increased with the milling time. However, further milling led to the reduction of the $CoSb_3$ phase, and it was proposed that $CoSb_3$ decomposed to $CoSb_2$ and Sb. In both of these experiments, nano-crystalline $CoSb_3$ phase were produced. It is likely that the as-synthesized nanostructured $CoSb_3$ phase is metastable, and prolonged reaction can cause them to decompose into $CoSb_2$ and Sb phases instead.

For reaction at 240 °C, even when the reaction duration was as short as 5 mins, both Sb and $CoSb_2$ phase were detected. This may be because $CoSb_3$ phase was already produced at lower temperature, and when the temperature was increased, $CoSb_3$ decomposed into $CoSb_2$ and Sb phases. The peak intensity of $CoSb_2$ and Sb increased with prolonged reaction duration, which means that with the reaction duration extended, the amount of Sb and $CoSb_2$ increased due to the decomposition of $CoSb_3$.

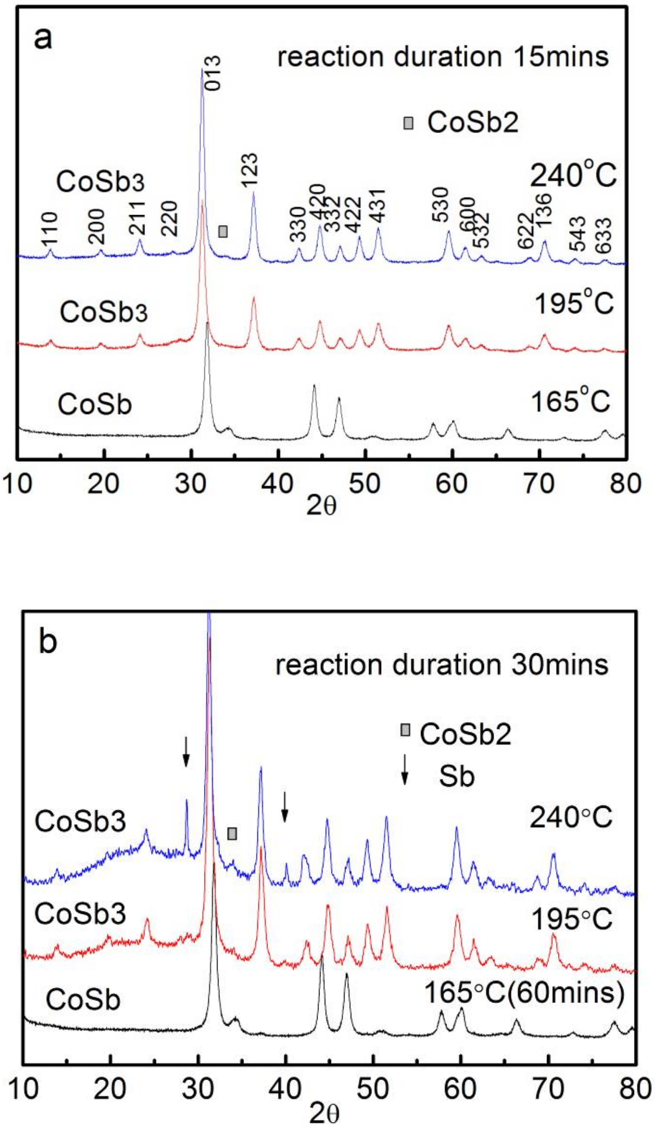

Figure 4.2-2: Powder XRD patterns for the products prepared at various temperatures with various reaction durations of 15 mins (a) and 30mins (b).

The phase compositions of the products obtained at the various synthesis conditions are summarized in Table 4.2-1.

In order to investigate whether the Sb and $CoSb_2$ were decomposed from $CoSb_3$, or they were the remnants of the reactants, the refinement of the XRD patterns of the samples obtained at 195 °C and 240 °C with a reaction duration of 5mins were analysed, and the results are shown in the Figure 4.2-3. From the refinement results obtained for the sample reacted at 240 °C, trace amount of Sb and $CoSb_2$ were observed. From the weight ratio of the refinement result, the molar ratio of Sb to $CoSb_2$ is calculated to be 0.9:1.1, which is very close to the 1:1 ratio, indicating that the Sb and $CoSb_2$ came from the reaction $CoSb_3=CoSb_2+Sb$. However, for the sample reacted at 195 °C, according to the XRD result, in addition to the peaks of $CoSb_3$ phase, only peaks attributed by the Sb phase were observed. Peaks corresponding to the $CoSb_2$ phase were not observed. If this Sb came from the decomposition of $CoSb_3$, a same molar amount of $CoSb_2$ must come out simultaneously but this is contradictory to the experimental results. Hence, the Sb remaining in the sample at 195 °C can only be the remnant of reduced Sb from the reaction $2SbCl_3+6NaBH_4 \rightarrow 2Sb+6BH_3+6NaCl+3H_2$. Here, we can reach the conclusion that the Sb phase in the sample reacted at 195 °C was remnants of unreacted Sb, while the Sb and $CoSb_2$ phases in the sample reacted at 240 °C were due to the decomposition of $CoSb_3$.

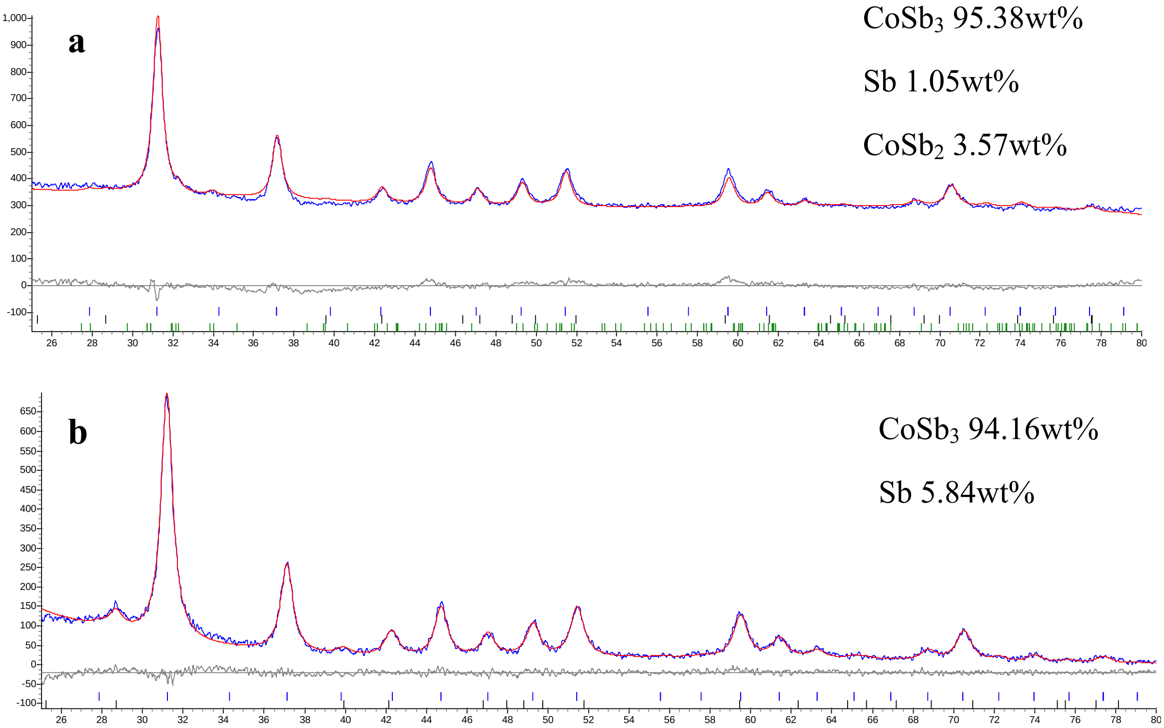

Figure 4.2-3: XRD refinement results of the sample obtained at 240 °C with a reaction duration of 5 mins (a) and the sample obtained at 195 °C with a reaction duration of 5 mins (b).

Table 4.2-1: Phase compositions of the products obtained at the various synthesis conditions.

Duration / Temperature	5 mins	15 mins	30 mins
165 °C	CoSb	CoSb	CoSb (60 mins)
195 °C	$CoSb_3$+Sb	$CoSb_3$	$CoSb_3$+$CoSb_2$+Sb
240 °C	$CoSb_3$+$CoSb_2$	$CoSb_3$+$CoSb_2$	$CoSb_3$+$CoSb_2$+Sb

From the experimental results, one can see that this experiment is a temperature and duration dependent reaction. At 165 °C, only CoSb phase was detected in the synthesized product even when the duration time was prolonged to 60 mins. By further increasing the reaction temperature to 195 °C and even 240 °C, $CoSb_3$ phase was obtained. However, the phase compositions are dependent on the reaction duration as well. At 195 °C, when the reaction duration was only 5 mins, $CoSb_3$ with a small amount of Sb was detected. When the reaction duration was extended to 15 mins, only pure $CoSb_3$ was obtained. With the reaction time further increased to 30 mins, the diffraction peaks corresponding to the $CoSb_3$, Sb and $CoSb_2$ phases were observed in the XRD results. For reaction temperature of 240 °C and with a relatively short reaction duration (5 mins and 15 mins), $CoSb_3$ with trace amount of Sb and $CoSb_2$ were formed. When the duration was further increased to 30 min, the peaks corresponding to the Sb and $CoSb_2$ phases become more obvious. Hence, the optimized reaction condition is at a temperature of 195 °C for 15 mins.

This optimized reaction condition will be used in the synthesis of n-type Ni-doped $CoSb_3$ nano-particles as described later in Section 4.3.

4.2.3 Phase development mechanism

The experimental observation seems to indicate that the formation of the $CoSb_3$ phase takes place in a stepwise mode. At the start of the experiment, the addition of $NaBH_4$ reduced the Co^{2+} and Sb^{3+} ions to Co and Sb atoms, according to reactions (4.1) and (4.2), respectively. The same reducing reactions were also reported by Zhao's group as the starting step to synthesize $CoSb_3$ by a solvothermal method [6]. With further increase in temperature, the reduced active Co and Sb atoms will react with each other to form the intermetallic Co-Sb products. In our experiments, CoSb is obtained preferentially rather than $CoSb_2$ at relatively low temperature (165 °C). The absence of $CoSb_2$ at 165 °C can be explained based on the thermodynamic calculations as shown in Figure 4.2-4 [102-104]. According to the calculation of Gibbs free energies, within our experimental temperature range, the remaining Co will react with $CoSb_2$ to form CoSb once $CoSb_2$ was formed in the reaction. Due to the relatively low reaction temperature (165 °C), the reduction reactions ((4.1) and (4.2)) cannot be completed to supply enough Sb to produce $CoSb_2$ even when the reaction duration was prolonged to another 60 mins. Hence, CoSb is the only product in the reaction at a temperature of 165 °C. With further increase in temperature, the formation of Sb will be completed and reaction (4.4) will take place to form $CoSb_3$. However, with higher temperature or prolonged reaction duration, $CoSb_3$ will decompose into $CoSb_2$ and Sb ((4.5)).

$$CoCl_2+2NaBH_4 \rightarrow Co+2BH_3+2NaCl+H_2 \quad (4.1)$$

$$2SbCl_3+6NaBH_4 \rightarrow 2Sb+6BH_3+6NaCl+3H_2 \quad (4.2)$$

$$Co+Sb \xrightarrow{165^{\circ}C} CoSb \quad (4.3)$$

$$CoSb+2Sb \longrightarrow CoSb_3 \quad (4.4)$$

$$CoSb_3 \longrightarrow CoSb_2+Sb \quad (4.5)$$

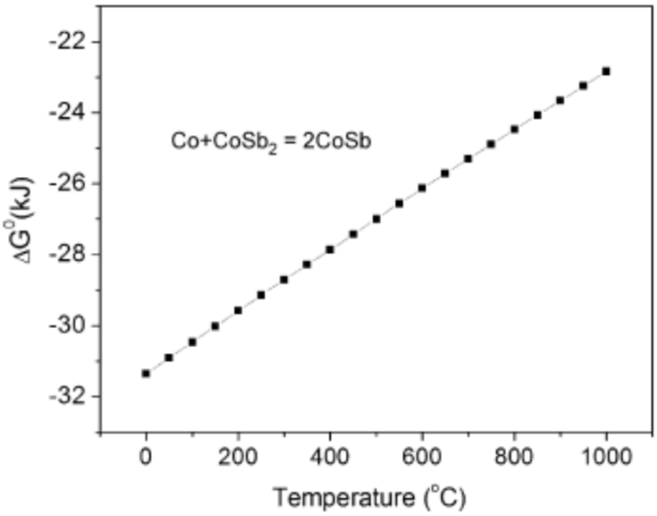

Figure 4.2-4: Gibbs free energies ΔG^0 as function of temperature for the reaction of Co+CoSb$_2$=2CoSb [102].

4.2.4 Microstructure analysis

Figure 4.2-5 (a) shows the typical morphology of the as-synthesized pure CoSb$_3$ nano-particles obtained at optimized reaction conditions (195 °C, 15 mins). Figure 4.2-5 (b) is a high resolution TEM image of as-synthesized pure CoSb$_3$ nano-particles to show its polycrystallinity. The particles are surrounded by amorphous surfactant which is reasonable since PVP was applied to during synthesis to prevent crystal growth. And these surfactants will be removed in the following hot press process. The indexed electron diffraction pattern (inset) confirms that the nanoparticles are pure CoSb$_3$ phase without any other impurity such as CoSb$_2$, CoSb or Sb. This is consistent with the XRD results. The continuous and homogenous ring pattern indicates its polycrystallinity without any prefer orientation, and confirms its even and fine grain size. The particle size of these nano-particles is below 30 nm which is in a good agreement with the results of 22.8 nm from XRD Rietveld refinement shown in Figure 4.2-4 (c). These pure CoSb$_3$ nanoparticles will be used as nano-inclusions in Chapter 5.

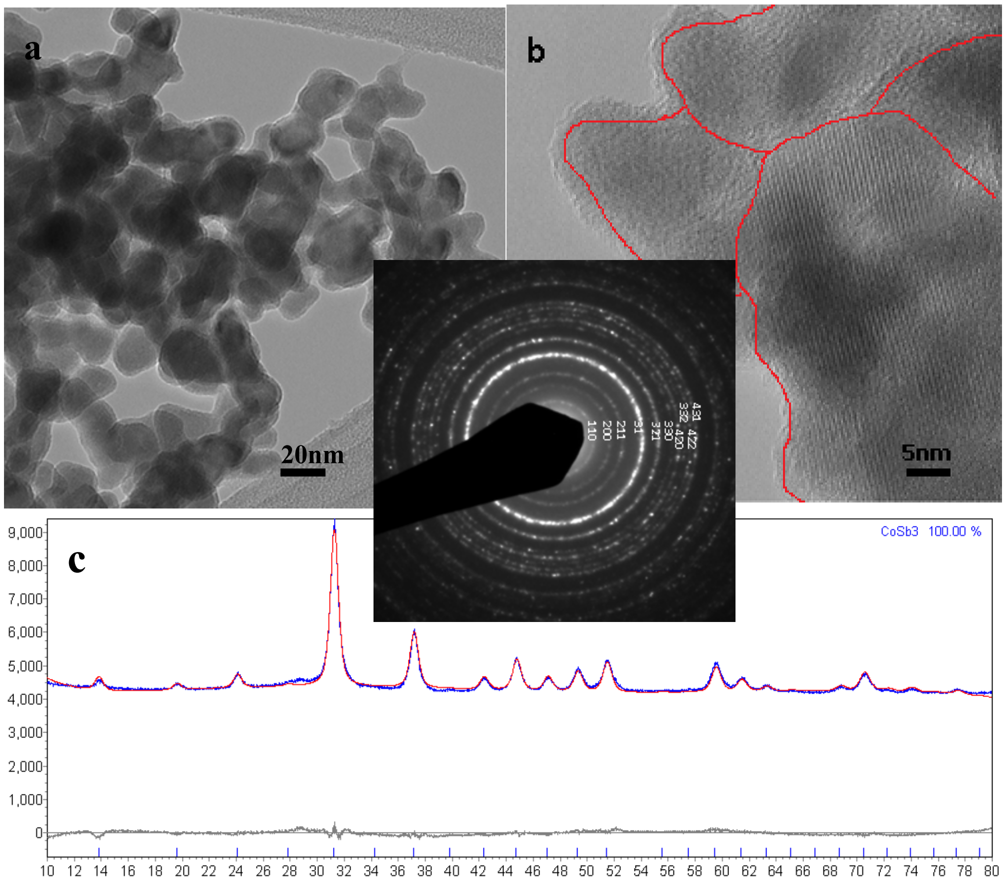

Figure 4-2.5: TEM image (a), HRTEM image (b) and XRD refinement results (c) of the nanostructured $CoSb_3$ synthesized under optimized condition of 195 °C and 15 min. The inset is electron diffraction pattern of the as-synthesized nanostructured $CoSb_3$.

4.3 Synthesis of nanostructured Ni-doped n-type $Ni_xCo_{8-x}Sb_{24}$

After the successful synthesis of p-type $CoSb_3$ nano-particles, n-type $CoSb_3$ were prepared. Ni was chosen as the dopant substituting Co in the skutterudite lattice as Ni and Co has very similar covalent radii (Co: 1.16 Å and Ni: 1.15 Å), electronegativities (Co: 1.88 and Ni: 1.91) and atomic mass (Co: 58.93 and Ni: 58.70) [105,18]. Furthermore, Ni has one more electrons at the outer shell ($3d^8$ $4s^2$) than that of Co ($3d^7$ $4s^2$), will provide one more electron than Co [5]. Therefore, the major carriers can be changed from holes to electrons, and make the materials an n-type semiconductor.

Ni-doped $CoSb_3$ nano-particles were synthesized using the optimized reaction conditions as mentioned earlier for the synthesis of p-type $CoSb_3$ nano-particles. The experimental procedures were almost the same except that $NiCl_2$ was added as a precursor according to the nominal composition of $Co_{8-x}Ni_xSb_{24}$ where x=1, x=1.25 and x=1.5. Doping effects on the thermoelectric properties were investigated. The Ni-doped sample will then be used as the n-type nano-inclusion in the subsequent work on the preparation of n-type nanocomposites presented in Chapter 6.

4.3.1 Phase analysis

Using the optimized reaction conditions (reaction temperature 195 °C and reaction duration 15 mins) achieved in the synthesis of pure $CoSb_3$, Ni-doped n-type $Ni_xCo_{8-x}Sb_{24}$ nano-particles were prepared. $NiCl_2$ was added in the reaction precursor according to the nominal compositions $Co_{8-x}Ni_xSb_{24}$ where x=1, x=1.25 and x=1.5. Figure 4.3-1 shows the XRD patterns of the nano-particles prepared with the various nickel doping level ($Co_{8-x}Ni_xSb_{24}$, x=1, x=1.25 and x=1.5). At low doping level $Co_7Ni_1Sb_{24}$, the nano-particles are of pure skutterudite phase. With further increase in the doping level, the peaks attributed to $Co_{1-n}Ni_nSb$ (can be considered as (1-n)CoSb+(n)NiSb) appeared, and the intensity of these peaks increased with doping level. This observation indicates that (1) the intermediate product $Co_{1-n}Ni_nSb$ in the synthesis of Ni-doped $CoSb_3$ still remains, i.e. the reaction: $Co_{1-n}Ni_nSb+2Sb \rightarrow Co_{1-n}Ni_nSb_3$ is difficult to complete in high Ni content; and (2) not all Ni go into the skutterudite lattice during the polyol method synthesis.

The optimization of reaction condition for the synthesis of undoped $CoSb_3$ suggests that both increasing reaction temperature and prolonging the reaction duration may lead to the completion of this reaction, but at the same time, these conditions can also cause the skutterudite phase to decompose into $Co_{1-n}Ni_nSb_2$ and Sb at higher temperature or with long reaction duration. In order for this material to be used in a TE device and for the characterization of their TE properties, the as-synthesized loose nano-particles have to be pressed into dense materials. Fortunately, during the hot pressing process, the $Co_{1-n}Ni_nSb$ phase can react with Sb to produce the desired $Co_{1-n}Ni_nSb_3$ phase. This will be discussed in Section 4.4.

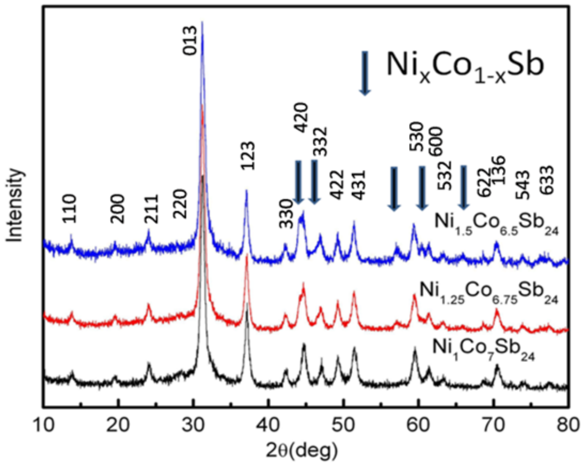

Figure 4.3-1: XRD patterns of the nano-particles prepared with various nickel doping level (nominal composition) $Co_{8-x}Ni_xSb_{24}$ where x=1, x=1.25 and x=1.5.

The actual compositions of as-synthesized undoped and Ni-doped $CoSb_3$ powders are determined by EPMA and the results are shown in Table 4.3-1. The EPMA results indicate that the contents of element Sb of all the samples are higher than that of stoichiometric proportion of skutterudite phase. This may be due to the excess Sb precursor in the reactants in order to get Sb-rich $CoSb_3$ phase. The actual content of dopant Ni is smaller than that of nominal composition, and the deviation increases with doping level. It seems that it is difficult for the dopant to be incorporated into the lattice at relatively high doping level.

Table 4.3-1 Nominal and actual composition of hot pressed pellets prepared with undoped $CoSb_3$ (Co_8Sb_{24}) and Ni-doped $Co_{8-x}Ni_xSb_{24}$ (x=1, x=1.25 and x=1.5) nanoparticles.

Nominal composition	Actual composition
Co_8Sb_{24}	$Co_8Sb_{31.6}$
$Co_7Ni_1Sb_{24}$	$Co_7Ni_{0.98}Sb_{31.3}$
$Co_{6.75}Ni_{1.25}Sb_{24}$	$Co_{6.75}Ni_{1.19}Sb_{31.7}$
$Co_{6.5}Ni_{1.5}Sb_{24}$	$Co_{6.5}Ni_{1.32}Sb_{31.6}$

The lattice parameters for undoped $CoSb_3$ and Ni-doped $Co_{8-x}Ni_xSb_{24}$ (x=1, x=1.25 and x=1.5) are also determined by refining XRD data though Rieveld method and showed in Figure 4.3-2. Since the lattice parameter of $NiSb_3$ is 9.13 Å which is bigger than that of $CoSb_3$ (9.041 Å), the lattice parameter increase with increasing doping content [106,107]. It should be noted that the refined lattice parameter of $CoSb_3$ in our experiments is 9.056 Å which is bigger than that of standard value 9.041 Å. This is due to the actual composition deviation from the stoichiometric proportion of skutterudite phase. For the nano-particles prepared via polyol method are in the Sb-rich phase, i.e. more Sb atoms subside in the lattice of skutterudite which will lead to the lattice distortion as well as increase in lattice parameter.

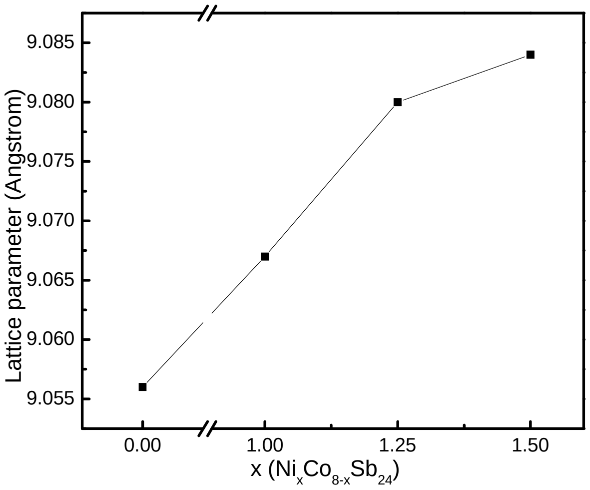

Figure 4.3-2: Lattice parameters of the nano-particles prepared with various nickel doping level (nominal composition) $Co_{8-x}Ni_xSb_{24}$ where x=1, x=1.25 and x=1.5).

There is no direct characterization technique that is available to determine the exact location of Ni in the $CoSb_3$ lattice. Here, we can only indirectly deduce the possible locations of Ni. Based on the results of lattice parameter that the lattice parameter increases with increasing doping level and the major carriers changed from holes into electrons after doping, discussed in section 4.4, there are mainly two possible locations for Ni ions before reaching doping limit (>25%): as dopant at the Co site and as filler in the void of the $CoSb_3$ skutterudite crystal lattice [5].

As dopant, Ni is most possibly located at the Co site due to their very similar covalent radii (Co: 1.16 Å and Ni: 1.15 Å), electronegativities (Co: 1.88 and Ni: 1.91) and atomic mass (Co: 58.93 and Ni: 58.70). Based on previous reported work [5], it is assumed that Ni is located at the Co site. This assumption is supported by the lattice parameter results. Since the lattice parameter of $NiSb_3$ is 9.13 Å which is bigger than that of $CoSb_3$ (9.041 Å), the lattice parameters after Ni doping in $CoSb_3$ should increase with increasing Ni doping content. This trend is in a good agreement with our lattice parameter results. Moreover, the change in the major carriers after doping (results are discussed in section 4.4.3) also confirms the location of Ni at the Co site. The carrier concentration and Seebeck coefficient results indicate that after doping, the major carriers change from holes into electrons. This is a result of Ni having one more electrons at the outer shell ($3d^8$ $4s^2$) than that of Co ($3d^7$ $4s^2$), which will provide one more electron than Co when Co is substituted by Ni.

As filler, Ni has to be located in the void site. This is unlikely to happen as the void radius of the skutterudite crystal lattice is 1.892 Å, which is much bigger than that of the covalent radius of Ni. If Ni happens to come into the void, during the applied hot press processing, Ni would rather leave this unstable location.

4.3.2 Microstructure analysis

From TEM observation, all the Ni-doped $CoSb_3$ samples have very similar morphology. Figure 4.3-3 shows the typical morphology of the as-synthesized Ni-doped $CoSb_3$ nano-particles for with various doping level. The particle sizes are around 30nm. Similar to that of undoped $CoSb_3$, the particles are surrounded by amorphous surfactants, since PVP was applied during synthesis to prevent crystal growth.

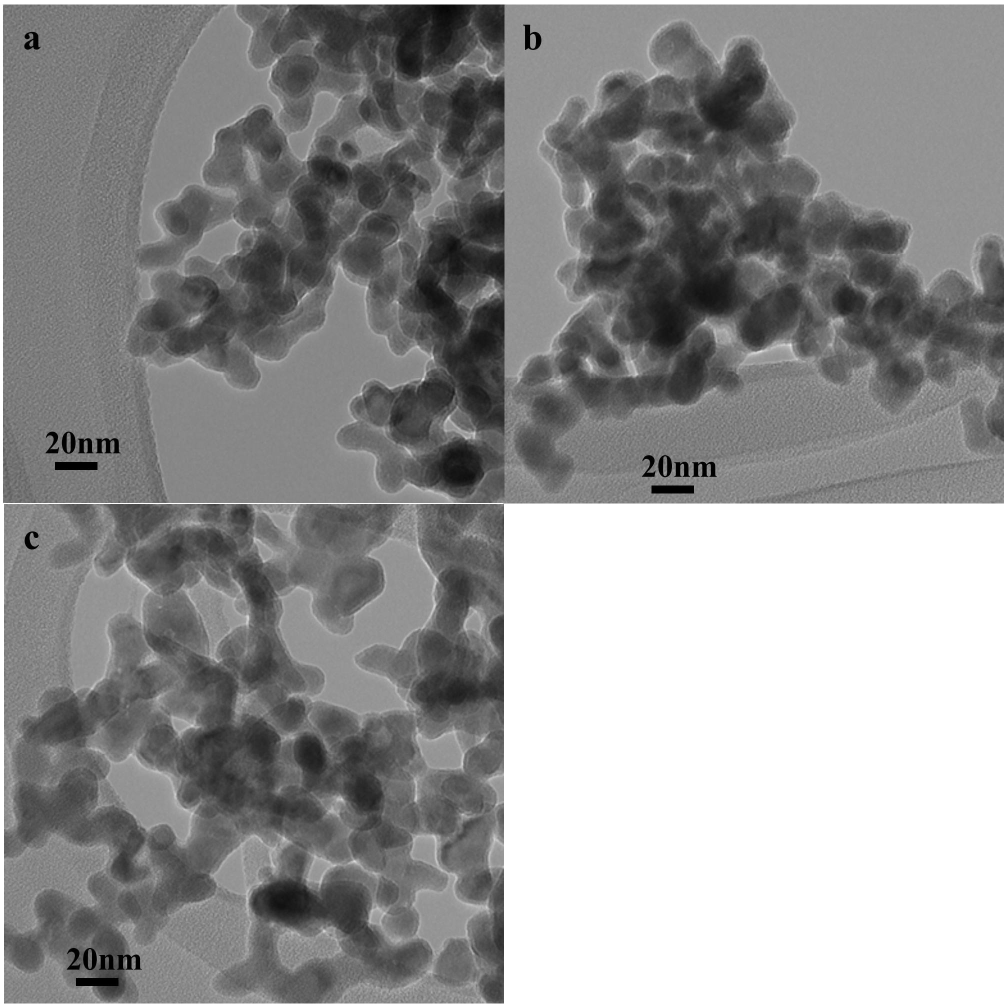

Figure 4.3-3: Typical TEM images Ni-doped $Co_{8-x}Ni_xSb_{24}$ (x=1 (a), x=1.25 (b) and x=1.5 (c)) nano-particles.

4.4 Thermoelectric properties of undoped $CoSb_3$ and Ni-doped $Co_{8-x}Ni_xSb_{24}$ (x=1, x=1.25 and x=1.5) nanostructured materials

In order to characterize the thermoelectric properties of the undoped $CoSb_3$ and Ni-doped $Co_{8-x}Ni_xSb_{24}$, the powders were hot pressed into pellets at 500 °C and at a pressure of 100 MPa in vacuum. In this section, the phase and microstructure analysis as well as the thermoelectric properties of the hot pressed pellets are presented.

4.4.1 Phase identification

Figure 4.4-1 shows the XRD patterns of the pellets prepared with undoped $CoSb_3$ nano-particles and Ni-doped $Co_{8-x}Ni_xSb_{24}$ (x=1, x=1.25 and x=1.5) nano-particles after hot pressing. As shown earlier (Figure 4.3-1), before hot pressing, the heavily Ni-doped $CoSb_3$ nano-particles contain impurity of $Co_{1-n}Ni_nSb$ phase. However, after hot pressing, the peaks contributed by $Co_{1-n}Ni_nSb$ disappear, instead, additional diffraction peaks corresponding to the Sb phase were observed for all the pellet samples prepared from the undoped $CoSb_3$ and Ni-doped $Co_{8-x}Ni_xSb_{24}$ (x=1, x=1.25 and x=1.5) nano-particles (see Figure 4.4-1). A possible reason for the appearance of the Sb phase in the hot pressed pellets is that the synthesized nanostructured Sb-rich $CoSb_3$ phase was metastable, and hence during the hot pressing process, some excess Sb in the Sb-rich $CoSb_3$ metastable phase would choose to exist as the elemental Sb phase, instead of existing inside the $CoSb_3$ lattice. And meanwhile, the $Co_{1-n}Ni_nSb$ in the as-synthesized nano-particles reacted with these excess Sb and produced $Co_{8-x}Ni_xSb_{24}$ under the hot pressing process.

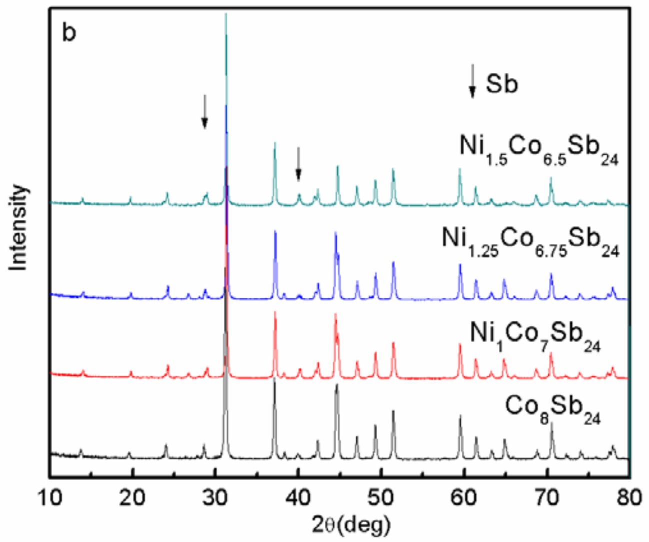

Figure 4.4-1: XRD patterns of hot pressed pellets prepared with undoped $CoSb_3$ (Co_8Sb_{24}) and Ni-doped $Co_{8-x}Ni_xSb_{24}$ (x=1, x=1.25 and x=1.5) nanoparticles.

4.4.2 Microstructure analysis

Figures 4.4-2 (a)-(d) show typical FESEM images of the fractured surfaces of the hot-pressed pellet samples prepared with undoped $CoSb_3$ (Co_8Sb_{24}) and Ni-doped $Co_{8-x}Ni_xSb_{24}$ (x=1, x=1.25 and x=1.5) nano-particles. The size of the particles generally ranges from 50 nm for undoped $CoSb_3$ nanostructures to a few hundred nanometers for Ni-doped $Co_{8-x}Ni_xSb_{24}$. Generally speaking, the grain size increased with increasing Ni-doping content. As compared with the as-synthesized nano-particles (around 30 nm) which were shown previously in Figure 4.2-5 and Figure 4.3-3, the particle size increased after hot pressing. The particles aggregated and grew during the hot press process. It is also observed that there are two types of particles in Ni-doped $Co_{8-x}Ni_xSb_{24}$, the smaller ones of below 100 nm in spherical shape and larger ones of 300-500 nm in bar shape. We guess that the smaller ones grew from the synthesized skutterudite phase nano-particles which are similar to that of undoped $CoSb_3$. And the larger ones were synthesized from $Co_{1-n}Ni_nSb$ and excess Sb during the hot pressing process. The high temperature (500 °C) and pressure (100 MPa) make the reaction $Co_{1-n}Ni_nSb+2Sb \rightarrow Co_{1-n}Ni_nSb_3$ very fast and produce larger particle sized $Co_{1-n}Ni_nSb_3$ in bar shape.

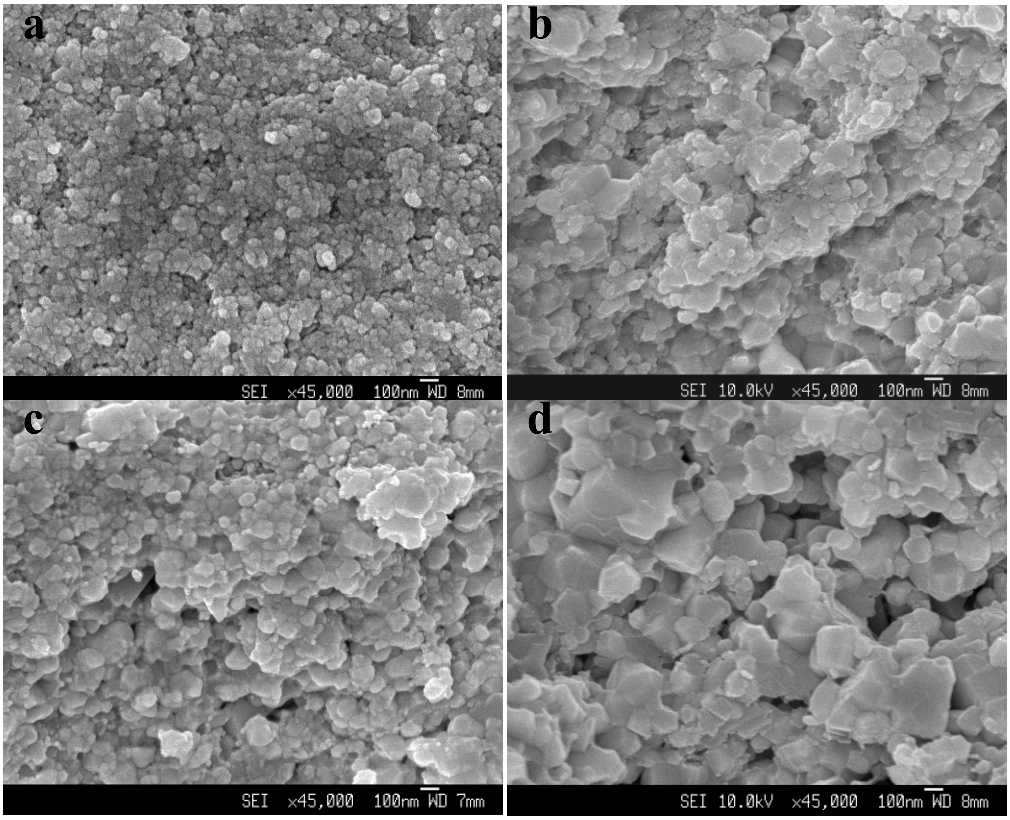

Figure 4.4-2: Typical FESEM images of fractured surfaces of the hot pressed pellet samples prepared with undoped $CoSb_3$ (Co_8Sb_{24}) (a) and Ni-doped $Co_{8-x}Ni_xSb_{24}$ (x=1 (b), x=1.25 (c) and x=1.5 (d)) nano-particles.

Typical TEM images of undoped $CoSb_3$ and Ni-doped $Ni_{1.25}Co_{6.75}Sb_{24}$ are showed in Figure 4.4-3(a) and (b) indicating that the grain sizes are distributed in a wide range of around 50 nm to hundreds of nanometers after hot press processing. And the surfactants have been removed during the hot press processing. According to phonon scattering mechanism mentioned in the literature, the grain with a particular grain size can scatter phonons of a corresponding wave-length. Hence, the wide range distributions of grain size of nanostructured undoped $CoSb_3$ and Ni-doped $CoSb_3$ are expected to scatter more phonons in a wide range of wave-length.

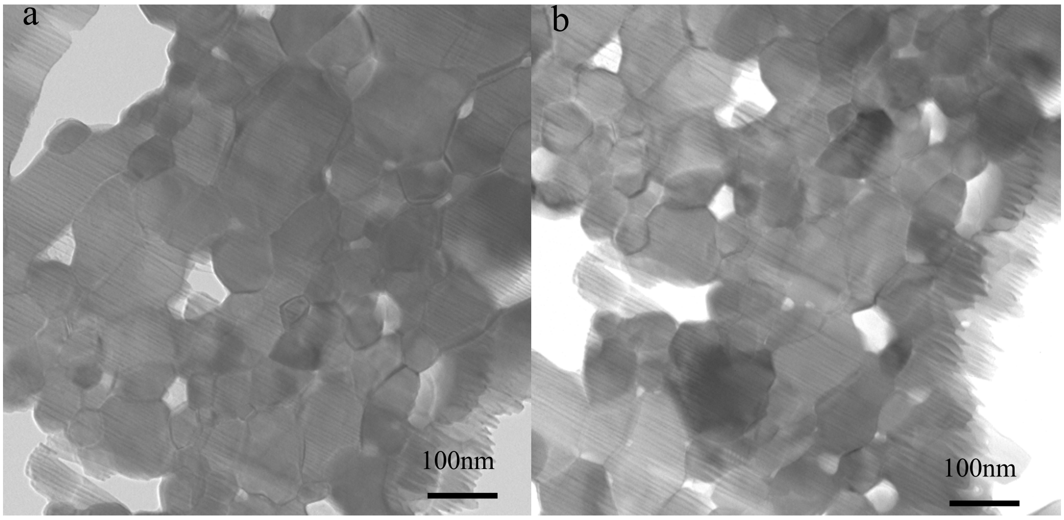

Figure 4.4-3: Typical TEM images of sample undoped $CoSb_3$ (a) and Ni-doped $Ni_{1.25}Co_{6.75}Sb_{24}$ (b) after hot pressing process.

Figure 4.4-4 is a high resolution TEM image of Ni-doped sample $Ni_{1.25}Co_{6.75}Sb_{24}$ to show the grain boundaries (a) (in red oval) and crystallinity (b). The clean grain boundaries and good crystallinity are prerequisites to achieve low electrical resistivity.

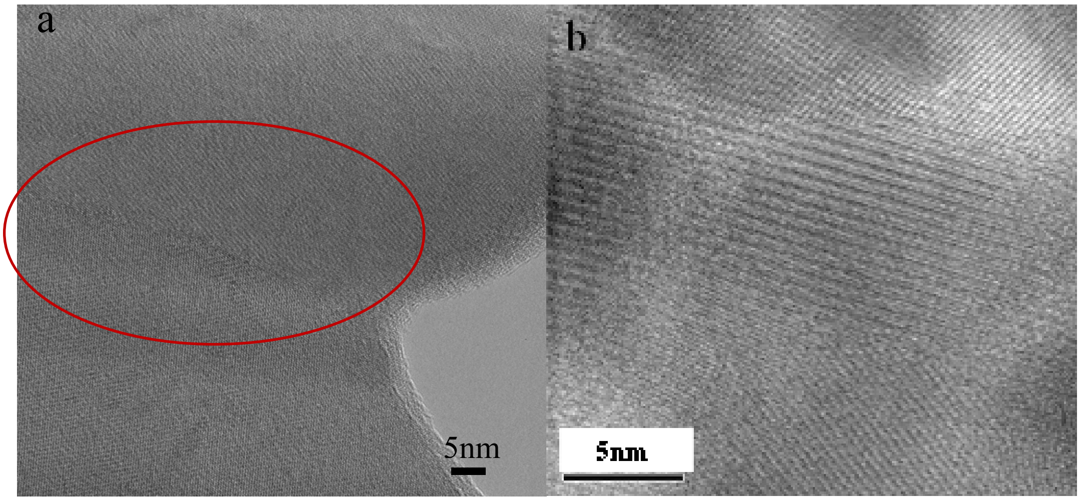

Figure 4.4-4: Typical HRTRM images of image of Ni-doped sample $Ni_{1.25}Co_{6.75}Sb_{24}$ to show the grain boundaries (a) (in red oval) and crystallinity (b).

As discussed in the XRD results, after hot pressing, the Sb phase were observed for all the pellet samples prepared from the undoped $CoSb_3$ and Ni-doped $Co_{8-x}Ni_xSb_{24}$ (x=1, x=1.25 and x=1.5) nano-particles. Here, the XRD results are confirmed by TEM techniques. Figure 4.4-5 shows a typical TEM image of these impurity Sb clusters (in black rectangle) with elemental analysis by EDX.

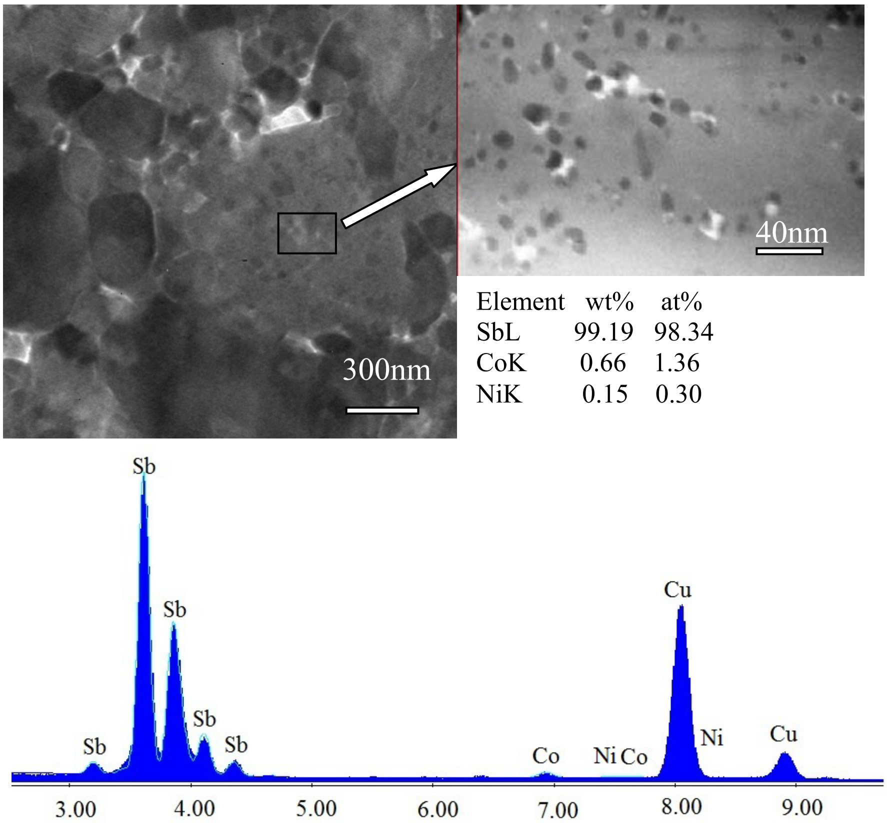

Element	wt%	at%
SbL	99.19	98.34
CoK	0.66	1.36
NiK	0.15	0.30

Figure 4.4-5: A typical TEM image and EDX results of impurity Sb cluster (in black rectangle).

4.4.3 Electrical properties

4.4.3.1 Carrier concentration

The carrier concentration is a very important parameter that affects both the electrical resistivity and Seebeck coefficient as described in literature [16]. The carrier concentrations of the samples were determined by Hall measurement at room temperature and the results are shown in Figure 4.4-6. For the undoped $CoSb_3$, the carrier concentration value is positive, which indicates that the major carriers of this sample are holes. However, after doping, the carrier concentration changes from positive to negative which means that the major carriers have changed from holes to electrons donated by the n-type dopants. In addition, the absolute carrier concentration values have also increased with Ni-doping content at relative low doping level which means that Ni atoms successfully substitute Co atoms and generate more electrons. However, the carrier concentration decreased with the doping level further increase. One possible reason is that when dopant Ni goes into the lattice of skutterudite, it will give one more electron than Co to the lattice. In order to keep the valence balance, more Sb will go into the lattice to act as a hole donor. The holes contributed by Sb will compensate the electrons given by dopants and decrease the nett carrier concentration with electron as major carriers.

The excess Sb in the alloys also has an effect on the carrier concentration. There are two types of Sb remaining in the alloy: excess Sb atoms in the lattice forming the crystal structure of skutterudite and elemental Sb as impurity which are detected in the XRD pattern. Based on the previous work, for the excess Sb in the lattice, acting as a hole-donor, gives holes conduction and increase the p-type carrier concentration [108]. However, obviously, elemental Sb gives electron conductions, namely, contributes as n-type carriers. For the p-type undoped $CoSb_3$, the p-type carrier concentration is enhanced by the Sb remaining in lattice and partially compensated by elemental Sb impurity. On the contrary, for n-type Ni-doped $Co_{8-x}Ni_xSb_{24}$ (x=1, x=1.25 and x=1.5) the n-type carrier concentration is enhanced by elemental Sb impurity and partially compensated by the Sb remaining in the skutterudite lattice. Therefore, the resultant carrier concentration from Hall measurement only reflects the nett value. For our Ni-doped samples, the sample $Co_{6.75}Ni_{1.25}Sb_{24}$ possesses the maximum carrier concentration.

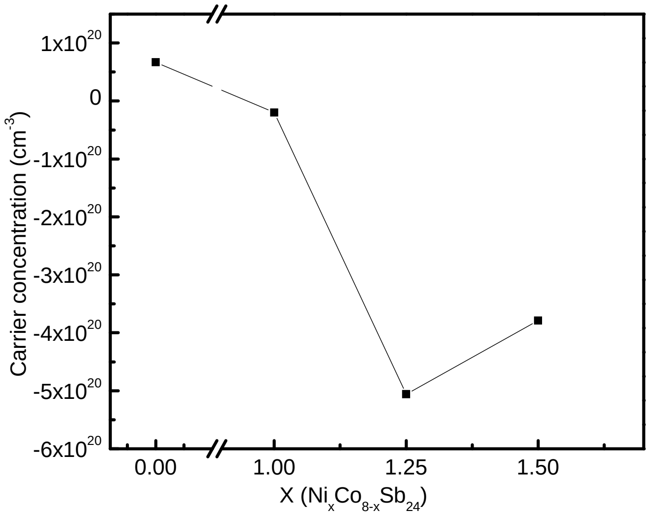

Figure 4.4-6: The dependence of the carrier concentration versus Ni content at room temperature.

4.4.3.2 Electrical resistivity

The electrical resistivity plotted as a function of temperature for the hot pressed undoped $CoSb_3$ and Ni-doped $Co_{8-x}Ni_xSb_{24}$ (x=1, x=1.25 and x=1.5) samples are shown in Figure 4.4-7. After doping with Ni, the resistivity decreased greatly. For the undoped $CoSb_3$, the electrical resistivity decreased with temperature, indicating a semiconductor behavior. However, the Ni-doped samples showed a metal-like behavior, i.e. the electrical resistivity increased with temperature indicating a heavily doped semiconductor.

Overall, the electrical resistivity has the reversed trend to that of carrier concentration since the electrical resistivity can be expressed as: $1/\rho = n(p)e\mu$, n indicates that the major carrier is electron and p stands for hole. The resistivity first decreased with nickel content which has the same trend as that of carrier concentration. The sample $Ni_{1.25}Co_{6.75}Sb_{24}$ has the lowest resistivity within the measurement temperature range due to its high carrier concentration. This value (~5×10^{-6} Ω·m) is comparable to the value of metal (×10^{-7} Ω·m) and also much lower than the value of 1.43×10^{-5} Ω·m for sample with the highest figure-of-merit *ZT* value among Ni-doped $CoSb_3$ samples reported so far [109]. We believe that the impurity Sb plays an important role in reducing electrical resistivity. As discussed in the carrier concentration part, elemental Sb gives more electron conduction contributing more n-type carriers and reduces electrical resistivity. The sample $Ni_{1.5}Co_{6.5}Sb_{24}$ possesses the highest resistivity. As mentioned in the carrier concentration discussion, with the n-type doping level increasing, more Sb will go into the lattice to act as hole donor in order to keep valence balance. The major carrier electrons are partially compensated by the holes donated by the Sb subsiding in the lattice of skutterudite and lead to the decrease in carrier concentration as well as increase in electrical resistivity.

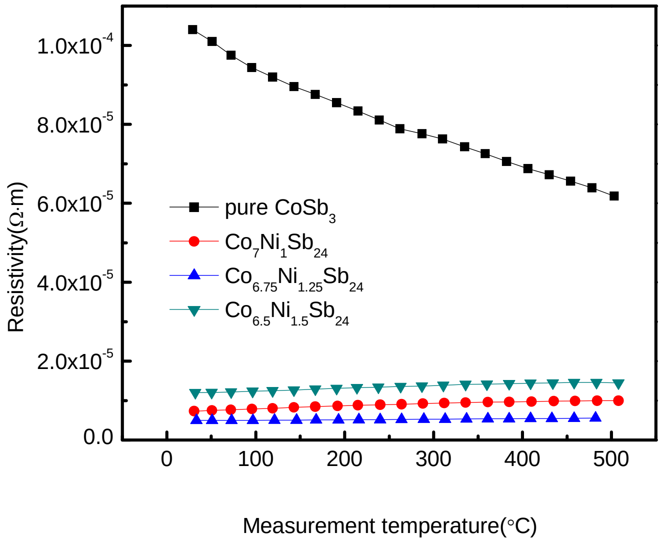

Figure 4.4-7: The temperature dependence of the electrical resistivity of hot pressed undoped $CoSb_3$ and Ni-doped $Co_{8-x}Ni_xSb_{24}$ (x=1, x=1.25 and x=1.5) samples.

4.4.3.3 Seebeck Coefficient

Figure 4.4-8 shows the temperature dependence of the Seebeck coefficient of the hot pressed undoped $CoSb_3$ and Ni-doped $Co_{8-x}Ni_xSb_{24}$ (x=1, x=1.25 and x=1.5) samples.

All the three Ni-doped samples showed negative Seebeck coefficient values over the whole temperature range investigated. This indicates that the samples are all n-type with the major carriers being electrons. For the undoped samples, the Seebeck coefficient values are positive which means that the major carriers are holes. These results are consistent with the Hall measurement results and confirm the substitution of Co by Ni.

The absolute values of the Seebeck coefficient for all samples increased with temperature reaching a maximum at around 400~450 °C and then decreased with temperature. For the Ni-doped samples, the Seebeck coefficient first increased with increasing Ni-doping content at a relative low doping level. Both the $Ni_{1.25}Co_{6.75}Sb_{24}$ and $Ni_{1.5}Co_{6.5}Sb_{24}$ samples possessed almost the same Seebeck coefficient values over the whole measurement temperature range. This is the results of filter effect and carrier concentration. As discussed in the section 4.4.2, the average grain size of sample $Ni_{1.25}Co_{6.75}Sb_{24}$ is smaller than that of $Ni_{1.5}Co_{6.5}Sb_{24}$. When the length of grains is small (i.e. the density of grain boundaries is high), the possibility of carriers with relatively high energy passing through the potential barrier of these high density grain boundaries are much higher that of carriers with relatively low energy. This leads to the increase in Seebeck coefficient as the grain size decreases. Hence, the absolute value Seebeck coefficient of sample $Ni_{1.25}Co_{6.75}Sb_{24}$ should be higher than that of sample $Ni_{1.5}Co_{6.5}Sb_{24}$ due to its smaller grain size. However, the absolute value of Seebeck coefficient of sample $Ni_{1.25}Co_{6.75}Sb_{24}$ was compensated by its higher carrier concentration, since Seebeck coefficent decreases with increasing carrier concentration. Both filter effect and carrier concentration lead to the similar Seebeck coefficient of these two samples.

The effect of impurity Sb on the Seebeck coefficient is also investigated. For materials with more than one type of charge carrier, the Seebeck coefficient should be expressed as $S = \sum_i \left(\frac{\sigma_i}{\sigma} \right) S_i$, where σ_i and S_i are partial electrical conductivity and partial thermopower associated with the *i*th group of carriers [110-112]. For the undoped $CoSb_3$, the Seebeck coefficient (*S*) of $CoSb_3$/Sb can be rewritten as:

$$S = \frac{\sigma_{CoSb_3}}{\sigma_{CoSb_3} + \sigma_{Sb}} S_{CoSb_3} + \frac{\sigma_{Sb}}{\sigma_{CoSb_3} + \sigma_{Sb}} S_{Sb} \qquad (4.5)$$

and transformed into

$$S = S_{CoSb_3} + \frac{\sigma_{Sb}}{\sigma_{CoSb_3} + \sigma_{Sb}} \left(S_{Sb} - S_{CoSb_3} \right) \qquad (4.6)$$

since Sb is a metal and S_{Sb} is much less than S_{CoSb3}, one can expect that the second term in Equation (4.6) is negative and therefore, *S* of binary phase material should be lower than that of single phase $CoSb_3$ system. Consequently, comparing with pure undoped $CoSb_3$ prepared by traditional method (whose maximum Seebeck coefficient value is around 200V/K for p-type), a marked decrease in *S* for undoped $CoSb_3$ is observed. Similarly, according to Equation (4.6), the remaining elemental Sb also decreases the overall Seebeck coefficient of Ni-doped $Co_{8-x}Ni_xSb_{24}$ (x=1, x=1.25 and x=1.5) and the absolute value of Seebeck coefficient are smaller than the best reported values (~300 μV/K) [109].

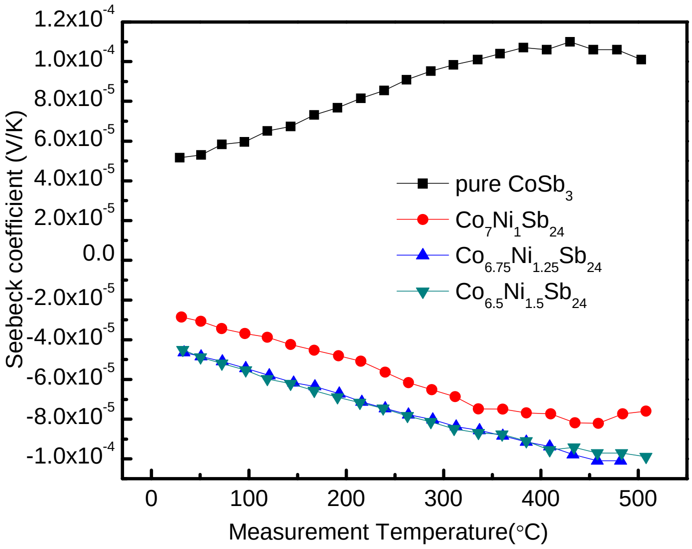

Figure 4.4-8: The temperature dependence of the Seebeck coefficient of hot pressed undoped $CoSb_3$ and Ni-doped $Co_{8-x}Ni_xSb_{24}$ (x=1, x=1.25 and x=1.5).

4.4.3.4 Power factor

Based on the Seebeck coefficient and electrical resistivity results, the power factor (α^2/ρ) of these samples were calculated (see Figure 4.4-9). Due to its very low electrical resistivity and high Seebeck coefficient, the sample $Ni_{1.25}Co_{6.75}Sb_{24}$ possessed the best electrical property with a maximum power factor of 1.84×10^{-3} $Wm^{-1}K^{-2}$ at about 450 °C. Compared with the undoped $CoSb_3$, whose highest power factor is 1.84×10^{-4} $Wm^{-1}K^{-2}$, the value has increased by 10 times. Compared with values reported in the literature, the maximum power factor of sample $Ni_{1.25}Co_{6.75}Sb_{24}$ is lower than the sample with similar doping level (~2.2×10^{-3} $Wm^{-1}K^{-2}$ at 450 °C) due to its smaller Seebeck coefficient caused by the elemental Sb impurity.

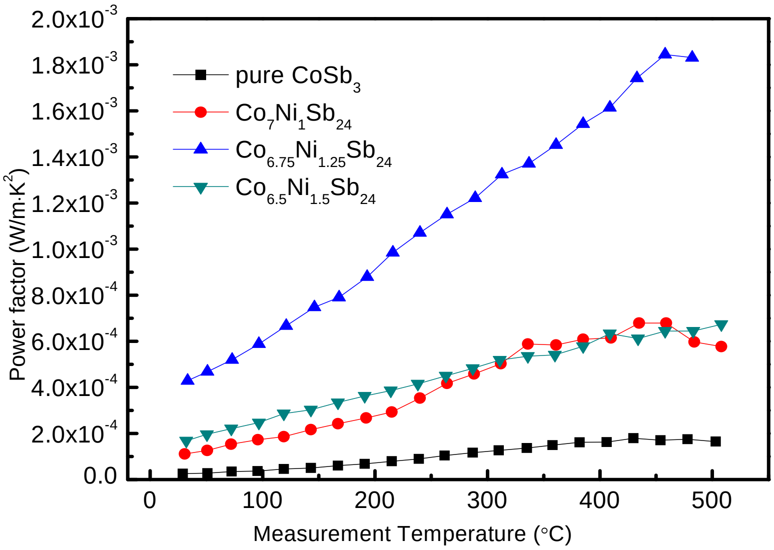

Figure 4.4-9: The temperature dependence of the power factor of hot pressed undoped $CoSb_3$ and Ni-doped $Co_{8-x}Ni_xSb_{24}$ (x=1, x=1.25 and x=1.5) samples.

4.4.4 Thermal properties

Figure 4.4-10(a) shows the temperature dependence of the total thermal conductivity for the various samples. The thermal conductivity of a material is the sum of two contributions, namely the carrier thermal conductivity and the lattice thermal conductivity, $\kappa = \kappa_c + \kappa_l$, , where κ_c and κ_l are thermal conductivities contributed by charge carriers and lattice, respectively. The carrier thermal conductivity was estimated using the Wiedemann-Franz's law, $\kappa_c = \frac{LT}{\rho}$, where L is the Lorentz number, taken as 2.45×10^{-8} V^2K^{-2} for our samples, ρ is the electrical resistivity and T is the absolute temperature in Kelvin [5]. The lattice thermal conductivity κ_l for the samples can then be obtained by subtracting κ_c from κ, and the results are shown in Figure 4.4-10(b).

The lattice thermal conductivity of micron-sized $CoSb_3$ is more than 8 W/m·K at 50 °C (to be discussed later in Chapter 5). As compared, the lattice thermal conductivity of the nanostructured undoped $CoSb_3$ was significantly reduced to 1.94 W/m·K at the same temperature which is comparable to the value (~2 W/m·K) reported by Zhao's group where solvothermal route was applied to synthesized nano-particles followed by hot pressing process [70]. As predicted by theoretical analysis, nanostructuring is an effective way to reduce thermal conductivity [113,114]. According to Rayleigh scattering regime, the scattering cross section varies as $\sigma \propto b^6 / \lambda^4$, where b is the size of the scattering particles and λ is the phonon wavelength. The grain boundaries of nanostructures (shown as Figure 4.4-3 and Figure 4.4-4) scatter the relatively long-wavelength phonons which carry more heat than that of short-wavelength phonons [20]. The phonon scattering by the high density of grain boundaries is the main contributor to reduce lattice thermal conductivity. Meanwhile, Sb clusters (see Figure 4.4-5) can also act as phonon scatters to scatter its corresponding wavelength phonons and further reduce the lattice thermal conductivity.

In the nanostructured Ni-doped $Co_{8-x}Ni_xSb_{24}$ (x=1, x=1.25 and x=1.5), similar to that of undoped $CoSb_3$, the high density of grain boundaries and Sb cluster both act as phonon scatterers to reduce the lattice thermal conductivity. In addition to grain boundaries, the point defects created due to substitution can also scatter the relatively shorter wavelength phonons and cause an overall reduction in the lattice thermal conductivity. The same phenomenon has also been reported for Sn- and Te-doped skutterudites that the additional dopants could reduce the lattice thermal conductivity remarkably by introducing "point defect scattering" mechanism [115,116]. Besides the Ni dopants, the excess Sb in the skutterudite lattice can also lead to structure distortion and produce point defects. In addition to point defect scattering, another important reason is the Ni substitution which increases the carrier concentration greatly and leads to a stronger "electron–phonon scattering" to scatter phonons and reduce lattice thermal conductivity [117]. All these effects lead to the lattice thermal conductivity of Ni-doped samples to decrease with increased Ni-doping content, and sample $Ni_{1.5}Co_{6.5}Sb_{24}$

possessed the lowest lattice thermal conductivity among the three Ni-doped samples. Hence, in the Ni-doped nanostructured $CoSb_3$, it can be concluded that the low lattice thermal conductivity is contributed mostly by nanostructuring and doping (point defect scattering and phonon- electron scattering).

The lowest lattice thermal conductivity of Ni-doped nanostructured samples is 0.64 W/m·K at 300 °C which is very near to the lowest theoretical lattice thermal conductivity of ~0.3 W/m·K [118]. Such a low thermal conductivity has never been reported even in an unfilled skutterudite. Comparing with unfilled nanostructured $CoSb_3$ whose grain size are around several hundred nanometers, the grain size of our samples prepared by polyol method together with hot press are really small (shown in Figure 4.4-3) and the density of grain boundaries are high. The high density of grain boundaries can scatter more phonons and reduce the lattice thermal conductivity.

It is also worth noting that the $Ni_{1.25}Co_{6.75}Sb_{24}$ sample has the highest total thermal conductivity among all the samples which is comparable with reported values [109,119]. This is a result of the large contribution from carrier thermal conductivity. On the contrary, the undoped $CoSb_3$ and sample $Ni_{1.5}Co_{6.5}Sb_{24}$ with relative high electrical resistivity have the lowest total thermal conductivity among all the samples. According to Wiedemann-Franz's law, $\boldsymbol{\kappa}_c = \frac{\boldsymbol{LT}}{\boldsymbol{\rho}}$, the sample with lower resistivity has higher carrier thermal conductivity. Here, we can see the reduction of electrical resistivity and thermal conductivity cannot happen simultaneously. This is the reason why we have to optimize the carrier concentration i.e. doping content in order to improve the overall figure-of-merit *ZT* value.

The densities of our samples are all in a relative narrow range (88%~89% of theoretical value). Hence, the effect of porosity on thermal conductivity is not considered here.

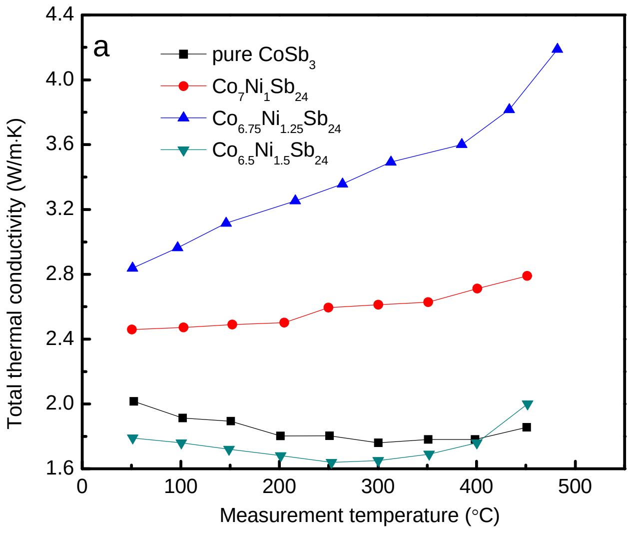

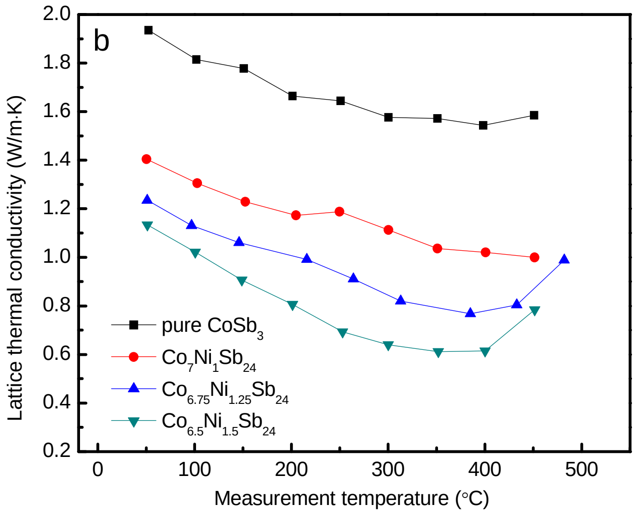

Figure 4.4-10: Temperature dependences of total thermal conductivity (a) and lattice thermal conductivity (b) of the hot pressed undoped $CoSb_3$ and Ni-doped $Co_{8-x}Ni_xSb_{24}$ (x=1, x=1.25 and x=1.5) samples.

4.4.5 Figure-of-merit *ZT* value

Based on the results of electrical resistivity, Seebeck coefficient and thermal conductivity, the dimensionless figure of merit, *ZT* values for all the samples were calculated and are presented in Figure 4.4-11. The highest *ZT* value of 0.33 was attained at about 480 °C for the $Ni_{1.25}Co_{6.75}Sb_{24}$ sample. As compared with the undoped $CoSb_3$ sample whose highest *ZT* value is 0.067, the value had increased by nearly 5 times. Hence, doping is an effective way to improve electrical properties by increasing carrier concentration and reducing electrical resistivity, and at the same time, the introduced dopants can scatter phonons more effectively and further reduce the lattice thermal conductivity. The decrease in both electrical resistivity and lattice thermal conductivity after doping are the primary reasons for the remarkable improvement in the figure-of-merit, *ZT* value. However, this value is still smaller than the reported best *ZT* value (0.7 at 525 °C) of nanostructured Ni-doped $CoSb_3$ due to its smaller Seebeck coefficient caused by the Sb impurity [109]. But compared with the samples which also have impurity phase whose highest *ZT* value is 0.2 at 377 °C, the *ZT* value has increase by more than 50% [119].

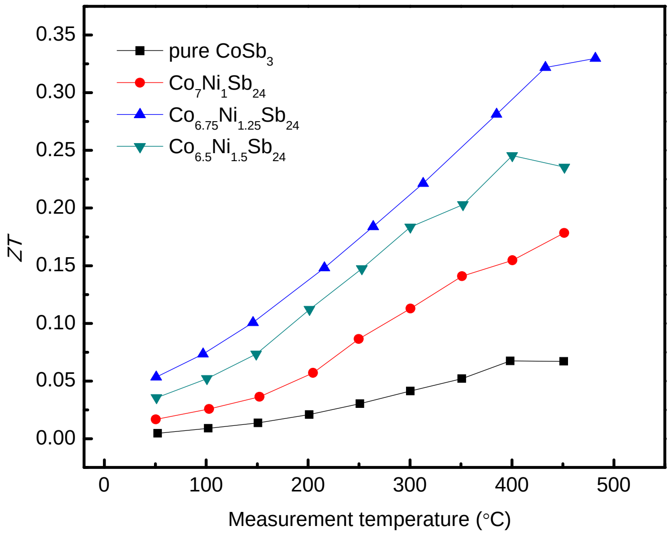

Figure 4.4-11: Temperature dependences of the dimensionless figure-of-merit *ZT* value of the hot pressed undoped $CoSb_3$ and Ni-doped $Co_{8-x}Ni_xSb_{24}$ (x=1, x=1.25 and x=1.5) samples.

4.5 Conclusions

1. High purity $CoSb_3$ nanoparticles have been successfully synthesized via a modified polyol process. The $CoSb_3$ phase was synthesized at a relatively low temperature via a rapid, one-pot synthesis route. The optimized reaction conditions were determined to be at a temperature of 195 °C for 15 mins. N-type Ni-doped $CoSb_3$ nanoparticles have also been successfully synthesized using a similar process.

2. The dopant content is optimized. Among the Ni-doped samples, $Ni_{1.25}Co_{6.75}Sb_{24}$ has the highest *ZT* value of 0.33 at 480 °C. Comparing with the undoped $CoSb_3$ whose highest *ZT* value is only 0.067, this value (0.33) is nearly 4 times higher than that of undoped $CoSb_3$.

3. Nanostructuring is an effective way to reduce the lattice thermal conductivity. For undoped $CoSb_3$, comparing with its corresponding bulk material, both total and lattice thermal conductivities have been greatly reduced. After doping, the lattice thermal conductivity was further reduced, and the lowest lattice thermal conductivity of sample $Ni_{1.5}Co_{6.5}Sb_{24}$ is 0.64 W/m·K which is very close to the lowest theoretical lattice thermal conductivity of ~0.3 W/m·K.

4. After doping, the electrical resistivity has been greatly reduced with major carrier changed. The electrical resistivity of sample $Ni_{1.25}Co_{6.75}Sb_{24}$ is as low as 5×10^{-6} Ω·m which is comparable with the value of metal ($\times10^{-7}$ Ω·m). However, comparing with the electrical resistivity, doping has less impact on absolute value of Seebeck coefficient. This is due to the existence of elemental Sb impurity which has a negative effect on Seebeck coefficient for both p-type undoped and n-type Ni-doped $CoSb_3$.

5. The as-synthesized undoped $CoSb_3$ nano-particles will be used as nano-inclusion to prepare p-type nanocomposites in Chapter 5. The n-type Ni-doped $Ni_{1.25}Co_{6.75}Sb_{24}$ nano-particles will be used as nano-inclusions in the preparation of n-type nanocomposites in Chapter 6 due to its lowest electrical resistivity and highest *ZT* value among the Ni-doped samples.

Chapter 5

Preparation and Characterization of p-type $CoSb_3$-based nanocomposites

5.1 Introduction

In this chapter, three types of p-type nanocomposites with various nano-inclusions and micron-sized matrix were prepared. The main goal of the nanocomposite method proposed in this work is to introduce randomly dispersed second phase nanostructures with high density of grain boundaries into a micron-sized matrix to reduce the overall thermal conductivity by scattering more phonons, and meanwhile maintain the electrical properties of matrix by keeping the good connection of bulk matrix. The figure-of-merit, *ZT* value will be consequently enhanced.

Our work started with undoped $CoSb_3$ acting both as nano-inclusion and micron-sized matrix (C-C composite system) to study the effect of nano-inclusion on the thermal conductivity. The results showed that both the total and lattice thermal conductivities are reduced after introducing nano-inclusions which can scatter more phonons and reduce the thermal conductivity. Besides thermal conductivity, the electrical properties of the nanocomposite were also found to be affected by nano-inclusions, because of the different preparation methods used to prepare the nano-inclusions and the micron-sized matrix that gave rise to different electrical properties of these two phases i.e. the nano-inclusions have much higher carrier concentration than that of micron-sized matrix. Based on the investigation of C-C nanocomposite system, another two types of nanocomposites whose nano-inclusions have much lower or comparable carrier concentration than that of micron-sized matrix were prepared and the effects of nano-inclusion on both thermal and electrical properties were investigated. The micron-sized matrix and nano-inclusions for each type of nanocomposite systems as well as their carrier concentration comparison are listed in Table 5.1-1. For the C-C nanocomposite system, the carrier concentration of the nano-inclusion was much higher than that of micron-sized matrix. The C-Z system refers to the system where the micron-sized matrix is the undoped $CoSb_3$ and the nano-inclusion is ZrO_2. For this nanocomposite system, an extreme case was studied by using an insulator as the nano-inclusions which had a much lower carrier concentration than that of the micron-sized matrix. The F-C nanocomposite system refers to the system where the micron-sized matrix is the La-, Ca-filled skutterudite and the nano-inclusion is the undoped $CoSb_3$. In this system, the matrix and nano-inclusion have comparable carrier concentrations. Other than studying the thermal conductivity, the effects of nano-inclusion impact on electrical properties, namely carrier concentration, electrical resistivity, Seebeck coefficient, and the overall *ZT* value of these three types of nanocomposites, were investigated to determine a suitable material type that can be used as nano-inclusions to improve the overall thermoelectric properties via the nanocomposite approach.

Table 5.1-1 The micron-sized matrix and nano-inclusions for each type of nanocomposite systems and their carrier concentration comparison to prepare the three types of nanocomposite systems.

System	Micron-sized matrix	Carrier concentration comparison	Nano-inclusions
1 C-C	$CoSb_3$	<<	$CoSb_3$
2 C-Z	$CoSb_3$	>>	ZrO_2
3 F-C	$La_{0.35}Ca_{0.35}Fe_{1.5}Co_{2.5}Sb_{12.03}$	≈	$CoSb_3$

5.2 C-C nanocomposite system

P-type undoped nanostructured $CoSb_3$ synthesized via polyol method was chosen as the nano-inclusions while micron-sized p-type $CoSb_3$ matrix was prepared through solid state reaction. The weight percentage of nano-inclusions was varied from 10% to 30%.

5.2.1 Preparation of matrix

For the pure $CoSb_3$ system, before the matrix was determined, a series of experiment with different Sb content (0.1at%, 0.25at% and 0.5at%) was conducted to optimize the amount of excess Sb in pure $CoSb_3$. The carrier concentrations obtained at room temperature for each sample are summarized in Table 5.2-1 below:

Table 5.2-1: Carrier concentration of samples with different amount of excess Sb in $CoSb_3$

Sample name	Composition	Carrier concentration (cm^{-3})
0.1at% Sb excess	$CoSb_{3(1+0.1\%)}$	6.5×10^{16}
0.25at% Sb excess	$CoSb_{3(1+0.25\%)}$	1.9×10^{17}
0.5at% Sb excess	$CoSb_{3(1+0.5\%)}$	9.3×10^{17}

The major carriers of these three samples are holes. From the carrier concentration results, it is noted that the carrier concentration increased with increasing amount of Sb excess and sample with 0.5at% Sb excess possesses the highest carrier concentration at room temperature.

The electrical properties, i.e. electrical resistivity, Seebeck coefficient and power factor, of these samples were also measured from room temperature to above 500 °C. The electrical resistivity plotted as a function of temperature for all the samples is shown in Figure 5.2-1. All these three samples show a semiconductor behaviour i.e. electrical resistivity decreases with increasing temperature. The resistivity decreases with increasing Sb excess content which is in agreement with the carrier concentration results. However, the decrease in electrical resistivity with temperature is not obvious for the sample with 0.5at% excess Sb. This is because the high Sb content in the lattice weakens its semiconductor behaviour [5].

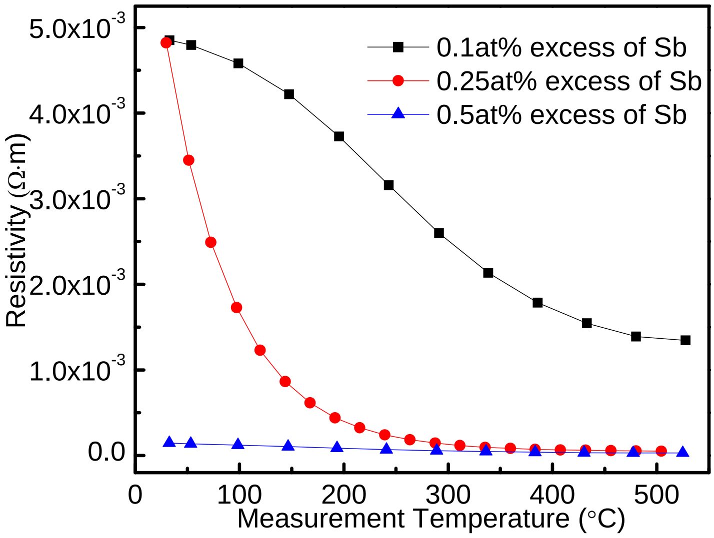

Figure 5.2-1: Temperature dependence of resistivity for the samples with different amount of excess Sb.

Figure 5.2-2 (a) shows the Seebeck coefficient as a function of temperature for all the samples with different amount of excess Sb. The positive values of the Seebeck coefficient indicate that the samples are p-type which is in agreement with the carrier concentration results. The Seebeck coefficient initially increases with excess Sb, but it decreases with further increase in excess Sb. Such a trend was also reported in Liu's work [120]. One possible reason is that, for the sample with 0.5at% excess Sb, not all the Sb goes into the lattice and the residual metal Sb contributes to electrical conduction and results in the decrease in Seebeck coefficient. Among all the samples, the sample with 0.25% excess Sb achieved the highest Seebeck coefficient value of 2.3×10^{-4} (V/K) at around 200 °C. Based on the results of electrical resistivity and Seebeck coefficient, the power factors of each sample are calculated according to the equation: $PF= \alpha^2/\rho$, where α is Seebeck coefficient and ρ is resistivity, and are shown in Figure 5.2-2 (b). Among all the samples, the sample with 0.25at% excess Sb exhibits the highest Seebeck coefficient as well as the best electrical properties with a maximum power factor value of 3.6×10^{-4} $Wm^{-1}K^{-2}$ at around 350 °C.

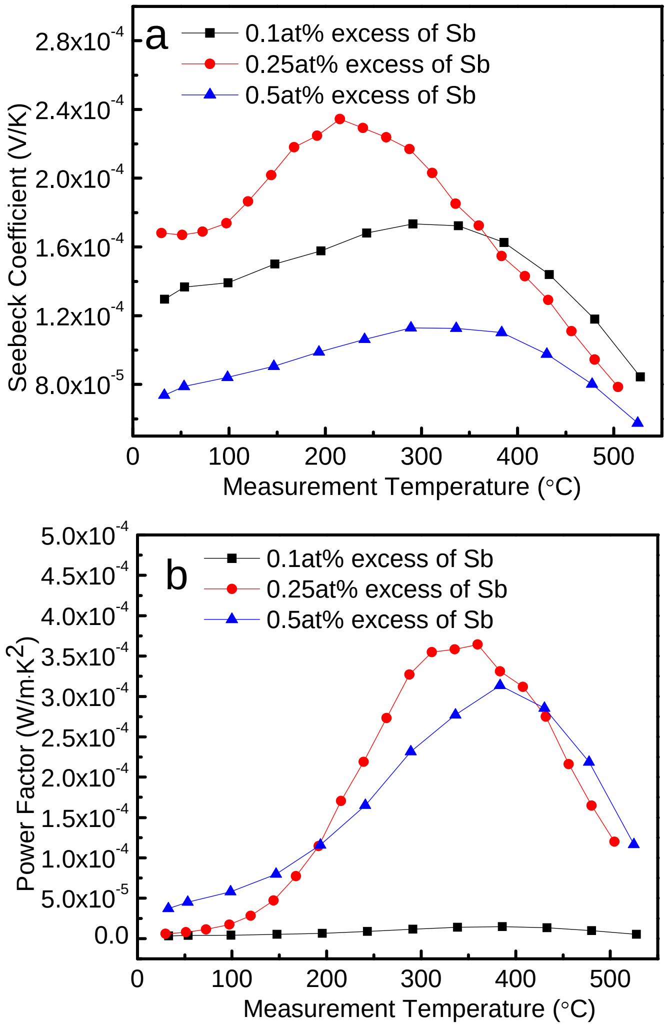

Figure 5.2-2: Temperature dependences of Seebeck coefficient (a) and power factor (b) for the samples with different amount of excess Sb.

The results showed that the sample with 0.25at% excess Sb possesses the best electrical properties, i.e. the highest power factor among these three samples. Hence, the sample with 0.25at% excess Sb was chosen as the p-type nanocomposite matrix.

5.2.2 Phase analysis

Figure 5.2-3 shows the XRD patterns of the hot-pressed nanocomposites pellets with various amounts of nano-inclusions. The samples are named as c-c nano XX%, where XX indicates the weight percentage of nano-inclusions in the sample, and c-c means C-C nanocomposite system in which both the micron-sized matrix and nano-inclusions are undoped $CoSb_3$ phase. C-micron refers to the sample composed of 100wt% micron-sized $CoSb_3$ particles, which is the reference sample without any nano-inclusions.

After the hot pressing process, it was observed that additional diffraction peaks corresponding to trace amount of the Sb phase were detected in the samples containing $CoSb_3$ nano-inclusions. The intensity of the Sb peaks was also observed to increase with increasing amount of $CoSb_3$ nano-inclusions in the nanocomposites. It was noted that there is no additional Sb phase in the sample c-micron after the hot pressing process, indicating that the additional Sb does not come from the micron-sized particles and was instead contributed from the $CoSb_3$ nano-particles. This observation is consistent to that described in Chapter 4, where the detection of the Sb phase in the hot pressed pellets was attributed to the meta-stable nature of the synthesized nano-sized Sb-rich $CoSb_3$ phase, where the excess Sb precipitated out from the lattice and existed as elemental Sb phase during hot pressing.

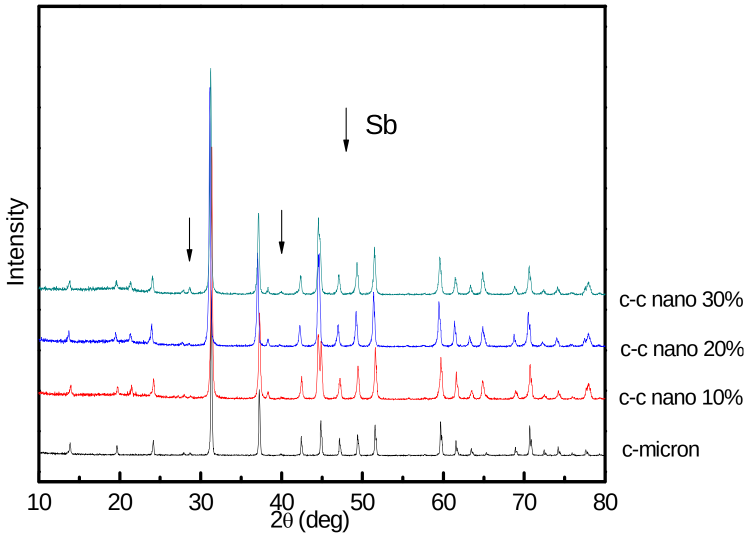

Figure 5.2-3: XRD patterns of the hot-pressed nanocomposite sample pellets prepared with various amount of nano-inclusions where both the nano-inclusions micron-sized matrix were undoped $CoSb_3$.

5.2.3 Microstructure analysis

Figure 5.2-4 (a) shows a typical fractograph of the c-micron sample obtained via solid state reaction, which consists of only micron-sized grains. Figures 5.2-4 (b), (c) and (d) correspond to the fractographs for the c-c nano 10%, c-c nano 20% and c-c nano 30% sample respectively, showing a combination of nano-sized and micron-sized grains. These nanocomposites exhibit similar microstructures except for the amount of nano-inclusions distributed among the micron-sized matrix. Most of these nano-inclusions existed as clusters (the region in the red oval shows a typical nano-cluster in Figure 5.2-4(b)) residing mainly between the micron-sized grains. The numbers of nano-clusters are observed to increase with increasing weight percentage of nano-inclusions. TEM image detailing the grain boundaries of the nanocomposite samples is shown in Figure 5.2-5 for sample c-c nano 10%. Both nano-grains and micron-grains are shown in the image. Obviously, after introducing nano-grains, the density of grain boundaries has increased which is beneficial to the reduction of thermal conductivity. Similar to that observed from

FESEM images, the nano-grains are mainly distributed at the boundaries of the micron-grains.

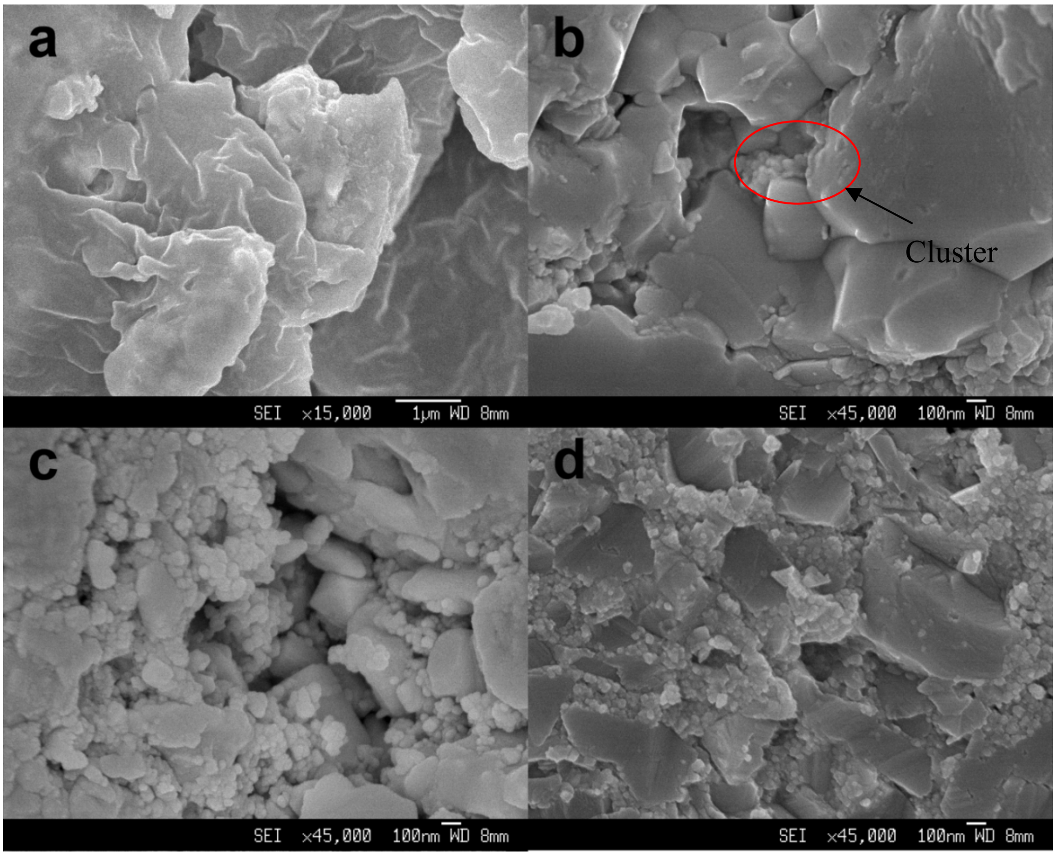

Figure 5.2-4: Typical FESEM images of the fractured surfaces of (a) c-micron, (b) c-c nano 10%, (c) c-c nano 20%, and (d) c-c nano 30% samples.

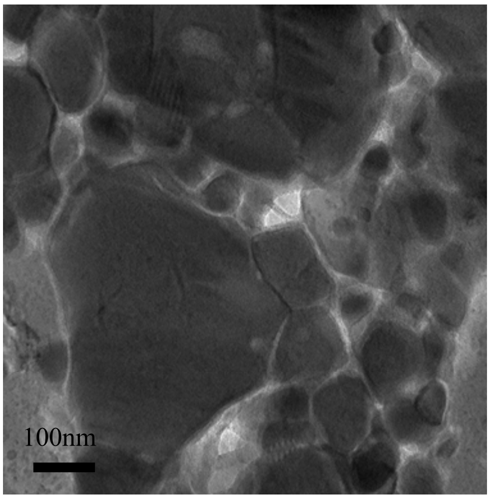

Figure 5.2-5: Typical TEM images of sample c-c nano 10% to show the details of the connection between the micron-sized matrix and nano-inclusions.

5.2.4 Electrical properties

5.2.4.1 Carrier concentration

Hall measurements were carried out to determine the carrier concentration at room temperature. The dependence of the carrier concentration versus the weight percentage of nano-inclusions for the C-C nanocomposite system is shown in Figure 5.2-6. The carrier concentrations of all the samples are positive which indicates a p-type conduction mechanism and the major carrier is holes. The carrier concentration of the c-micron sample is only about 1.9×10^{17} cm^{-3} which is much lower than that of the c-nano 100% (sample composed of 100wt% of undoped $CoSb_3$ nano-particles) whose carrier concentration is 6.7×10^{19} cm^{-3}. The change in the carrier concentration is related to the excess Sb atoms in the lattice of nano-inclusions which acts as a hole-donator to increase the carrier concentration of holes which was already discussed in Chapter 4.

In general, the carrier concentration of nanocomposite samples increased with increasing content of nano-inclusion which has higher carrier concentration than that of micron-sized matrix. By adding only 10wt% of nano-inclusions, the carrier concentration of the c-nano 10% sample was increased nearly 40 times (as compared to the c-micron sample) to 7.3×10^{18} cm^{-3}. Here, one can see that when the carrier concentration of the nano-inclusion is much higher than that of the matrix, and the carrier concentration of the nanocomposite is very sensitive to the nano-inclusion. However, disregarding the size effect on the carrier concentration, the sample of c-c nano 20% can be considered as a nanocomposite whose matrix is c-c nano 10% with 10wt% of c-nano 100% as nano-inclusion. In this case, the matrix c-c nano 10% and nano-inclusion c-nano 100% have comparable carrier concentrations (7.3×10^{18} cm^{-3} and 6.7×10^{19} cm^{-3}, respectively) and the increase in carrier concentration from sample c-c nano 10% to c-c nano 20% is moderate and not as obvious as that from sample c-micron to c-c nano 10%. Similarly, the carrier concentration also increased slightly from sample c-c nano 20% to c-c nano 30%. Here, we can reach the conclusion that when the nano-inclusion and micron-sized matrix have comparable carrier concentration, the carrier concentration of nanocomposite samples varies moderately after mixing, and this phenomenon will be further confirmed and discussed in the F-C nanocomposite system later.

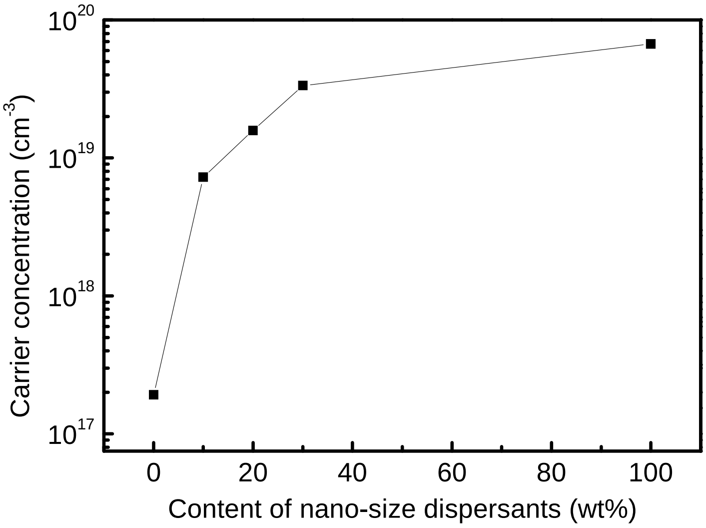

Figure 5.2-6: The dependence of carrier concentration versus the weight percentage of nano-inclusions at room temperature for the nanocomposite samples with undoped CoSb$_3$ as both nano-inclusion and micron-sized matrix.

5.2.4.2 Electrical resistivity

The electrical resistivity plotted as a function of temperature for all the samples is shown in Figure 5.2-7(a). The resistivities of the c-micron and c-nano 100% samples are observed to decrease with temperature over the whole temperature range measured, which indicates semiconductor behaviour. However, for the nanocomposite samples: c-c nano 10%, c-c nano 20% and c-c nano 30% (see magnified plot in Figure 5.2-7(b)), the resistivity initially increased with temperature up to 150 °C, which indicates metallic behaviour instead. With further increase in temperature, the resistivities of these samples then start to decrease with temperature indicating semiconductor behaviour. It is very exciting that all these three nanocomposite samples have lower resistivity than both the c-micron and c-nano 100% samples except for the c-c nano 10% sample which exhibits higher electrical resistivity at near room temperature range. By adding only 10wt% of nano-inclusions, the resistivity decreased significantly as compared to the sample c-micron by one order of magnitude. And at relative low temperature range (<200 °C), the electrical resistivities of three nanocomposite samples decrease with content of nano-inclusion. Both these two phenomena are in agreement with the results of carrier concentration. However, with the temperature further increase, the values of electrical resistivity overlap. This may be related to electrical transport mechanism changing from metallic behaviour to semiconductor behaviour with the temperature increasing and will be studied later.

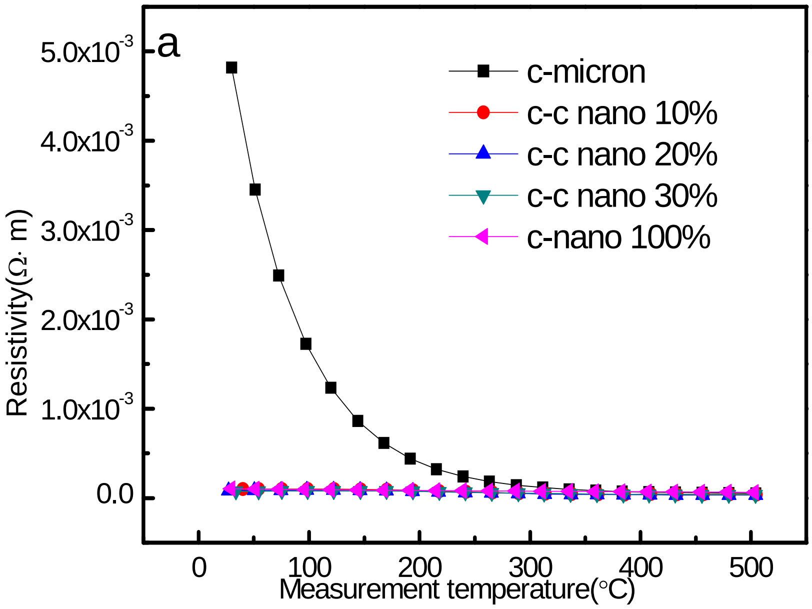

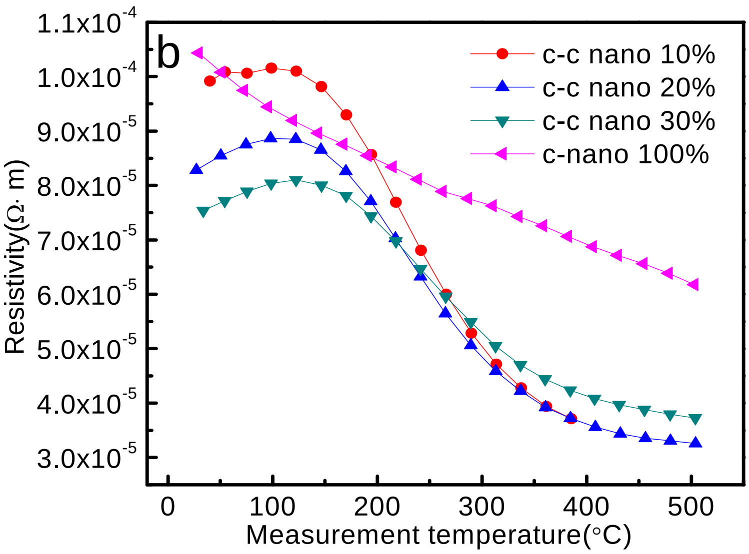

Figure 5.2-7: (a) Temperature dependences of resistivity for the nanocomposite samples with various amount of nano-inclusions with undoped CoSb$_3$ as both nano-inclusions and micron-sized matrix. (b) Magnified plot of samples c-c nano 10%, c-c nano 20%, c-c nano 30% and c-nano 100%.

Within the measured temperature range, both the c-micron and c-nano 100% samples exhibit semiconductor behaviour. Thermally activated conduction (TAC) model is applied to analysis the electrical conduction mechanism. The plots of *log(ρ)* versus inverse temperature for these two samples are presented in Figure 5.2-8(a). The solid line is fitted to the equation [108]:

$$\rho(T) = \rho_0 \exp\left(E_g / 2k_B T\right) \tag{5.1}$$

where ρ_0 is a constant, k_B is Boltzmann constant and E_g is the band gap. For sample c-micron, E_g was determined to be 0.43 eV, which is close to the reported band gap of CoSb$_3$ (0.5 eV [9]). This E_g level is likely due to a deep acceptor level or even the intrinsic band gap. For sample c-nano 100%, E_g of 0.04 eV was obtained. This is much smaller than the band gap of CoSb$_3$ indicating that E_g of c-nano 100% arises from a shallow acceptor level, which is much easier to be activated and hence cause an increase in the carrier concentration. This is in agreement with the carrier concentration results.

In order to understand the conduction mechanism of the nanocomposites samples (c-c nano 10%, c-c nano 20% and c-c nano 30%), the temperature range was divided into two parts. From room temperature to 150 °C, the samples showed metallic behaviour as indicated from the resistivity results. For temperatures above 150 °C, the electrical resistivity showed semiconductor behaviour. It was proposed that small polaron hopping conduction (SPHC) model can be applied to explain this phenomenon [121]. In this model, the electrical resistivity vary as a function of temperature as shown in Equation 5.2,

$$\rho(T) = \frac{1}{pe\mu} = \frac{T}{C}\exp\left(\frac{E_p}{k_B T}\right) \tag{5.2}$$

where p is the carrier concentration, e is the electrical charge of carrier, μ is the carrier mobility, C is a constant, E_p is the activation energy of polaron hopping, and k_B is the Boltzmann constant. By plotting $ln(\rho/T)$ vs $1/T$ for the c-c nano 10%, c-c nano 20% and c-c nano 30% samples (Figures 5.2-8(b), (c) and (d)), it was found that the temperature dependence of the resistivity in the semiconductor-like temperature range of these nanocomposites fits well to the SPHC model. The activation energy, E_p in the semiconductor temperature range was determined by performing a linear fit of the experimental data. The E_p data obtained for the nanocomposite samples with different amount of nano-inclusions are presented in the respective plots. It is also noted that the activation energy E_p decreases with increasing amount of nano-inclusions. The decrease in the activation energies indicates that the transport of the polarons becomes easier with increasing amount of the nano-inclusions. This is the result of the movement of the acceptor level towards the valence band with increasing amount of nano-inclusions.

Meanwhile, the increased amount of nano-inclusions also caused enhanced distortions on the sites neighbouring the polaron, and such distortions aid in the motion of the carriers leading to the carrier mobility increase with the increasing amount of nano-inclusions. It should be mentioned that the resistivity of the c-nano 100% sample is higher than all three nanocomposite samples. In the c-nano 100% sample, the carriers are scattered by the high density of grain boundaries and carriers due to its nanostructure and highest carrier concentration among all the samples. The reduction in the carrier mobility results in a higher electrical resistivity.

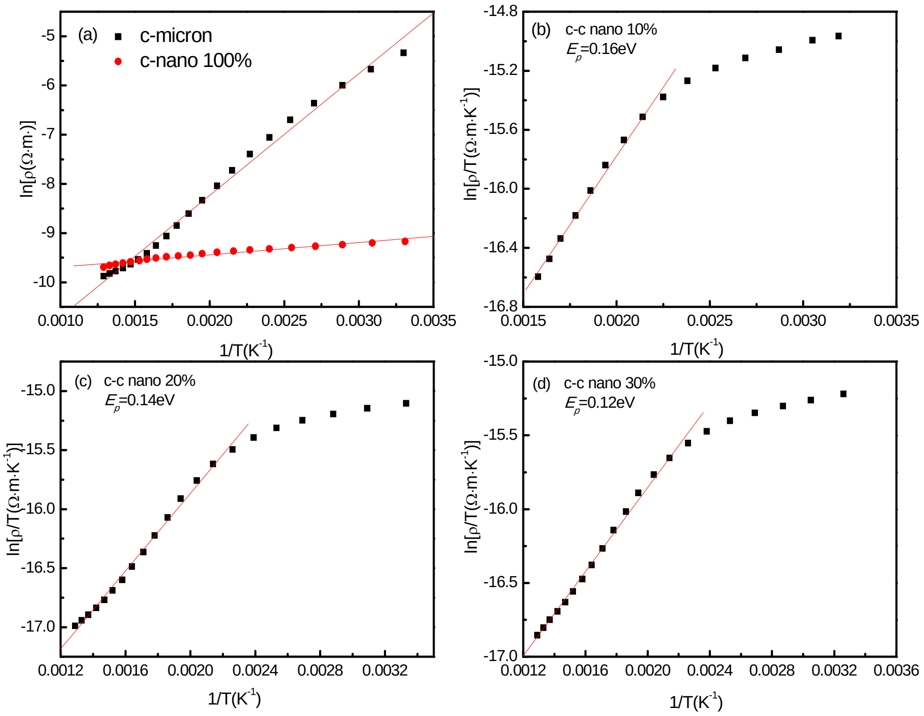

Figure 5.2-8: (a) Plots of ln(ρ) vs 1/T for samples c-micron and c-nano 100%. Plots of ln(ρ/T) vs 1/T for (b) sample c-c nano 10%, (c) c-c nano 20%, and (d) c-c nano 30%.

5.2.4.3 Seebeck coefficient

Figure 5.2-9 shows the Seebeck coefficient as a function of temperature for all the samples with different amount of nano-inclusions. The positive values indicate that the samples are p-type. Even though the values of Seebeck coefficient are scattered at relative high temperature range, in the temperature range below 425 °C, it is observed that the Seebeck coefficient of the samples investigated decreased with increasing amount of nano-inclusions. This phenomenon is in an agreement with that of carrier concentration, since the Seebeck coefficient decreases with increasing carrier concentration.

Besides carrier concentration, effective mass can also alter Seebeck coefficient value. The carrier effective mass, $m_p{}^*$ was estimated using the Seebeck coefficient and carrier concentration data by assuming a single parabolic band model with acoustic phonon scattering as a predominant carrier scattering mechanism. In this model [16], the Seebeck coefficient α can be expressed as follows (our samples are all p-type):

$$\alpha_p = \frac{k_B}{e}\left(\frac{2F_1(\eta)}{F_0(\eta)} - \eta\right) \qquad (5.3)$$

The carrier concentration p can be expressed as follows:

$$p = 4\pi\left(\frac{2m_p{}^* k_B T}{h^2}\right)^{\frac{3}{2}} F_{\frac{1}{2}}(\eta) \qquad (5.4)$$

where, p is the carrier concentration, $m_p{}^*$ stands for effective mass of the carrier (holes for our samples), k_B is the Boltzmann's constant, η is the reduced Fermi energy, F_x is the Fermi integral of order x, T is the absolute temperature. The effective mass of the carriers for all the samples were calculated and plotted against the weight percentage of nano-inclusions as shown in Figure 5.2-10. From the results, one can see that the effective mass increased with the increasing amount of nano-inclusions. In general, carrier concentration and effective mass are the two main factors affecting the Seebeck coefficient values. The Seebeck coefficient, α_p increased with increasing effective carrier mass, $m_p{}^*$, and decreases with increasing carrier concentration, p. Even though the effective masses increase with the increasing amount of nano-inclusions, the Seebeck coefficient of our samples was found to decrease with the increasing amount of nano-inclusions. Hence, in our samples, it can be concluded that carrier concentration has a larger effect than the effective carrier mass on the final Seebeck coefficient values.

For sample c-micron and c-nano 100%, the Seebeck coefficient reached a maximum at about 200 °C and 425 °C, respectively. For temperature above 200 °C for the sample c-micron and 425 °C for c-nano 100%, with the temperature further increasing, the increased carrier concentration activated by a deep acceptor level becomes the dominant factor to affect the Seebeck coefficient, and caused a decrease in the Seebeck coefficient. For c-c nano 10%, c-c nano 20% and c-c nano 30% samples, the Seebeck coefficient reached the maximum values at temperatures ranging from 250 °C to 300 °C. At temperatures above 300 °C, the Seebeck coefficients of these three samples decreased. The decrease in Seebeck coefficient in these samples is due to the small polaron hopping activation within this temperature range which led to the increase in carrier concentration.

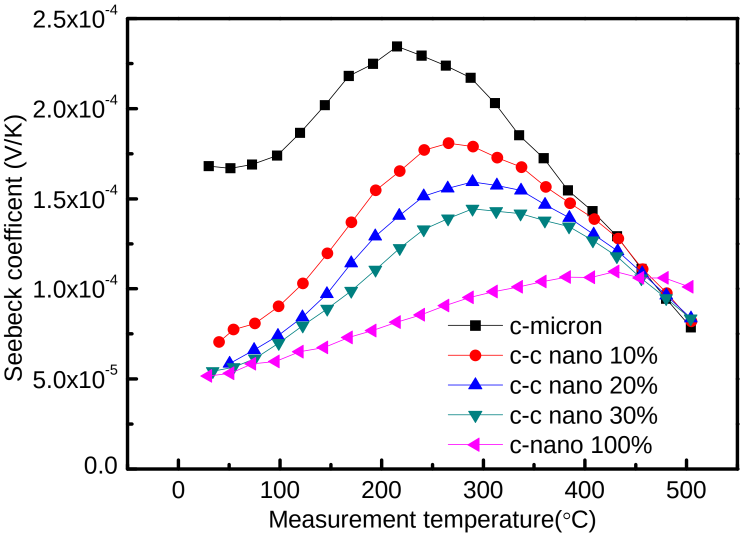

Figure 5.2-9: Temperature dependences of Seebeck coefficient for the nanocomposite samples with various amounts of nano-inclusions with undoped $CoSb_3$ as both nano-inclusions and micron-sized matrix.

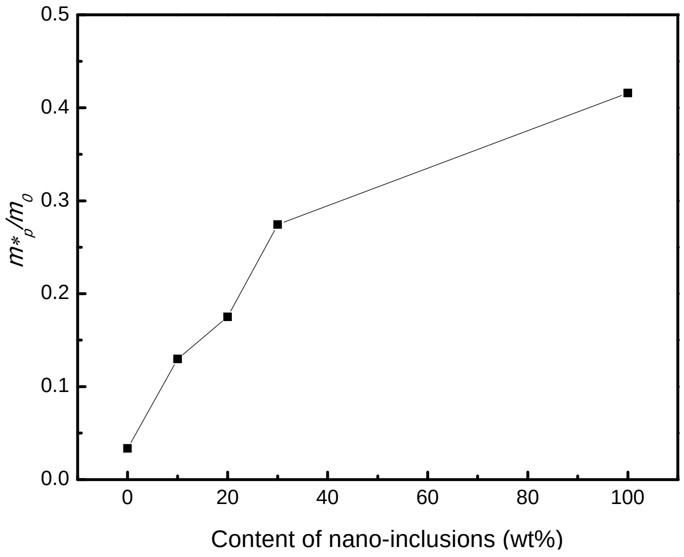

Figure 5.2-10: The dependence of the effective mass with the weight percentage of nano-inclusions at room temperature for the nanocomposite samples with various amounts of nano-inclusions with undoped $CoSb_3$ as both nano-inclusions and micron-sized matrix.

5.2.4.4 Power factor

Based on the Seebeck coefficient and electrical resistivity results, the power factor (α^2/ρ) of these samples were calculated and presented in Figure 5.2-11. The power factors for all the nanocomposite samples are higher than that of the matrix (sample c-micron) and nano-inclusions (c-nano 100%) and decrease with the content of nano-inclusion. The increase in power factor for nanocomposite samples are mainly due to reduction or increase in electrical resistivity or carrier concentration via the introduction of nano-inclusion with higher carrier concentration. Calculated by the equation, $PF= \alpha^2/\rho$, among all the samples, sample c-c nano 10% exhibits the best electrical properties with a maximum power factor value of 6.33×10^{-4} $Wm^{-1}K^{-2}$ at around 310 °C. As compared to the matrix (sample c-micron with a maximum power factor value of 3.64×10^{-4} $Wm^{-1}K^{-2}$) and for the nano-inclusion (c-nano 100% with a maximum power factor value of 1.79×10^{-4} $Wm^{-1}K^{-2}$), the power factor of the nanocomposites have increased dramatically.

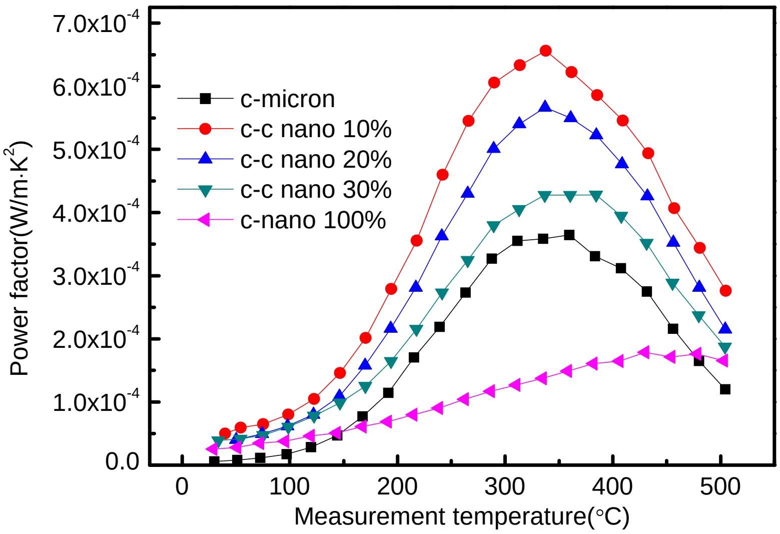

Figure 5.2-11: Temperature dependences of power factor for the nanocomposite samples with various amounts of nano-inclusions with undoped $CoSb_3$ as both nano-inclusions and micron-sized matrix.

5.2.5 Thermal properties

Figure 5.2-12(a) shows the temperature dependences of total thermal conductivity of all the samples. The lattice thermal conductivity κ_l for the samples obtained by subtracting κ_c from κ was also determined ($\boldsymbol{\kappa_c} = \frac{\boldsymbol{LT}}{\boldsymbol{\rho}}$ and $L=2.45\times10^{-8}\ V^2K^{-1}$), and the results are shown in Figure 5.2-12(b). As expected, the nano-inclusions play an important role in reducing the lattice thermal conductivity. The nano-scaled grain size of the nano-inclusions resulted in a high density of grain boundaries. These grain boundaries scatter and impede the movement of phonons which carry heat. This results in a reduction in the mean free path of phonons and lead to further reduction in both lattice and total thermal conductivity. As the amount of nano-inclusion increases, i.e. the grain boundaries increase, the lattice thermal conductivity decreases over the entire temperature range measured. At 50 °C, the lattice thermal conductivity decreases about 4 times from 8.10 $Wm^{-1}K^{-1}$ (sample c-micron) to 1.94 $Wm^{-1}K^{-1}$ (sample c-nano 100%).

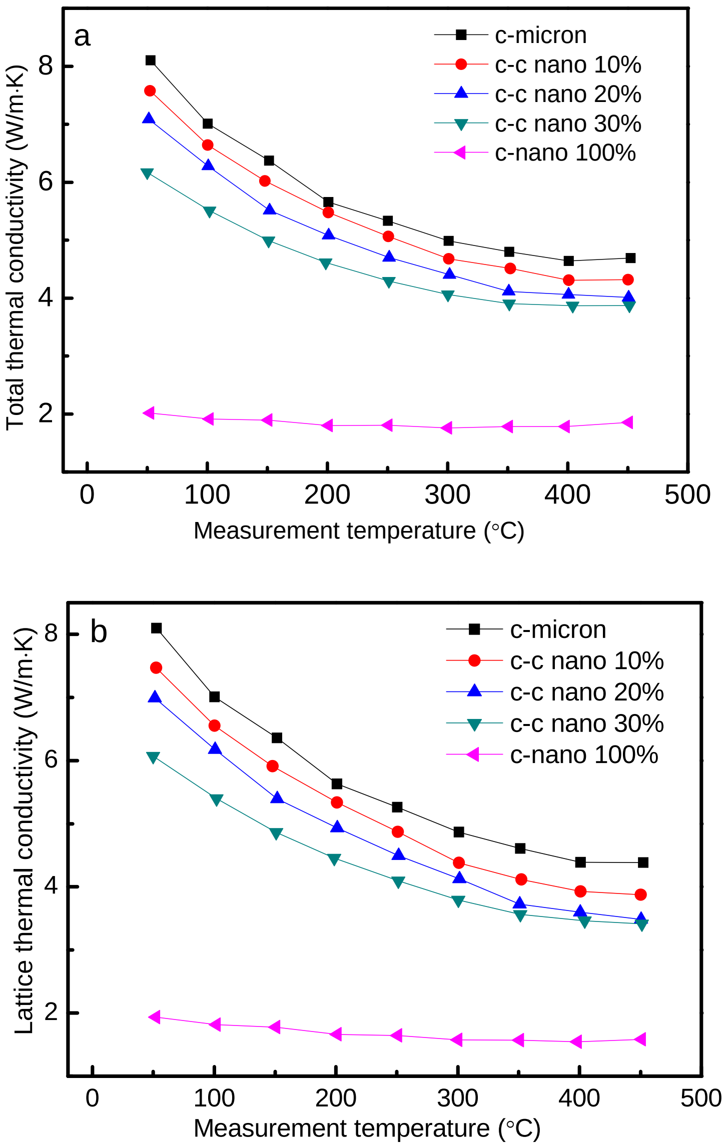

Figure 5.2-12: Temperature dependences of (a) total thermal conductivity, and (b) lattice thermal conductivity for the nanocomposite samples with various amounts of nano-inclusions with undoped $CoSb_3$ as both nano-inclusions and micron-sized matrix.

Porosity is another effect that can also reduce the thermal conductivity since the thermal conductivity of air (0.024 $Wm^{-1}K^{-1}$ at 25 °C) is also much smaller than that of micron-sized and nanostructured $CoSb_3$. The porosity can be considered as air dispersed in the matrix. The effect of porosity on the thermal conductivity was estimated using the following effective conductivity model [73],

$$\kappa_0 \approx \frac{\kappa_d}{1-\frac{3f}{2}} \qquad (5.5)$$

where κ_0 and κ_d are thermal conductivities of the non-dispersed and air-dispersed samples, respectively, and f is the volume fraction of air. For our tested samples, f is equal to the porosity which can be expressed as: $f = 1\text{-}relative\ density$. The relative density and the relationship between κ_0 and κ_d are listed in Table 5.2-2. From the results, one can see that the correcting coefficients $1/(1-3/2f)$ fall in a narrow range between 1.12 and 1.21 after calculation and the thermal conductivity of the corrected non-porous nanocomposites has the same trend as that of the air-dispersed samples, that is the thermal conductivity decreases with the increase in contents of nano-inclusions (Figure 5.2-13). Hence, after eliminating the effects of porosity, we can safely reach the conclusion that the introduced nano-inclusions are the main contributor in reducing the thermal conductivity rather than the porosity. Therefore, the effects of porosity will not be discussed in the other nanocomposite systems in the subsequent chapters.

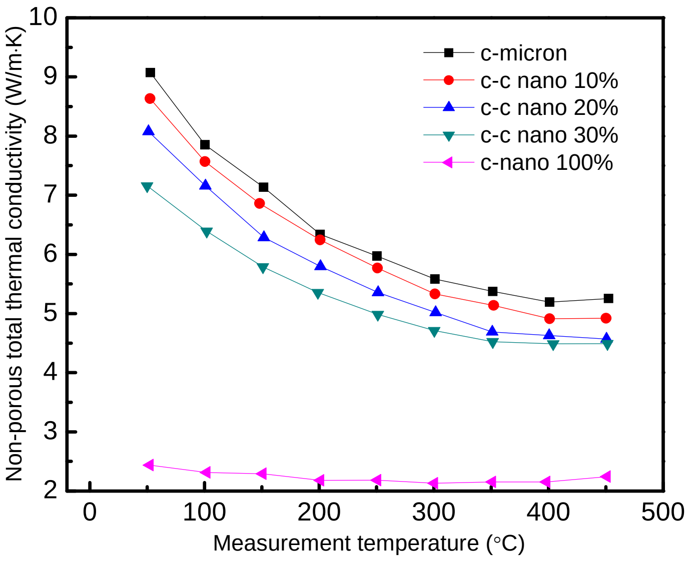

Figure 5.2-13: Temperature dependences of corrected non-porous total thermal conductivity for the nanocomposite samples with various amounts of nano-inclusions with undoped $CoSb_3$ as both nano-inclusions and micron-sized matrix.

Table 5.2-2: The relative density and relationship between κ_0 and κ_d of the samples with various amounts of nano-inclusions.

Sample	Relative density	$\kappa_0 \approx \kappa_d/(1-3/2f)$
c-micron	93%	$\kappa_0 \approx 1.12\ \kappa_d$
c-c nano 10wt%	92%	$\kappa_0 \approx 1.14\ \kappa_d$
c-c nano 20wt%	92%	$\kappa_0 \approx 1.14\ \kappa_d$
c-c nano 30wt%	91%	$\kappa_0 \approx 1.16\ \kappa_d$
c-nano 100wt%	88%	$\kappa_0 \approx 1.21\ \kappa_d$

5.2.6 Figure-of-merit *ZT* value

With the electrical resistivity, Seebeck coefficient and thermal conductivity results, the dimensionless figure of merit, *ZT* values for the samples are calculated and presented in Figure 5.2-14. The highest *ZT* value of 0.092 was obtained at about 400 °C for the c-c nano 10% sample. As compared to the c-micron sample, whose highest *ZT* value is 0.047, the value has nearly doubled. The decrease in the electrical resistivity of the nanocomposites is the most important contributor to the improvement in electrical property even though the improvement is slightly counteracted by the decrease in the Seebeck coefficient. Concurrently, the nano-inclusions of $CoSb_3$ in a micron-sized $CoSb_3$ matrix resulted in a reduction in the lattice thermal conductivity. Hence, due to the improvement in both the electrical and thermal properties, the *ZT* values of the nanocomposites are nearly doubled. These results are very exciting because it shows that nanocomposite approach can be an effective way to increase the figure-of-merit *ZT* value not only by decreasing the thermal conductivity, but at the same time, the electrical resistivity can also be decreased if the electrical resistivity of nano-inclusion is much smaller than that of the matrix.

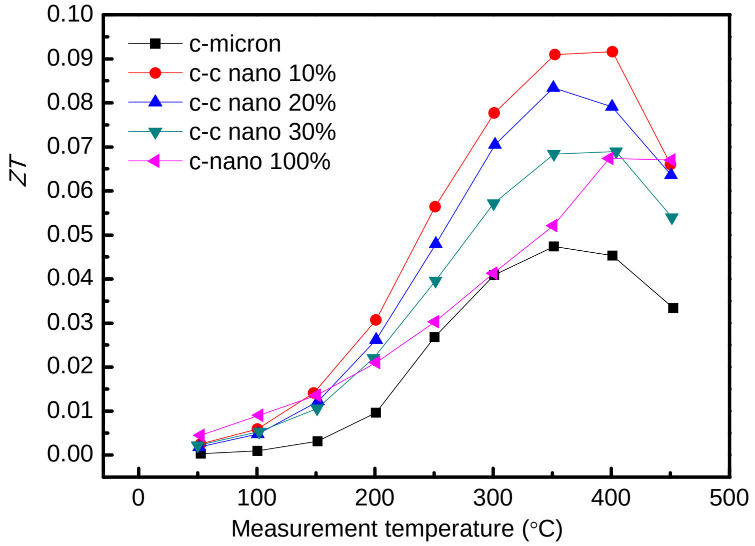

Figure 5.2-14: Temperature dependences of the dimensionless figure of merit ZT value for the nanocomposite samples with various amounts of nano-inclusions with undoped $CoSb_3$ as both micron-sized matrix and nano-inclusion.

5.3 C-Z nanocomposite system

The results of the C-C nanocomposite system showed that nanocomposite is an effective method to reduce lattice and total thermal conductivity. In this part of work, ZrO_2 nano-particles are chosen as nano-inclusions, since the thermal conductivity of ZrO_2 is in the range of 1.8~3.0 W/m·K, i.e. much lower than the micron-sized matrix $CoSb_3$ (around 8~10 W/m·K at room temperature), it is expected that the thermal conductivity of nanocomposites can be reduced by introducing nano-inclusions with lower thermal conductivity. In addition, another important role of the nano-inclusions is to act as phonon-scatterers due to its high density of grain boundaries, scattering more phonons and hence further reduce the lattice and total thermal conductivity of the nanocomposite samples, which can result in higher *ZT* values.

For electrical properties, the results of C-C composite system showed that when the carrier concentration of nano-inclusion is much higher than that of the micron-sized matrix, the resistivity of the nanocomposite samples can be greatly reduced. The reduction in the electrical resistivity ρ is main contributor in improving the overall electrical properties, i.e. the power factor (α^2/ρ) of the C-C nanocomposite system. In the C-Z nancomposite system, instead of reducing the electrical resistivity, we would like to explore the possibility of improving the power factor by increasing the value of Seebeck coefficient (α). Based on the results of the C-C nanocomposite system, it was shown that carrier concentration is the dominating effect on the final Seebeck coefficient, where the Seebeck coefficient value can be increased (reduced) by reducing (increasing) the carrier concentration. Hence, in the C-Z nanocomposite system, an extreme case of introducing insulator ZrO_2 nano-particles as nano-inclusions to reduce the carrier concentration and increase Seebeck coefficient was investigated. Meanwhile, energy barrier effect due to the phase interface between the micron-sized matrix and nano-inclusion will also be expected to enhance the Seebeck coefficient [75].

The results of the C-C nanocomposite system also showed that when the micron-sized matrix and nano-inclusion have very distinct carrier concentration, the electrical resistivity of nanocomposite sample can be greatly varied by the addition of only 10wt% nano-inclusions. Hence, in this part of the work, as the nano-inclusion is an insulator which has distinctly different electrical properties than that of micron-sized matrix, and in order not to reduce the electrical resistivity significantly, the contents of the insulator nano-inclusions were kept below 10wt%.

5.3.1 Phase analysis

Figure 5.3-1 shows the XRD pattern of the hot-pressed pellets obtained from the nanocomposites with ZrO_2 as nano-inclusions and $CoSb_3$ as micron-sized matrix. The ZrO_2 were commercially purchased and followed by ball milling for 3 h. The particle sizes of ball-milled ZrO_2 distributed in a range of 200 nm to 300 nm. The undoped $CoSb_3$

prepared by solid state reaction was still chosen as micron-sized matrix. The samples are named as c-z nano XX%, where XX indicates the weight percentage of nano-inclusions in the sample, and c-z refers to the C-Z nanocomposite system with ZrO_2 as the nano-inclusions and undoped $CoSb_3$ as the micron-sized matrix. From the XRD patterns, one can see that sample c-z nano 3% is in pure phase of skutterudite, no extra peaks even the peaks attributed by ZrO_2 are observed. With the content of ZrO_2 nano-inclusion further increased, the trace peaks attributed by ZrO_2 appeared for sample c-z nano 5% and c-z nano 7%.

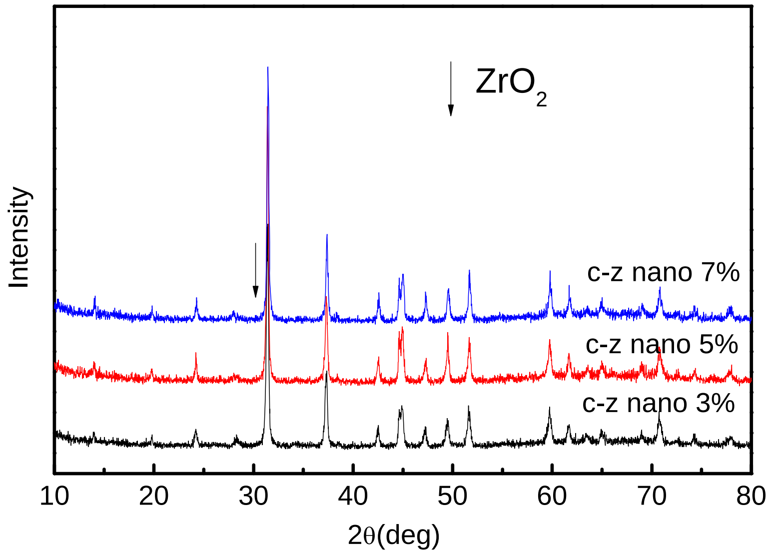

Figure 5.3-1: XRD patterns of the hot pressed nanocomposite sample pellets with various amounts of nano-inclusions with ZrO_2 as nano-inclusions and undoped $CoSb_3$ as micron-sized matrix.

5.3.2 Microstructure analysis

Figure 5.3-2 shows the typical FESEM images of the fracture surfaces of the samples from the C-Z nancomposite system. It can be seen that the average particle size of the ZrO_2 nano-inclusions is around 200~300 nm. After hot press, the particle size of ZrO_2 did not change too much and the dispersion of ZrO_2 are more scattered as compared to the other nanocomposite systems. This is because the sintering temperature (500 °C) is too low to densify ZrO_2. Similar to microstructures of the C-C nanocomposite system, most of these nano-inclusions existed as clusters residing at the grain boundaries of the micron-sized matrix.

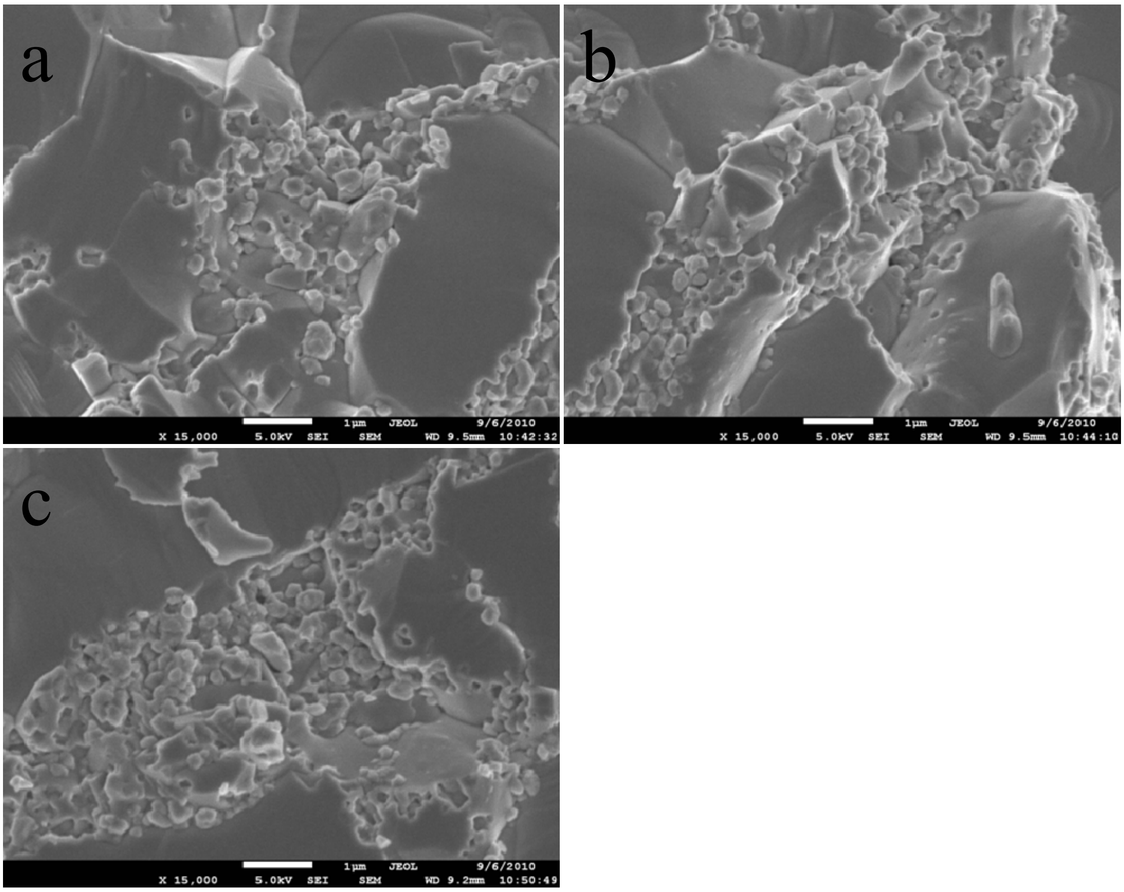

Figure 5.3-2: Typical FESEM images of the fracture surfaces of (a) c-z nano 3%, (b) c-z nano 5%, and (c) c-z nano 7% samples.

5.3.3 Electrical properties

5.3.3.1 Carrier concentration

The dependence of the carrier concentration versus the weight percentage of ZrO_2 nano-inclusions for the C-Z nanocomposite samples is shown in Figure 5.3-3. The carrier concentration values of all the samples are positive which indicates p-type conduction mechanism. The majority carriers did not change after the insulator nano-inclusions were introduced. However, the carrier concentrations decreased with increasing amount of insulator nano-inclusions. After introducing only 7wt% of nano-inclusions, the carrier concentration became more than 10 times smaller than that of micron-sized matrix. The carrier concentrations of all the nanocomposite samples are of the order of 10^{16} cm^{-3}, which is one order lower than that of the micron-sized matrix. Combining the results of C-C and C-Z systems, one can see that when the nano-inclusions have distinct carrier concentration compared to that of micron-sized matrix, the carrier concentration of nanocomposite samples are very sensitive to the addition of nano-inclusion and can change significantly just by adding a small amount of nano-inclusions. The carrier concentration of the nano-inclusions increased with the content of nano-inclusion when the nano-inclusion has higher carrier concentration than that of micron-sized matrix (C-C composite system) and otherwise decreased with content of nano-inclusions when the nano-inclusion has lower carrier concentration (C-Z composite system).

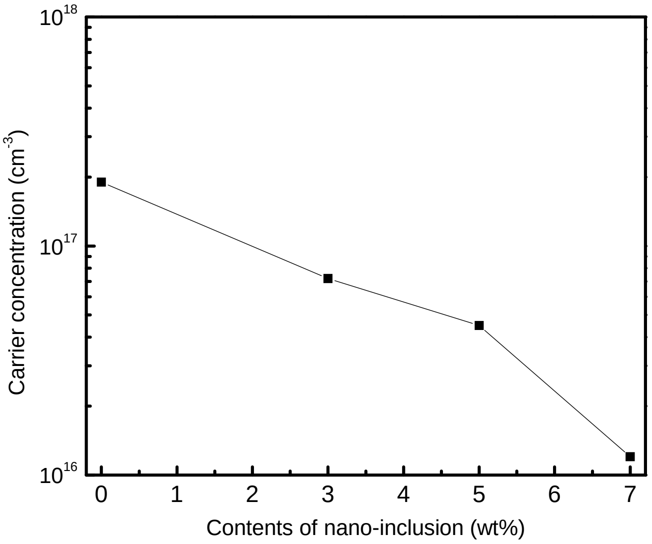

Figure 5.3-3: The dependence of carrier concentration versus weight percentage of nano-inclusions at room temperature for the nanocomposite samples with ZrO_2 as nano-inclusions and undoped $CoSb_3$ as micron-sized matrix.

5.3.3.2 Electrical resistivity

The electrical resistivity plotted as a function of temperature for all the samples with $CoSb_3$ as micron-sized matrix and ZrO_2 as nano-inclusions are shown in Figure 5.3-4. The resistivities of all the nanocomposite samples decreased with increasing temperature, which indicates semiconductor behaviour similar to that of the micron-sized matrix. Overall, the resistivity has the same trend as the carrier concentration, i.e. resistivity increases with increasing amount of insulator nano-inclusions. The change in the electrical resistivity for nanocomposite samples of C-Z system is not as obvious as that of C-C system. One possible reason is that, comparing with the nanocomposite samples in C-C system, the content of insulator nano-inclusion in C-Z system is relatively lower and the connection of micron-sized matrix is well maintained to keep the path of carrier remains unchanged. With the temperature increasing, the value of resistivity of nanocomposite samples became very close to each other, and this phenomenon was also observed in He's work [122]. A possible reason is that at high temperature range, the intrinsic band gap of micron-sized matrix has been thermally activated and the carrier concentration drastically increased leading to the reduction in carrier concentration caused by the nano-inclusions becomes less obvious.

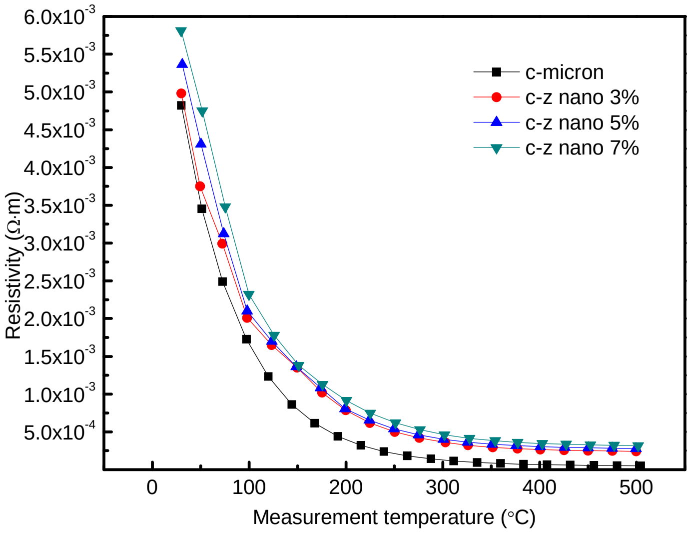

Figure 5.3-4: Temperature dependences of resistivity with various amounts of nano-inclusions for the nanocomposite samples with ZrO_2 as nano-inclusions and undoped $CoSb_3$ as micron-sized matrix.

5.3.3.3 Seebeck coefficient

The Seebeck coefficient plotted as a function of temperature for all the samples are shown in Figure 5.3-5. The positive Seebeck coefficient values confirmed that the samples are p-type. The Seebeck coefficient values increased with increasing temperature up to around 150 °C. Beyond 150 °C, the Seebeck coefficient values started to decrease with increasing temperature.

The overall Seebeck coefficient increased with increasing amount of the insulator nano-inclusions which is in agreement with other nanocomposite results [8,9]. In these nanocomposite samples, the nano-inclusions act as energy filters to scatter low energy electron which contribute less to the electrical conductivity leading to the band structure of matrix change and increase Seebeck coefficient. Meanwhile, the nano-inclusion can also cause defects and dislocation at the grain boundaries in the nanocomposite structures. And these defects can also act as energy filter to increase the overall Seebeck coefficient. Therefore, the Seebeck coefficient increases with nano-inclusions. Besides the low energy electrons scattering, carrier concentration is another important factor to affect Seebeck coefficient. In general, Seebeck coefficient increases with decreasing carrier concentration. The carrier concentration reduced due to the addition of the insulator nano-inclusions and lead to the increase in Seebeck coefficient values. At higher temperature (>300 °C), the results showed that the Seebeck coefficient values were not significantly affected by the insulator nano-inclusions which is also observed in He's work [122]. This is because at the higher temperature range, the drastic increase in carrier concentration due to the thermally activation of the deep acceptor level of the micron-sized matrix, make the value of carrier concentration for nanocomposite samples very close and lead to the Seebeck coefficient of all the samples to be of nearly the same values. Similarly, as discussed above, this deep acceptor level activation of micron-sized matrix also resulted in the close value of electrical resistivity of these three nanocomposite samples at higher temperature range.

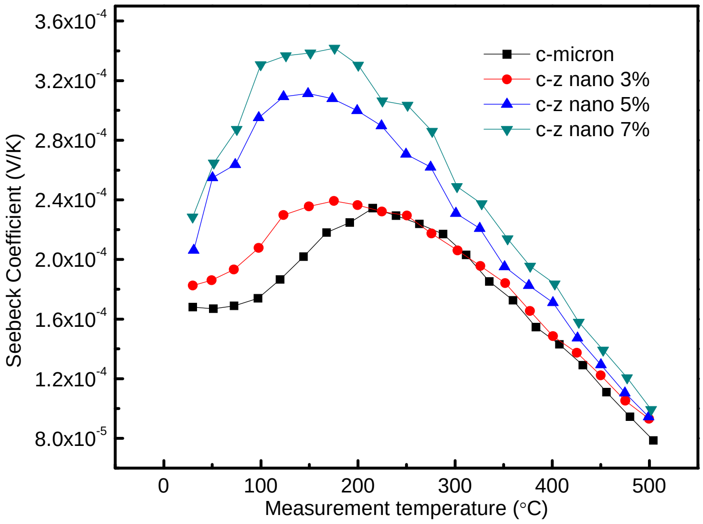

Figure 5.3-5: Temperature dependences of Seebeck coefficient with various amounts of nano-inclusions for the nanocomposite samples with ZrO_2 as nano-inclusions and undoped $CoSb_3$ as micron-matrix.

5.3.3.4 Power factor

Based on the Seebeck coefficient and electrical resistivity results, the power factor (α^2/ρ) of these samples were calculated and the results are shown in Figure 5.3-6. Even though sample c-z nano 5% and c-z nano 7% have higher power factor than that of matrix (sample c-micron) at a temperature range below 200 °C, the maximum power factors for all the nanocomposite samples are lower than that of the matrix. The nanocomposite samples have higher Seebeck coefficient than that of micron-sized matrix, however, their higher electrical resistivity caused a decrease in the power factor. The introduction of insulator as nano-inclusions is not able to improve the overall electrical properties.

For the nanocomposite samples, the power factor seems increase with nano-inclusions. However, the power factor cannot be further improved by adding more insulator nano-inclusions. Based on the work reported by Xiong's group, the high content of insulator will cause a remarkable increase in resistivity and reduce the overall power factor [92].

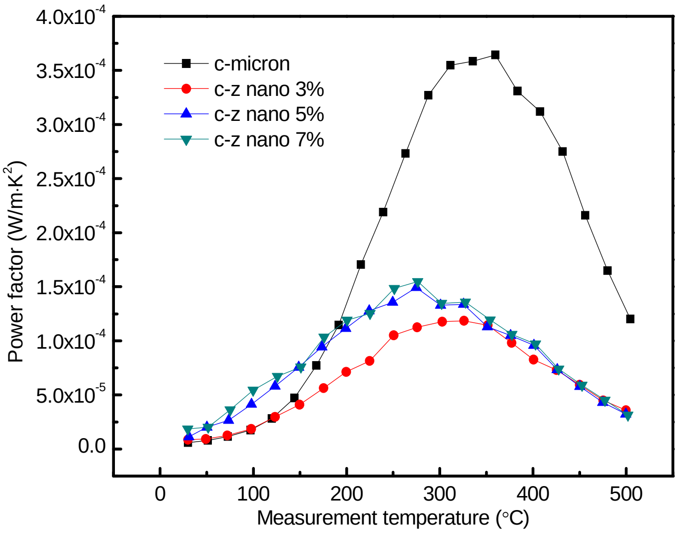

Figure 5.3-6: Temperature dependences of power factor with various amounts of nano-inclusions for the nanocomposite samples with ZrO_2 as nano-inclusions and undoped $CoSb_3$ as micron-matrix.

5.3.4 Thermal properties

Figure 5.3-7(a) shows the temperature dependence of the total thermal conductivity with various amounts of nano-inclusions. The lattice thermal conductivity κ_l for the samples was calculated by subtracting κ_c from κ ($L=2.45\times10^{-8}\ V^2K^{-2}$) and is presented in Figure 5.3-7(b). It should be noted that the effect of porosity will not be discussed here since the density of all the samples are in a very narrow range of 90% to 92% of the theoretical value, which means that the effect of porosity will be similar for these samples.

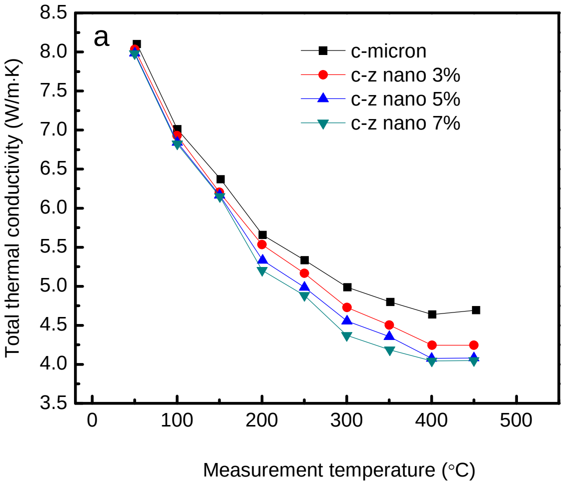

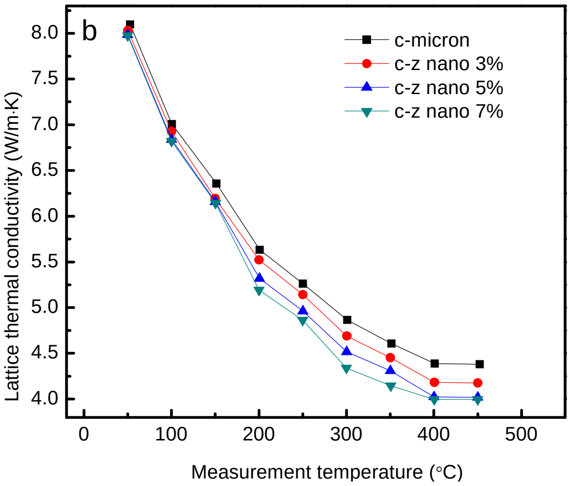

Figure 5.3-7: Temperature dependences of (a) total thermal conductivity and (b) lattice thermal conductivity with various amounts of nano-inclusions for the nanocomposite samples with ZrO_2 as nano-inclusions and undoped $CoSb_3$ as micron-matrix.

Overall, both lattice thermal conductivity and total thermal conductivity decreased with increasing contents of nano-inclusions. The relatively high density of grain boundaries of ZrO_2 nano-inclusion can scatter phonons and impede the movement of phonons, and hence reduce the lattice thermal conductivity. Meanwhile ZrO_2 is not a good thermal conductor itself (1.8~3.0 W/m·K at room temperature), and the phonon cannot select its path like electronic carriers, when it passes through ZrO_2 the thermal conductivity are reduced. However, the depression rate of total and lattice thermal conductivity of the C-Z system is not as obvious as compared to that of the C-C system and results reported by He et al [122]. The reason is located at the grain size of the ZrO_2 nano-inclusions obtained by a top-down approach which is much bigger than those in the other two systems. Here we can see that, the effect of phonon scattering by the nano-inclusion with big grain size is not as effective as that with smaller grain size.

5.3.5 Figure-of-merit ZT value

With the electrical resistivity, Seebeck coefficient and thermal conductivity results, the dimensionless figure of merit, *ZT* values for the samples were calculated and presented in Figure 5.3-8. Due to the poor electrical resistivity of the nanocomposite samples with ZrO_2 as nano-inclusions, among the nanocomposite samples, the highest *ZT* value achieved is only 0.033 at about 300 °C for the sample c-z nano 7%, which is even lower than the value of 0.047 at 450 °C for the sample c-micron without nano-inclusions. Even though the ZrO_2 nano-inclusion has improved the Seebeck coefficient and minimally reduced the thermal conductivity, its poor electrical resistivity makes the overall electrical resistivities of nancomposite samples increase and leads to the overall power factor and *ZT* value to decrease. Hence, we can reach the conclusion that insulator is not a good candidate acting as nano-inclusion in thermoelectric nanocomposites.

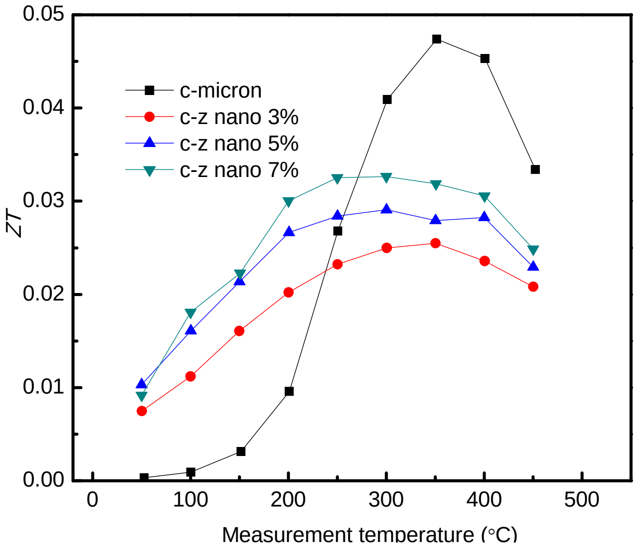

Figure 5.3-8: Temperature dependences of the dimensionless figure-of-merit *ZT* value with various amount of nano-inclusions for the nanocomposite samples with ZrO_2 as nano-inclusions and undoped $CoSb_3$ as micron-matrix.

5.4 F-C nanocomposite system

After investigating the thermoelectric properties of nanocomposites whose micron-sized matrix and nano-inclusions have very distinct carrier concentrations (for C-C nanocomposite system, the carrier concentration of nano-inclusion was much higher than that of the micron-sized matrix, and for the C-Z nancomposite system, the nano-inclusion was an insulator), in this part of the work, the nano-inclusions and micron-sized matrix with comparable carrier concentrations were studied. Filled skutterudite $La_{0.35}Ca_{0.35}Fe_{1.5}Co_{2.5}Sb_{12.03}$ prepared by solid state reaction was chosen as the micron-sized matrix and nanostructured undoped $CoSb_3$ synthesized via polyol method was chosen as the nano-inclusions. For the C-C nanocomposite system, sample c-c nano 10% possessed the best thermoelectric properties, hence, the weight percentage range for the nano-inclusions in the F-C nancomposite system was narrowed down to range from 5% to 20%.

5.4.1 Phase analysis

Figure 5.4-1 shows the XRD patterns of the hot-pressed nanocomposite pellets with various amounts of nano-inclusions. The samples are named f-c nano XX%, where XX indicates the weight percentage of nano-inclusions in the sample, f refers to the matrix which is filled skutterudite of the composition, $La_{0.35}Ca_{0.35}Fe_{1.5}Co_{2.5}Sb_{12.03}$. Sample f-micron refers to the sample without nano-inclusions added.

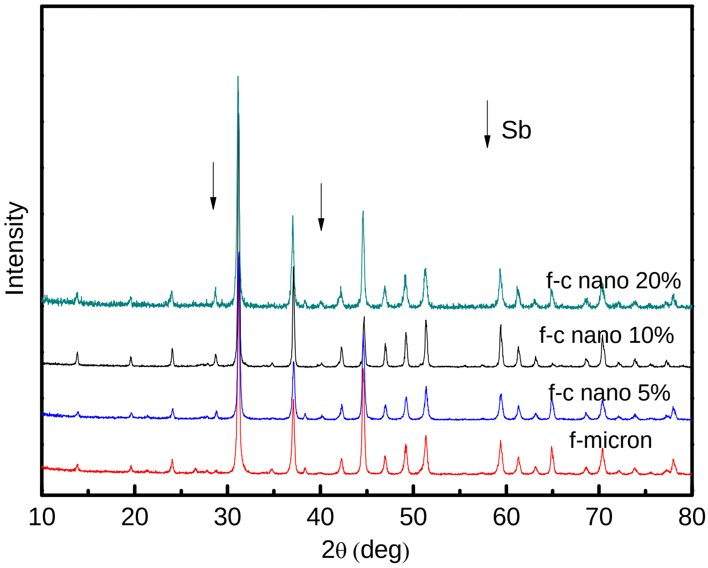

Figure 5.4-1: XRD patterns of the hot pressed nanocomposite sample pellets with undoped $CoSb_3$ as nano-inclusions and filled skutterudite $La_{0.35}Ca_{0.35}Fe_{1.5}Co_{2.5}Sb_{12.03}$ as micron-sized matrix.

All the samples are of the skutterudite phase. Additional diffraction peaks corresponding to the Sb phase were detected for the pellets that contained $CoSb_3$ nano-inclusions. The intensity of these peaks was observed to increase with increasing amount of nano-inclusions. Since excess Sb phase was not detected in the f-micron sample, the extra Sb phase must be contributed from the nano-inclusions. The same phenomenon also observed in the C-C nanocomposite system.

5.4.2 Microstructure analysis

Figure 5.4-2(a) shows a typical FESEM image of the fractured surface of the f-micron sample, indicating that the sample consists of only micron-sized grains. Figures 5.4-2(b)-(d) correspond to the FESEM images of f-c nano 5%, f-c nano 10% and f-c nano 20% samples, respectively. The microstructures of these nanocomposite samples are the similar to the ones observed for the C-C and C-Z composite systems, where most of the nano-inclusions existed as clusters residing mainly at the grain boundaries.

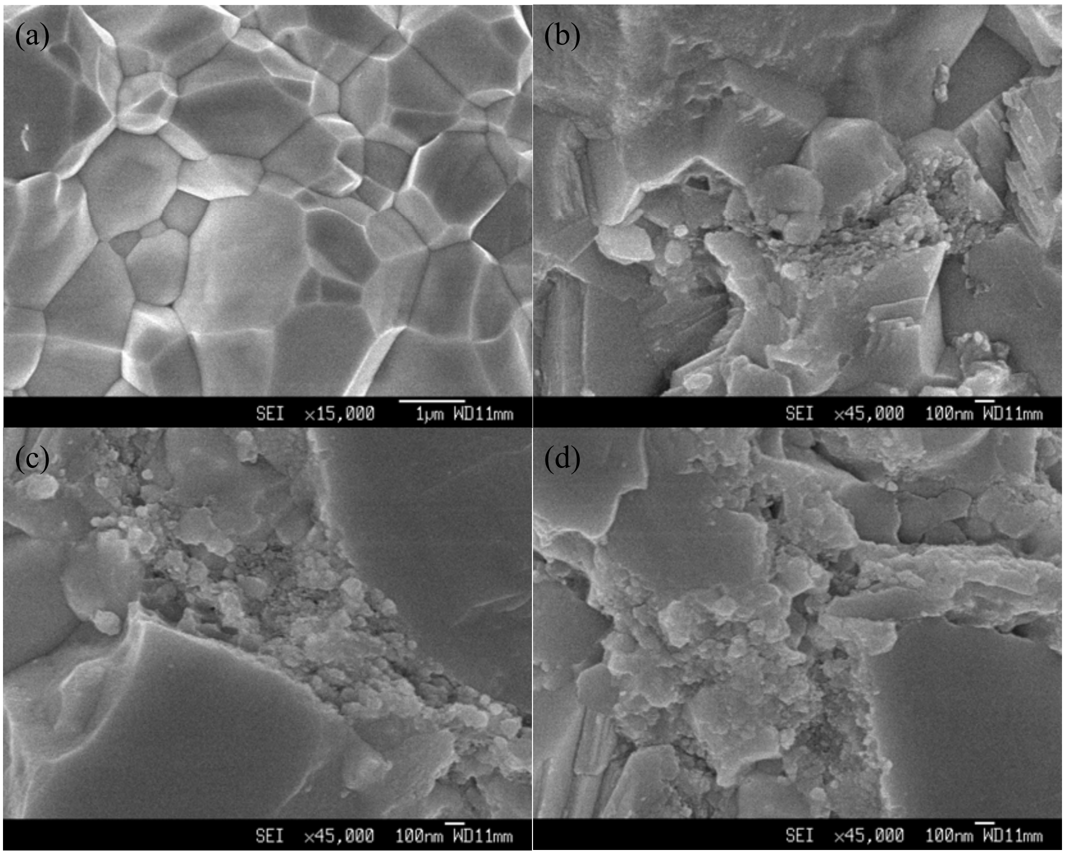

Figure 5.4-2: Typical FESEM images of fractured surfaces of f-c nanocomposite samples: (a) f-micron, (b) f-c nano 5% , (c) f-c nano 10%, and (d) f-c nano 20%.

5.4.3 Electrical properties

5.4.3.1 Carrier concentration

Figure 5.4-3 shows the carrier concentration at room temperature as a function of nano-inclusion content for the F-C nanocomposite samples. All the values are positive which indicates p-type conduction. The carrier concentration of the nano-inclusions (6.7×10^{19} cm^{-3}) is about one order lower than the micron-sized matrix (8.5×10^{20} cm^{-3}). This difference is smaller as compared to that of the C-C and C-Z nanocomposite systems. Hence, for the F-C nanocomposite samples, the carrier concentration only decreased moderately with increasing nano-inclusion content. The carrier concentration of the F-C nanocomposite samples were of the same order of magnitude as that of the micron-matrix. As compared to the C-C nanocomposite system (as shown in the inset of Figure 5.4-3), the variation in the carrier concentration was not as obvious for the same nano-inclusions content. The reason is because the difference in carrier concentration between the micron-matrix and nano-inclusions of the F-C nanocomposite system is not as distinct as that for C-C system.

From the study of these three types of nanocomposite systems (C-C, C-Z and F-C), it was clearly observed that when the nano-inclusions and the micro-sized matrix have very distinctly different carrier concentrations (e.g. C-C and C-Z nanocomposite systems), the carrier concentration of nanocomposite samples will be highly sensitive to the addition of the nano-inclusions. For example in the C-C nanocomposite system, a mere addition of 10wt% nano-inclusions caused the carrier concentration to change to a value close to that of the nano-inclusions. Similar for the C-Z system, a mere addition of 7% of the insulator nano-inclusions caused the carrier concentration to decrease significantly (by more than one order). On the other hand, for the F-C system where the micron-matrix and the nano-inclusion had comparable carrier concentrations, the carrier concentrations of the nanocomposite samples were not significantly affected.

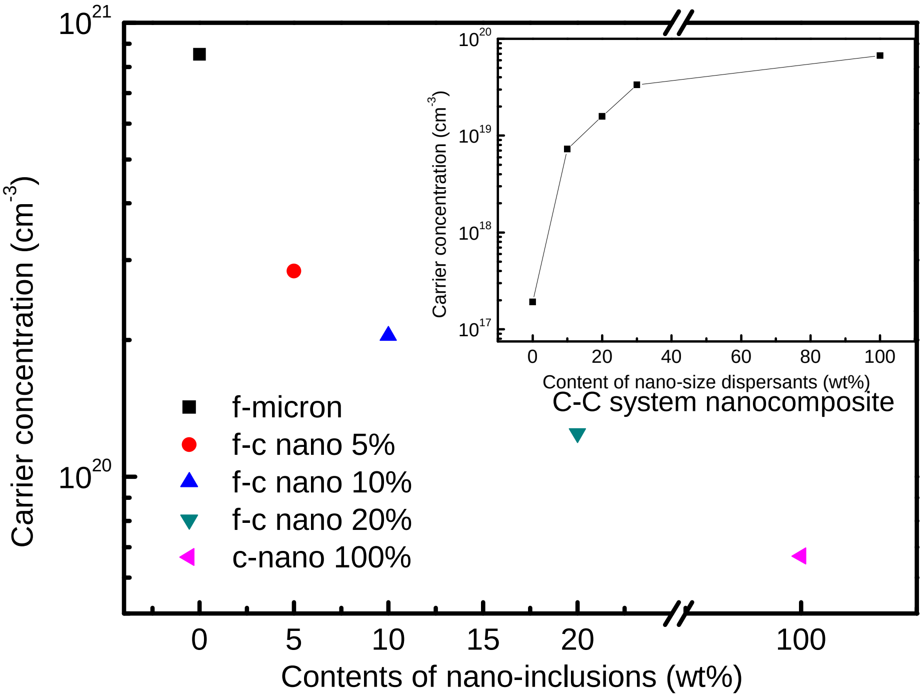

Figure 5.4-3: The dependence of the carrier concentration versus the weight percentage of nanoparticles at room temperature for the nanocomposite samples with undoped $CoSb_3$ as nano-inclusions and filled skutterudite $La_{0.35}Ca_{0.35}Fe_{1.5}Co_{2.5}Sb_{12.03}$ as micron-sized matrix. Inset is the carrier concentrations for the nanocomposite samples with undoped $CoSb_3$ both as micron-sized matrix and nano-inclusions, which is provided for comparison purposes.

5.4.3.2 Electrical resistivity

The electrical resistivities plotted as a function of temperature for all the samples with filled skutterudite as micron-sized matrix are shown in Figure 5.4-4. Electrical resistivities of the nanocomposite samples increased with increasing nano-inclusion contents. As discussed in Chapter 4, the resistivity of the c-nano 100% sample exhibits a semiconductor behaviour. The resistivity of the c-nano 100% sample was nearly one order higher than that of the f-micron sample. Also, the resistivity of the f-micron sample increased with temperature, exhibiting a metallic behaviour. Such behaviour was also observed for the nanocomposite samples (f-c nano 5%, f-c nano 10% and f-c nano 20%). It should be noted that the electrical resistivity values of these metallic behaviour samples are close to each other. This is mainly due to their approximate carrier concentrations of same order.

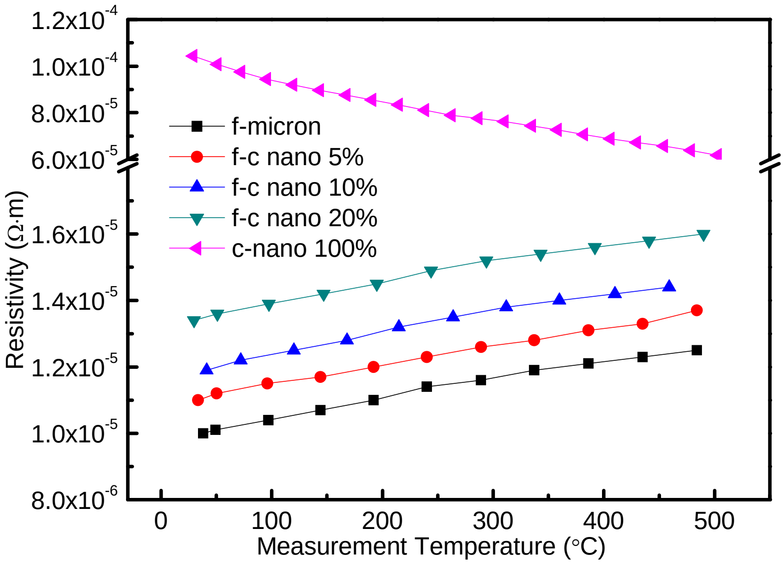

Figure 5.4-4: Temperature dependences of resistivity with various nano-inclusions for the nanocomposite samples with undoped $CoSb_3$ as nano-inclusions and filled skutterudite $La_{0.35}Ca_{0.35}Fe_{1.5}Co_{2.5}Sb_{12.03}$ as micron-sized matrix.

As compared with other nanocomposite systems, the carrier concentration of matrix (f-micron) and nanocomposite samples (f-c nano 5%, f-c nano 10% and f-c nano 20%) for F-C nanocomposite system are much higher, it is predicted that the carrier-carrier scattering may play an important role in carrier transportation. In order to verify this, the relationship between electrical resistivity and carrier concentration is studied. The proportionalities of electrical resistivity to carrier concentration, $p^{-5/3}$ (shown in Figure 5.4-5) was consistent with the carrier-carrier scattering model as proposed by Lawrence and Wilkins, indicating that carrier-carrier scattering mechanism is the dominate mechanism in carrier conduction [123].

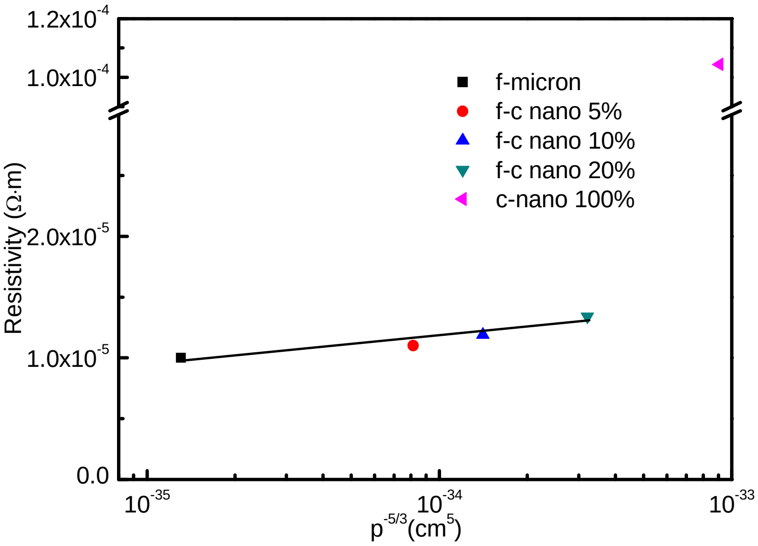

Figure 5.4-5 The proportionalities of electrical resistivity to carrier concentration $p^{-5/3}$ for samples with metallic behaviour (f-micron, f-c nano 5%, f-c nano 10% and f-c nano 20%).

5.4.3.3 Seebeck coefficient

The Seebeck coefficient plotted as a function of temperature for all the samples are shown in Figure 5.4-6. The positive values confirmed that the samples are p-type. It is observed that the Seebeck coefficient of nano-inclusion (c-nano 100%) is lower than that micron-sized matrix (f-micron). Based on the discussion of Equation (4.5) and (4.6), the Seebeck coefficient should decrease after adding second phase (nano-inclusions) with lower Seebeck coefficient. However, the results showed that the Seebeck coefficient values were not significantly affected by the addition of the nano-inclusions. This may be due to the filter effect of nano-inclusion. The nano-inclusions act as carrier filters to scatter carriers with lower energy and offset the reduction in Seebeck coefficient. And from the point of view of carrier concentration, as discussed previously, the resulting carrier concentrations for the nanocomposite samples were not altered significantly by the addition of the nano-inclusions, and the Seebeck coefficient are mainly depended on the carrier concentration in our nanocomposite systems, hence, the Seebeck coefficient values of the nanocomposite samples very much remained the same as that of micron-sized matrix.

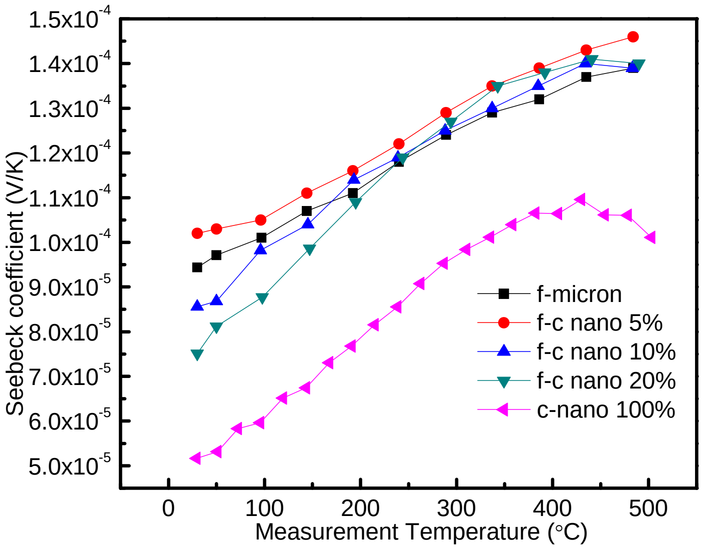

Figure 5.4-6: Temperature dependences of Seebeck coefficient with various nano-inclusions for the nanocomposite samples with undoped $CoSb_3$ as nano-inclusions and filled skutterudite $La_{0.35}Ca_{0.35}Fe_{1.5}Co_{2.5}Sb_{12.03}$ as micron-sized matrix.

5.4.3.4 Power factor

Based on the Seebeck coefficient and electrical resistivity, the power factor (α^2/ρ) of these samples were calculated and shown in Figure 5.4-7. In general, for the nanocomposite samples, the power factor decreased with increasing amount of nano-inclusions due to the increase in electrical resistivity. A maximum value of $1.56\times10^{-3}Wm^{-1}K^{-2}$ was reached at about 500 °C for the f-c nano 5% sample. Based on the power factor results of C-C and F-C nanocomposite systems, it is observed that, after introducing the nano-inclusion with poorer electrical property (smaller power factor) than that of micron-sized matrix, the power factor of nanocomposite samples are closer to that of micron-sized matrix with higher power factor rather than that of nano-inclusion. The higher power factor of micron-sized matrix is kind of maintained or even improved by nanocompositing.

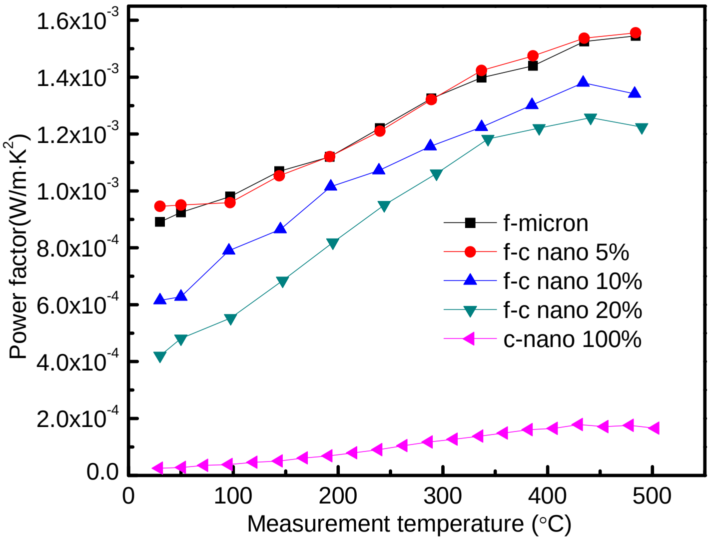

Figure 5.4-7: Temperature dependences of power factor with various nano-inclusions for the nanocomposite samples with undoped $CoSb_3$ as nano-inclusions and filled skutterudite $La_{0.35}Ca_{0.35}Fe_{1.5}Co_{2.5}Sb_{12.03}$ as micron-sized matrix.

5.4.4 Thermal properties

Figure 5.4-8 shows the total and lattice thermal conductivity for all the samples as a function of temperature. It should be noted that the effect of porosity will not be considered here since the density of all the samples were in the narrow range of 88% to 92%. As discussed previously in Section 5.2, the effect of porosity on the trend of the resulting thermal conductivity is minimal.

Both the total and lattice thermal conductivity in this F-C nanocomposite system decreased with increasing amount of nano-inclusions within the measured temperature range. This is consistent with the C-C and C-Z composite systems, where the increased phonon scattering induced by the higher density of grain boundaries introduced by the nano-inclusions. Based on the results obtained for the C-C, C-Z and F-C systems, it can definitely conclude that the nanocomposite is an effective way to reduce the lattice and total thermal conductivity by introducing grain boundaries which scatter more phonons in its corresponding wavelength and reduce the mean-free-path of the phonons.

When compared to the micron-sized undoped $CoSb_3$ (c-micron) sample, the Ca-La filled skutterudite (f-micron) sample has a much lower total and lattice thermal conductivity. The lower total thermal conductivity in the f-mircon sample is mainly contributed from the reduced lattice thermal conductivity rather than the carrier thermal conductivity, since sample f-micron possessed lower electrical resistivity than the c-micron sample. The reduction in the lattice thermal conductivity is contributed by the filling of the La and Ca atoms into the voids of the skutterudite crystal lattice. As discussed in the literature review section, skutterudite possesses an open structure in which foreign filler atoms can fill into the voids of the skutterudite crystal lattice. These filler atoms can "rattle" in the over-sized void to scatter phonons. Yang *et al.* [124] calculated the resonant frequencies of alkaline-earth filler, and determined that Ca and La have a resonant frequency of about 90 cm^{-1} and 70 cm^{-1} respectively. These two distinct domains of resonant frequencies are believed to scatter a broader spectrum of heat-carrying phonons. As a result, the Ca-La double filling provides remarkable reduction in lattice thermal conductivity as compared to un-filled $CoSb_3$ (c-micron). Meanwhile, for sample f-micron, substitution of Co by Fe in the lattice introduced additional point defects to scatter phonons and further reduce the lattice thermal conductivity. Finally, in the F-C nanocomposite samples, there are three means of reducing the thermal conductivity: filling, doping and nano-inclusions.

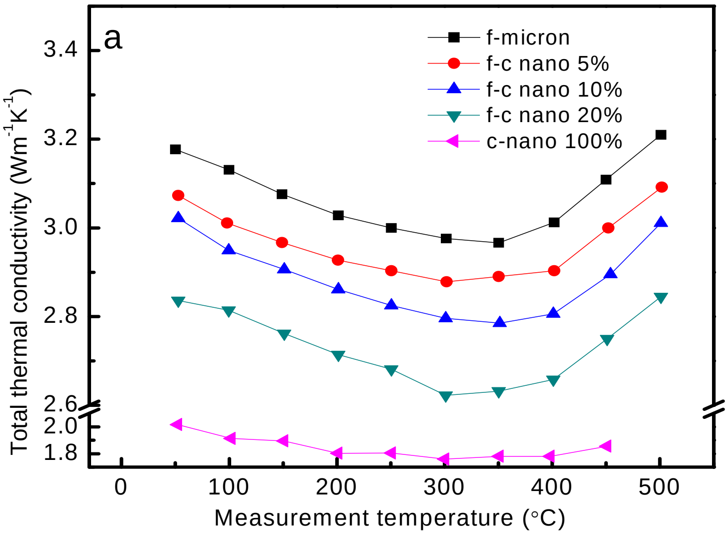

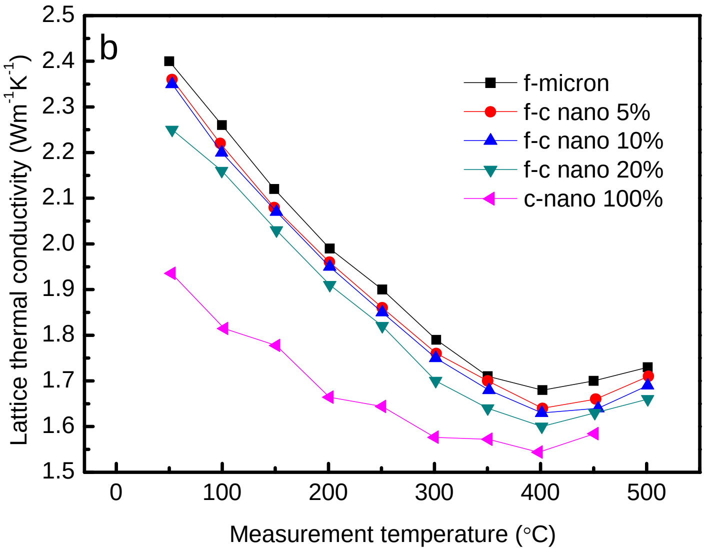

Figure 5.4-8: Temperature dependences of experimental total thermal conductivity (a), experimental lattice thermal conductivity (b) for the nanocomposite samples with various amounts of nano-inclusions with undoped $CoSb_3$ as nano-inclusions and filled skutterudite $La_{0.35}Ca_{0.35}Fe_{1.5}Co_{2.5}Sb_{12.03}$ as micron-sized matrix.

6.4.5 Figure-of-merit *ZT* value

With the electrical resistivity, Seebeck coefficient and thermal conductivity results, the dimensionless figure of merit, *ZT* values for the samples were calculated and presented in Figure 5.4-9. The highest *ZT* value of 0.39 was attained at about 500 °C for f-c nano 5%. As compared to the bulk sample, the value has increased by 6%. This improvement is comparable with Mi's and Alboni's results. In their work, samples with 10wt% (for Mi's work) and 5wt% (for Alboni's work) of $CoSb_3$ nano-inclusions possessed the best *ZT* value with an improvement of less than 10% comparing with the micron-sized matrix of Yb-filled and La-filled skutterudite [125,126]. Comparing with the improvement of *ZT* value for C-C improvement, the increase in *ZT* for F-C system is not obvious. This is because, for the thermal conductivity of the filled skutterudite-based nanocomposites, whose thermal conductivity of matrix is already relatively low due to the rattling of the filler atoms, the reduction in the absolute value of total thermal conductivity (from 3.2 $Wm^{-1}K^{-1}$ of bulk to 2.8 $Wm^{-1}K^{-1}$ of nano 20% for F-C system) through this nanocomposite approach is not as significant as our previous work in which the matrix is pure $CoSb_3$ (from 8.1 $Wm^{-1}K^{-1}$ to 7.1 $Wm^{-1}K^{-1}$ of nano 20% for C-C system). Furthermore, the electrical properties of filled skutterudites are already very excellent due to the filling atoms, and the improvement by adding nano-inclusion is not so remarkable as that for unfilled skutterudites.

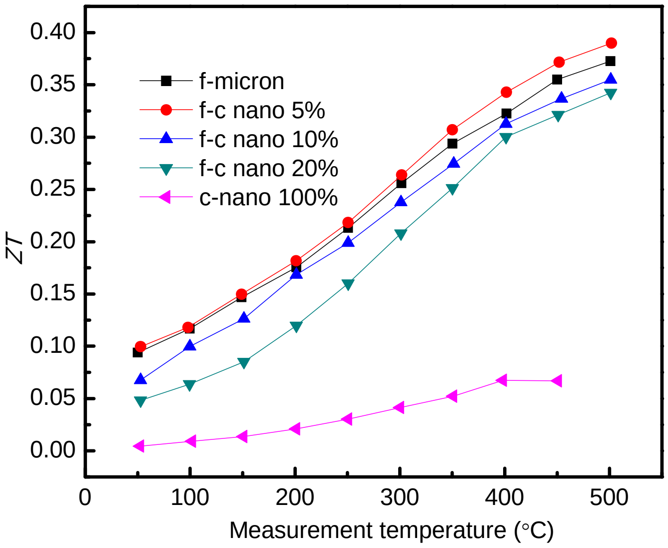

Figure 5.4-9: Temperature dependences of figure-of-merit *ZT* value with various nano-inclusions for the nanocomposite samples with undoped $CoSb_3$ as nano-inclusions and filled skutterudite $La_{0.35}Ca_{0.35}Fe_{1.5}Co_{2.5}Sb_{12.03}$ as micron-sized matrix.

5.5 Comparison and conclusions

5.5.1 Comparison—electrical properties

The dependences of carrier concentration and electrical resistivity on weight percentage of nano-inclusions of three types of nanocomposites at room temperature are shown in Figure 5.5-1 for comparison. It is clearly seen that the carrier concentration (shown in Figure 5.5-1(a)) of the nanocomposite increased when the carrier concentration of the nano-inclusion is larger than that of matrix and decreased when the nano-inclusion is of lower carrier concentration. The electrical resistivity (shown in Figure 5.5-1(b)) decreases with content of nano-inclusion of lower electrical resistivity and increases with content of nano-inclusion of higher electrical resistivity. When the micron-sized matrix and nano-inclusion have very distinct carrier concentrations (C-C and C-Z nanocomposite systems) and electrical resistivity, the variation rate of carrier concentration and electrical resistivity versus the weight percentage of nano-inclusion are bigger than that of nanocomposite system whose micron-sized matrix and nano-inclusion have comparable carrier concentration or electrical resistivity (F-C nanocomposite system). The higher carrier concentration of nano-inclusion will increase the carrier concentration and meanwhile decrease the overall electrical resistivity of nanocomposite samples. Among these three types of nanocomposite systems, the C-C nanocomposite system whose carrier concentration (electrical resistivity) of nano-inclusion is much higher (lower) than that of micron-sized matrix possesses the most improvement in reducing the electrical resistivity.

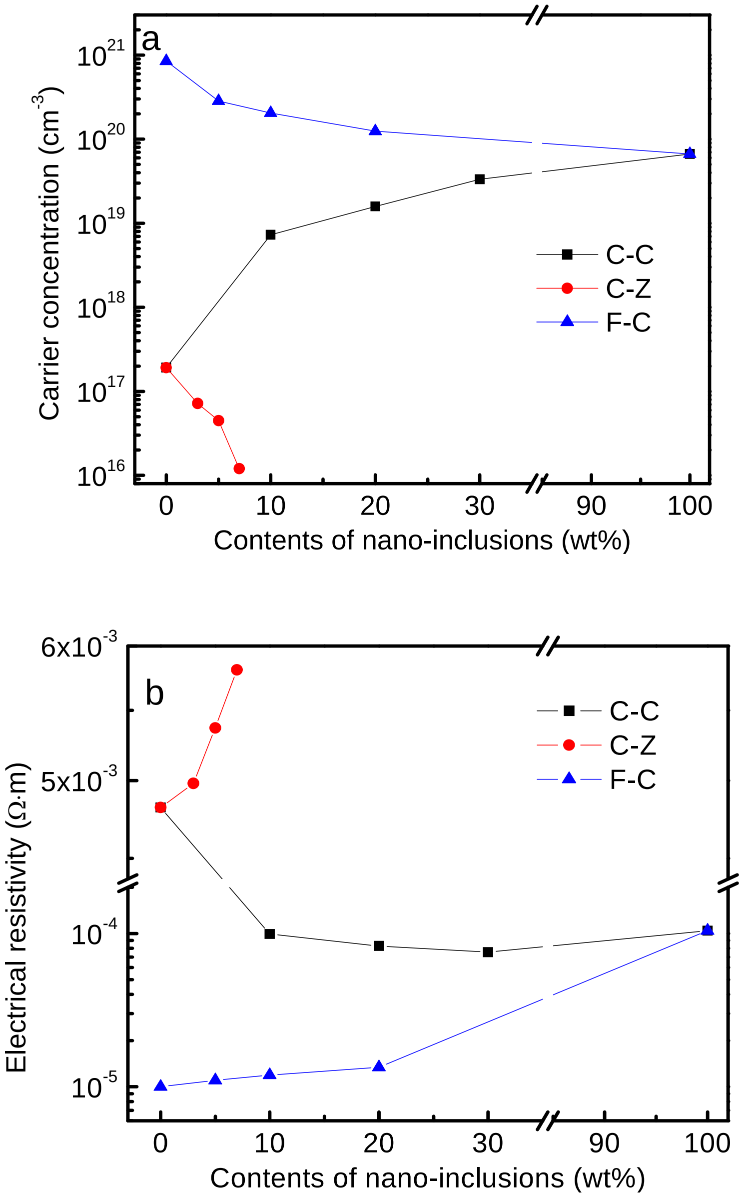

Figure 5.5-1: The dependence of carrier concentration (a) and electrical resistivity (b) versus the weight percentage of nano-inclusions at room temperature for C-C, C-Z and F-C nanocomposite systems.

However, the nanocomposite effect on the Seebeck coefficient is more complicated. Since the filter effect always does good to Seebeck coefficient, here, we mainly consider the effect of carrier concentration on Seebeck coefficient. The dependence of Seebeck coefficient on weight percentage of nano-inclusions for each type of nanocomposite system at room temperature are shown in Figure 5.5-2 and the carrier concentration is also displayed for comparison. Combining the relationship between carrier concentration and weight percentage of nano-inclusion discussed before, for the C-C and C-Z nanocomposite systems whose micron-sized matrix and nano-inclusion have distinct carrier concentration, at room temperature, the variation in Seebeck coefficient are mainly attributed by carrier concentration and has the opposite trend to the carrier concentration. However, for the F-C nanocomposite system, due to the comparable carrier concentration of micron-sized matrix and nano-inclusion, the Seebeck coefficient values of the nanocomposite samples change moderately and without remarkable trend.

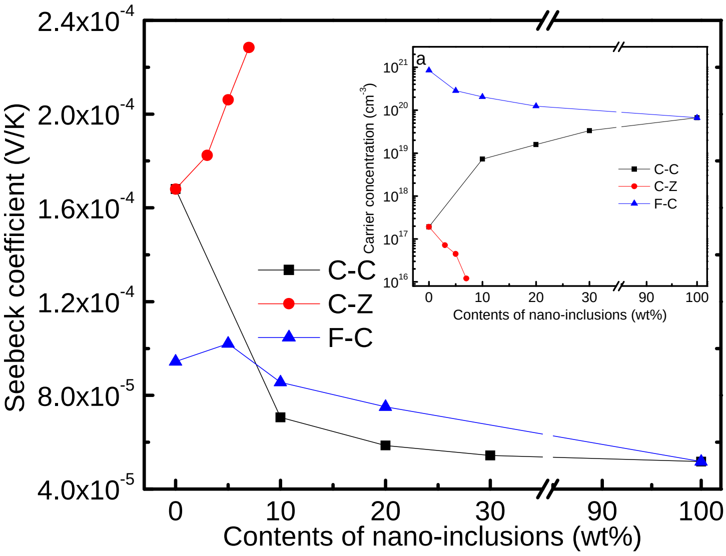

Figure 5.5-2: The dependence of Seebeck coefficient versus the weight percentage of nano-inclusions at room temperature for C-C, C-Z and F-C nanocomposite systems. Inset is the carrier concentrations for these three systems, which is provided for comparison purposes.

The dependences of overall power factor on the weight percentage of nano-inclusions of three types of nanocomposites at room temperature are shown in Figure 5.5-3 for comparison. From the point of view of power factor, comparing with the micron-sized matrix, the most improvement happens in the nanocomposite samples whose nano-inclusion possesses much higher carrier concentration (much lower electrical resistivity) than that of micron-sized matrix i.e. sample c-c nano 10% in C-C nanocomposite system. Hence, the nano-inclusion with much higher carrier than that of micron-sized matrix is the best candidate to improve the overall electrical property (power factor) of nanocomposite samples.

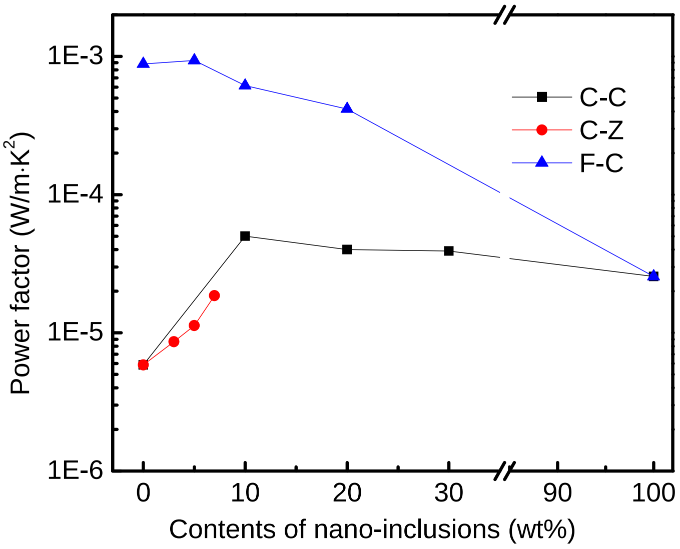

Figure 5.5-3: The dependence of power factor versus the weight percentage of nano-inclusions at room temperature for C-C, C-Z and F-C nanocomposite systems.

5.5.2 Comparison—thermal properties

For thermal properties, nanocomposite is an effective method to reduce both the lattice and total thermal conductivity due to the introduction of nano-inclusions which have high density of grain boundaries to scatter phonons more effectively. Both total thermal conductivity and lattice thermal conductivity decrease with increasing amount of nano-inclusions which are in a good agreement with the theoretical predictions.

After studying the thermal conductivity of nanocomposites, we tried to find a model or equation to predict the effective thermal conductivity for the nanocomposites.

Since the exact total thermal conductivity of ZrO_2 nano-particles used in session 5.3 is not clear, the quantitative analysis on total thermal conductivity of C-Z nanocomposite system will not be studied here. In order to predict the effective thermal conductivity of nanocomposites, several models were applied. Based on the results of C-C and F-C nanocomposite system, the effective thermal conductivity of nanocomposites can be best estimated by the following equation [127,128]:

$$\kappa_E = \kappa_M \left[\frac{\kappa_I + (n-1)\kappa_M - (n-1)V_I(\kappa_M - \kappa_I)}{\kappa_I + (n-1)\kappa_M + V_I(\kappa_M - \kappa_I)} \right] \tag{5.6}$$

here, κ_E is the effective thermal conductivity of the mixed composite, κ_M is the thermal conductivity of the micron-sized matrix (e.g. κ_M=3.18 W/m·K for sample f-micron at 50 °C), κ_I is the thermal conductivity of the nano-inclusion (e.g. κ_I=2.02 W/m·K for sample c-nano 100% at 50 °C), V_I is the inclusion particle volume fraction (since the matrix and the nano-inclusions are of the same phase, the volume percentage is equal to the weight percentage) and n is the empirical shape factor (in this work, the nano-inclusion are assumed to be spheres, therefore n=3). Figure 5.5-4(a) and (b) show the comparison between the experimental results and the data calculated using equation (5.6) for the F-C and C-C system, respectively. Overall, the agreement is satisfactory which indicates that Equation (5.6) can predict the final κ_E of the nanocomposite samples. From Equation (5.6) and experimental results for nanocomposites with both filled skutterudite and pure $CoSb_3$ as matrix, one can see that the final κ_E of the mixtures falls between the value of κ_M and κ_I. It is also noted that according to Equation (5.6), κ_E decreases with the increasing value of (κ_M-κ_I) with the same inclusion particle volume fraction.

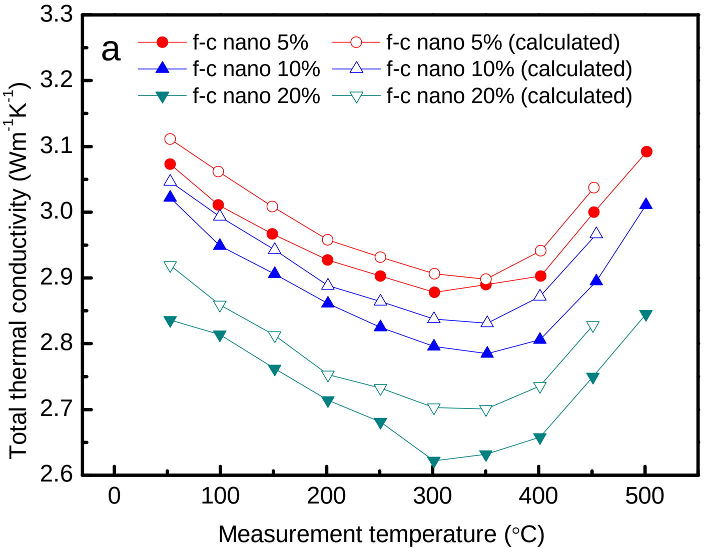

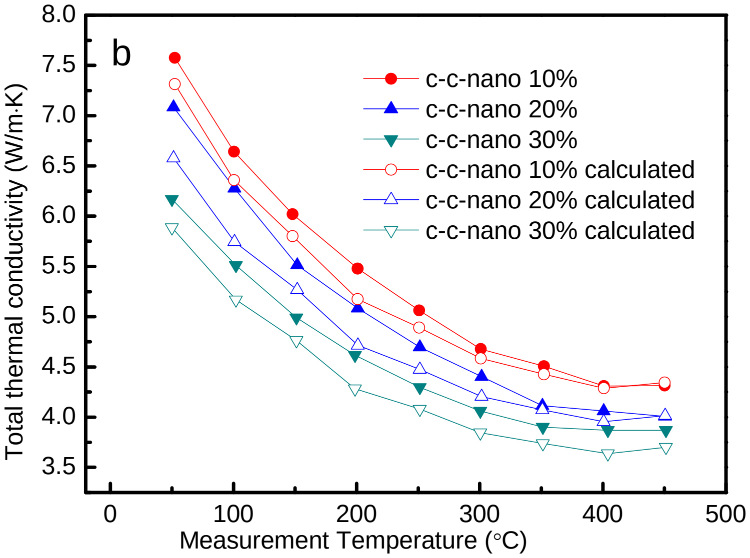

Figure 5.5-4: Comparison of experimental and calculated total thermal conductivity for the nanocomposite samples with various amounts of nano-inclusions with (a) undoped $CoSb_3$ as nano-inclusions and filled skutterudite $La_{0.35}Ca_{0.35}Fe_{1.5}Co_{2.5}Sb_{12.03}$ as micron-sized matrix and (b) with undoped $CoSb_3$ as both nano-inclusions and micron-sized matrix.

It should be noted that for the F-C nanocomposite system, the calculated data are higher than the experimental results, while for the C-C nanocomposite system, the calculated data are smaller than that of experimental results. From Figure 5.5-5(a) the deviations between the two values increased with increasing nano-inclusion contents. This may be due to the effect of porosity. The densities of all the samples are in the range of 88% to 92% of the theoretical value and decreases with increasing nano-inclusion content since the nano phase are more difficult to densify. From our previous calculation, when the densities of the samples fall within a narrow range, the effect of porosity on the thermal conductivity is not obvious. Conversely, the calculated data for C-C nanocomposite system is smaller than that of measured results. Equation (5.6) is applied on the insulator, and electrical thermal conductivity contributed by carriers which is equal to $\kappa_e=LT/(pe\mu)$ is not considered. For C-C nanocomposite system, after introducing nano-inclusions, the electrical thermal conductivity has greatly increased due to the great increase in carrier concentration. Since the thermal conductivity is mostly contributed by lattice thermal conductivity, the deviation caused by the carriers is in the acceptable range. The effective of porosity for C-C nanocomposite system is not obvious, because this effect is already offset by that of carrier concentration.

Therefore, based on this work, we can see that Equation (5.6) can be widely used to calculate the effective thermal conductivity of nanocomposites. The deviation between the calculated and experimental results is reasonable. It provides a general rule to choose the nano-inclusions for the nanocomposite method to further reduce the thermal conductivity in thermoelectric materials.

5.6 Effect of grain size of nano-inclusions on the thermoelectric properties of nanocomposites

The size, morphology and distribution of the nano-phase can indeed play very important roles on the final properties of thermoelectric nanocomposite system. However, in this work, $CoSb_3$ skutterudite is a body-centred cubic crystal structure, and there is no preferred orientation during its crystal growth, which means that it is difficult to obtain 1D nanostructures such as nanowires or nanotubes via wet chemical route. Therefore, the study on the effects of morphology was not investigated in this work. Most nanocomposites with nano-inclusion evenly dispersed in the matrix were obtained in film or layer-structured materials obtained by molecular beam epitaxy system, plasma laser deposition and so on. Due to the experimental limitation and design, the precise control of the distribution of the nano-phase in our as-synthesized nanocomposites could not be achieved. Here, we will only study the size effect of the nano-inclusions on the properties of thermoelectric nanocomposite.

The nano-particles of p-type undoped $CoSb_3$ were synthesized via polyol method and the detailed experimental procedures were presented in Chapter 3. In the nanocomposite system with pure $CoSb_3$ acting both as nano-inclusion and micron-sized matrix, the effect of carrier concentration difference between nano-inclusion and micron-sized matrix will overweight that of grain-size on the final thermoelectric properties of nanocomposites. Hence, the La- and Ca- filled skutterudite $La_{0.35}Ca_{0.35}Fe_{1.5}Co_{2.5}Sb_{12.03}$ with comparable carrier concentration to that of nano-inclusions is chosen as the matrix of this nanocomposite system to limit the effects of electrical properties difference between the nano-inclusions and matrix on the final thermoelectric properties of the nanocomposites. Nanocomposite sample with 5wt% of nano-inclusion were prepared since sample f-c nano 5%'s best thermoelectrical properties among the F-C nanocomposite system. Samples are named as f-c xx, where f-c means that the micron-sized matrix is filled-skutterudite and the nano-inclusion is $CoSb_3$, and xx indicates the size (nm) of the nano-inclusions. The hot press condition for sample f-c 50 was 500 °C, 2 h, and 100 MPa, while ahot press condition of 500 °C, 4 h, and 100 MPa was applied for sample f-c 120 to increase the grain size of the nano-inclusions. The FESEM image (Figure 5.6-1 (a)) shows that the average grain size of the nano-inclusions in sample f-c 50 is around 50 nm. From FESEM observation (Figure 5.6-1 (b)), the average grain size of the nano-inclusions in sample f-c 120 with longer dwelling time of 4 h is around 120 nm, which is much larger than that in sample f-c 50.

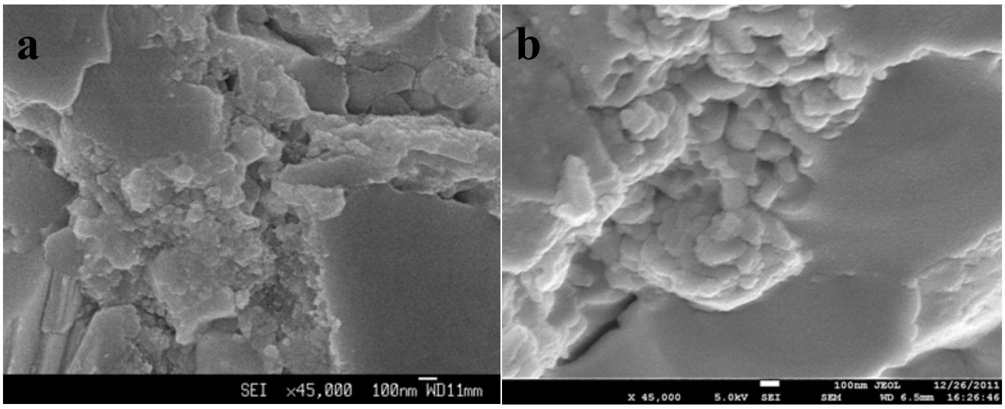

Figure 5.6-1: Typical FESEM images of the fractured surfaces of (a) f-c 50 and (b) f-c 120.

Figure 5.6-2 shows the electrical resistivity of two nanocomposite samples whose nano-inclusions are of different grain sizes. Both samples show a metallic behavior, i.e. the electrical resistivities increases with increasing temperature, which is in agreement with that of the micron-sized matrix (f-micron, shown in Figure 5.6-2). The samples with smaller grain size of nano-inclusions possesses a higher resistivity. According to MS theory [129], these nano-inclusions with smaller size lead to the presense of more grain boundaries, which means that the carriers are scattered by these grain boundaries and hence a reduction in their mean free path of carriers as well as increase in electrical resistivity.

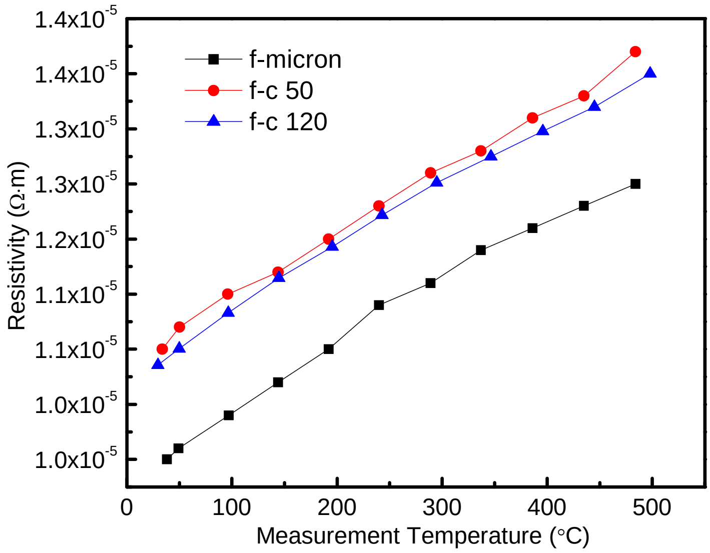

Figure 5.6-2: Temperature dependences of resistivity for the micron-sized matrix and the nanocomposite samples with different grain size of nano-inclusions.

Figure 5.6-3 shows the Seebeck cofficient of these two nanocomposite samples whose nano-inclusions are of different grain sizes as well as the micron-sized matrix. Here, the effect of carrier concentration on the Seebeck coefficient is not considered, since the micron-sized matrix and nano-inclusion have comparable carrier concentration. From the experimental results, the Seebeck coefficient values of sample f-micron and f-c 120 are very similar but lower than that of f-c 50. This phenomenon is due to the filter effects of grain boundaries. When the length of grains is small (i.e. the density of grain boundaries is high), the possibility of carriers with relatively high energy passing through the potential barrier of these high density grain boundaries are much higher that of carriers with relatively low energy. This leads to the increase in Seebeck coefficient as the length of grains decreases.

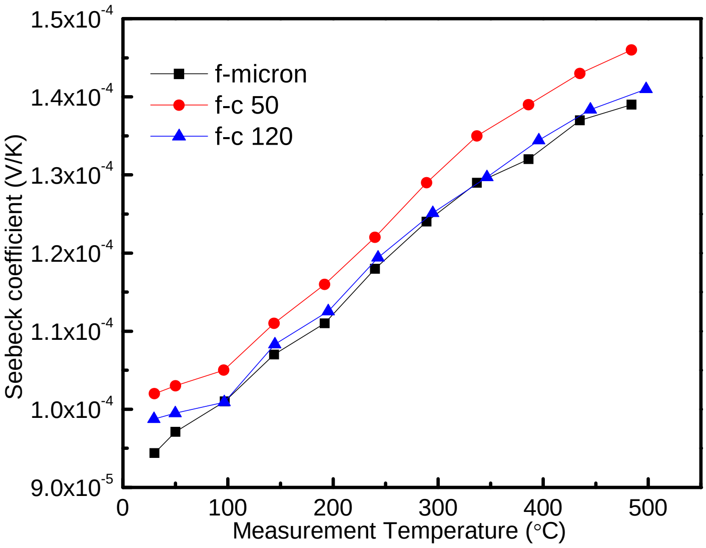

Figure 6.5-3: Temperature dependences of Seebeck coefficient for the micron-sized matrix and the nanocomposite samples with different grain size of nano-inclusions.

Based on the Seebeck coefficient and electrical resistivity results, the power factor (α^2/ρ) of these samples were calculated (see Figure 5.6-4). Comparing with the micron-sized matrix, the power factor does not change too much after introducing 5wt% of nano-inclusion with a size of 50 nm. The power factors of sample f-c 50 are higher than that of f-c 120 due to its relatively high Seebeck coefficent. Among all these three samples, sample f-c 50 possessed the best electrical property with a maximum power factor of 1.56×10^{-3} $Wm^{-1}K^{-2}$ at about 500 °C.

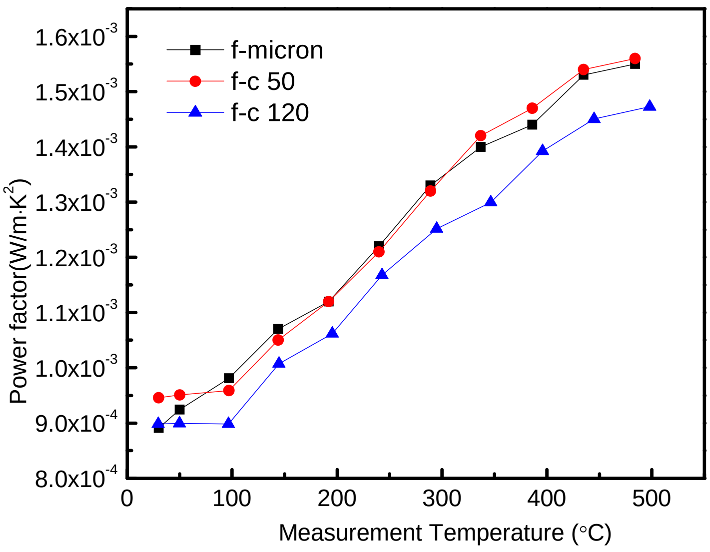

Figure 5.6-4: Temperature dependences of power factor for the micron-sized matirx and the nanocomposite samples with different grain size of nano-inclusions.

Figure 5.6-5 (a) shows the temperature dependences of the total thermal conductivity of these two samples with different nano-inclusion sizes. The lattice thermal conductivity κ_l for the samples obtained by subtracting κ_c from κ was also determined ($\kappa_c = \frac{LT}{\rho}$ and $L=2.45\times 10^{-8}\ V^2K^{-1}$), and the results are shown in Figure 5.6-5 (b). As expected, both total and lattice thermal conductivities decrease with decreasing grain size of nano-inclusions, which is a result of the increased density of grain boundaries to scatter more phonons. Essentially, the phonons are scattered by the grain boundaries. These grain boundaries scatter and impede the movement of phonons. The mean free path of phonons is reduced by these introduced grain boundaries and lead to further reduction in both lattice and total thermal conductivity. For the same weight percentage of nano-inclusions in the nanocomposite, the nano-inclusions with smaller grain size introduce more grain boundaries and lead to more reduction in the lattice and total thermal conductivity.

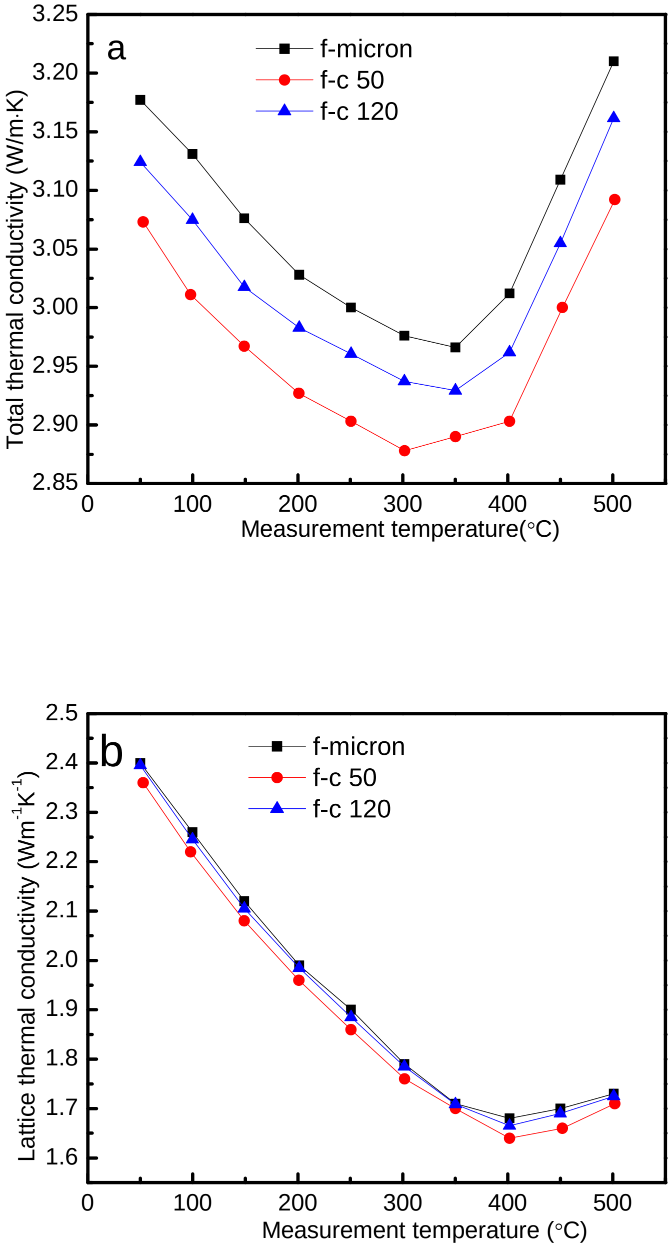

Figure 5.6-5: Temperature dependences of total thermal conductivity (a) and lattice thermal conductivity (b) for the micron-sized matrix and the nanocomposite samples with different grain size of nano-inclusions.

With the electrical resistivity, Seebeck coefficient and thermal conductivity results, the dimensionless figure of merit, *ZT* values for these two nanocomposite samples with different grain size of nano-inclusions are calculated and presented in Figure 5.6-6. Even though these there samples have very similar value within the measurement temperature range, sample f-c 50 possesses the best *ZT* value of 0.4 at around 500 °C. The increase in *ZT* value of sample f-c 50 benefits from the increase in Seebeck coefficient as well as the reduction in both the total and lattice thermal conductivity due to the smaller nano-inclusions.

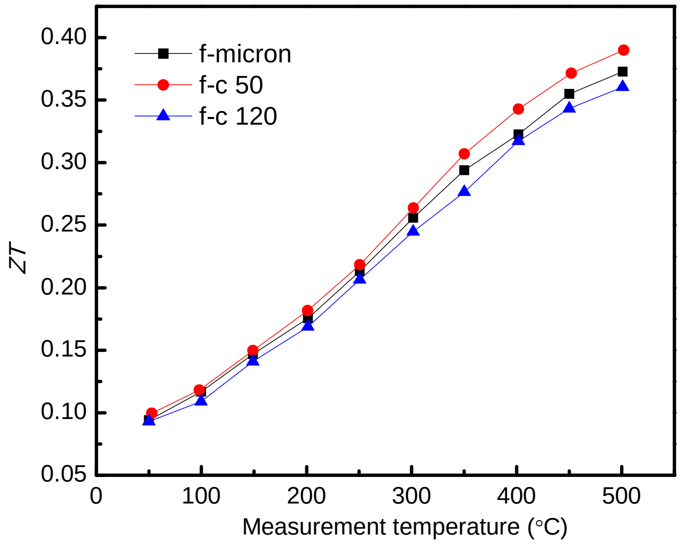

Figure 5.6-6: Temperature dependences of figure-of-merit *ZT* value for the micron-sized matrix and the nanocomposite samples with different grain size of nano-inclusions.

Based on this study, it can be concluded that with the same percentage of nano-inclusions, the nano-inclusions with a smaller size gives a better performance on the final thermoelectric properties of nanocomposites.

5.7 Conclusions

In this chapter, 3 types of p-type nanocomposites have been prepared.

1. For the all these 3 types of nanocomposites, both total thermal conductivity and lattice thermal conductivity decrease with increasing amount of nano-inclusions which are in a good agreement with the theoretical predictions. Based on the experimental

results from both session 5.2 and 5.4, a general rule for the choice of the nano-inclusions is provided. In order to reduce the effective thermal conductivity of the mixed nanocomposite, the thermal conductivity of the nano-inclusions must be lower than that of the matrix, and preferably much lower than the matrix phase.

2. The carrier concentration was found to be very sensitive to the amount of nano-inclusion, when the matrix and nano-inclusion have distinctly different carrier concentration. When the carrier concentration of nano-inclusion is much higher (lower) than that of micron-sized matrix, the carrier concentrations of nanocomposite increase (decrease) greatly after introducing nano-inclusions. When the micron-sized matrix and nano-inclusion have comparable carrier concentrations, the carrier concentrations of nanocomposite samples change moderately.

3. For the electrical resistivity, combining the results from session 5.2, 5.3 and 5.4, the overall electrical resistivity of the nanocomposite increased when the electrical resistivity of the nano-inclusion is larger than the matrix and decreased when the nano-inclusions is of lower electrical resistivity which shows the same trend as that of carrier concentration.

4. Carrier concentration is the dominating effect on the final Seebeck coefficient, i.e. the Seebeck coefficients decrease with the increasing carrier concentration. Comparing with the nanocomposite samples with undoped $CoSb_3$ as the micron-sized matrix, the nano-inclusions in F-C nanocomposite system have insignificant effect on the Seebeck coefficient of the composite samples with filled skutterudite as matrix due to unapparent variation in carrier concentration. Besides carrier concentration, the filter effects introduced by the nano-inclusion always have a good effect on Seebeck coefficient.

5. For the overall electrical properties evaluated by the power factor, the cases are more complicated. When the carrier concentration (resistivity) of nano-inclusion is much lower (higher) than that of the micron-sized matrix (e.g. in the C-Z nanocomposite system), the nano-inclusion has a negative effect on the power factor of the nanocomposite samples. When the nano-inclusion and micron-sized matrix have comparable carrier concentration or resistivity (e.g. in the F-C nanocomposite system), the improvement in the power factor is not significant. However, when the carrier concentration (resistivity) of nano-inclusion is much higher (lower) than that of micron-sized matrix (e.g. in the C-C nanocomposite system), the power factor of the nanocomposite increased significantly as compared to that of the micron-sized matrix. Hence, in order to improve the electrical properties, the nano-inclusion must possess much higher carrier concentration or much lower resistivity than that of the micron-sized matrix.

6. For the overall thermoelectric properties (*ZT* value), due to the great improvement on the electrical properties of the nanocomposite samples whose carrier concentration (resistivity) is much higher (lower) than that of micron-sized matrix as well as the reduction in thermal conductivity, the highest *ZT* value of the C-C nancomposite system nearly doubled that of the matrix. Here, we can conclude that nanostructures with much higher (lower) carrier concentration (resistivity) and much lower thermal conductivity than that of micron-sized matrix are the most suitable for use as nano-inclusions. However, the amount of nano-inclusion cannot be decided qualitatively, it depends on the both electrical and thermal properties difference between nano-inclusion and micron-sized matrix.

7. For the nanocomposites with the same percentage of same type of nano-inclusions, the nano-inclusions with a smaller size gives a better performance on the final thermoelectric properties of nanocomposites.

Chapter 6

Preparation and Characterization of n-type $CoSb_3$-based nanocomposites

6.1 Introduction

A TE device needs both p- and n-type materials to function. Having attained an improved figure-of-merit *ZT* value for p-type nanocomposites in Chapter 5, we will improve the thermoelectric properties of the corresponding n-type material. In this chapter, we focus mainly on the preparation and characterization of the thermoelectric properties of n-type nanocomposites.

Based on the result of Mi's work, n-type Te-doped $CoSb_3$ ($Te_{0.03}Co_{0.97}Sb_3$) prepared through traditional solid state reaction was chosen as micron-sized matrix and mixed with various amount of nano-inclusions [77]. According to the conclusion of p-type nanocomposites (Chapter 5) that nanostructure materials with higher carrier concentration or low resistivity than that of matrix is suitable to use as nano-inclusions, nanostructured $Ni_{1.25}Co_{6.75}Sb_{24}$ synthesized in Chapter 4 are chosen as the nano-inclusion due to its highest carrier concentration, lowest resistivity and highest *ZT* value among the Ni-doped nanostructures. This kind of nanocomposite is so called T-N system for short. It is expected that the nano-inclusion with very low resistivity may have a positive effect on the electrical resistivity and improve the overall thermoelectric property of the final nanocomposite samples. Since for the p-type nanocomposite C-C and F-C system, the nanocomposite samples which possess the best thermoelectric properties are the 10wt% and 5wt% of nano-inclusions respectively, the weight percentage of nano-inclusion was varied from 5% to 15%, in interval of fives for this work.

6.2 T-N nanocomposite system

6.2.1 Phase analysis

Figure 6.2-1 shows the XRD pattern of the hot-pressed pellets obtained from the n-type nanocomposites with various amount of nano-inclusions with $Ni_{1.25}Co_{6.75}Sb_{24}$ as the nano-inclusions and $Te_{0.03}Co_{0.97}Sb_3$ as the micron-sized matrix. The samples are named t-n nano XX%, where XX indicates the weight percentage of nano-inclusions in the sample， t-n means that the micron-sized matrix is Te-doped $CoSb_3$ and nano-inclusion is Ni-doped $CoSb_3$. The sample t-micron means Te-doped $CoSb_3$ with no extra nano-inclusions added. The XRD results indicated that sample t-micron and t-n 5% are in the pure skutterudite phase. The trace peaks attributed to Sb only appears in the sample t-n nano 10% and t-n nano 15% with relative high content of nano-inclusion. This is because the amount of Sb introduced by nano-inclusion for sample t-n 5% is too little for the XRD to detect.

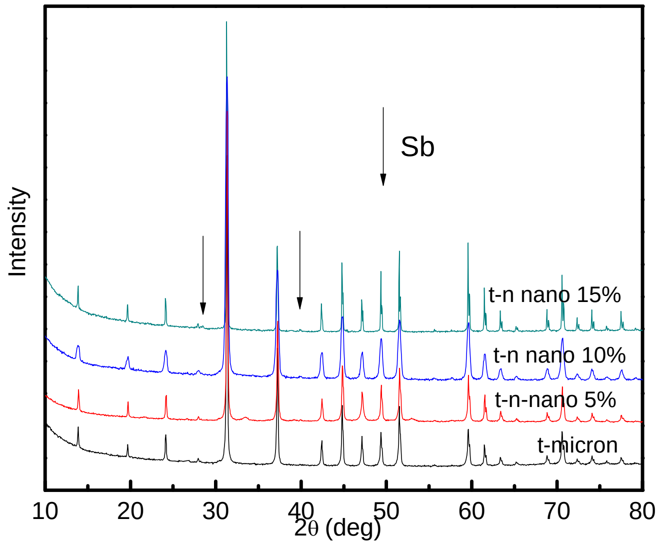

Figure 6.2-1: XRD pattern of the hot pressed n-type nanocomposite sample pellets with $Ni_{1.25}Co_{6.75}Sb_{24}$ as nano-inclusions and $Te_{0.03}Co_{0.97}Sb_3$ as micron-sized matrix.

6.2.2 Microstructure analysis

Figure 6.2-2(a) shows a typical FESEM image of the fracture surface of sample t-micron indicating that the sample consists of only micron-sized grains. Figures 6.2-2(b), (c), (d) correspond to sample t-n nano 5%, t-n nano 10%, t-n nano 15%, indicating that the samples contain both nano-sized and micron-sized grains. They have similar microstructures except for the amount of nano-inclusions distributed among the micron-sized matrix. Similar to that of the p-type nanocomposites, most of these nano-inclusions exist as clusters residing mainly between the micron-sized particles.

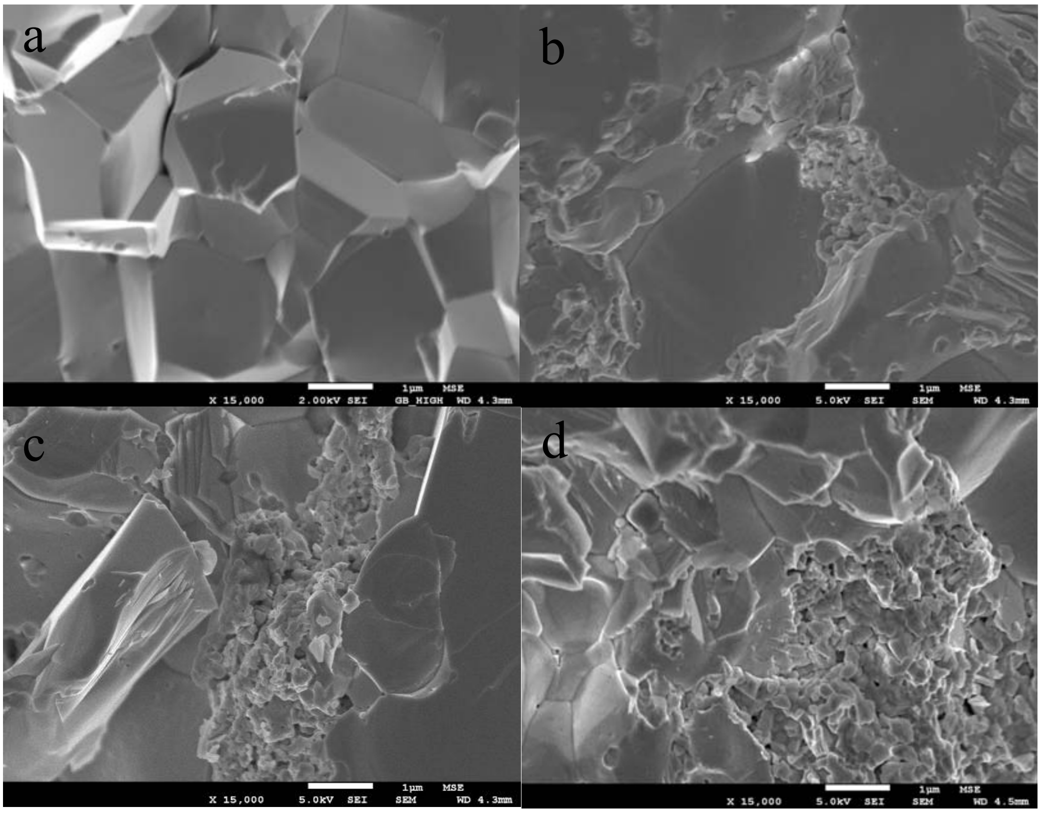

Figure 6.2-2: The typical FESEM images of the fracture surface of t-micron (a), t-n nano 5% (b), t-n nano 10% (c), t-n nano 15% (d).

6.2.3 Electrical properties

6.2.3.1 Carrier concentration

The dependence of the carrier concentration versus the weight percentage of nano-inclusions for the nanocomposite with $Ni_{1.25}Co_{6.75}Sb_{24}$ as nano-inclusions and $Te_{0.03}Co_{0.97}Sb_3$ as micron-sized matrix at room temperature is as shown in Figure 6.2-3. All the carrier concentration values are negative indicating that all the samples are of n-type conduction. The carrier concentrations of micron-sized matrix and nano-inclusion are 8.52×10^{19} cm^{-3} and 5.06×10^{20} cm^{-3} respectively. The carrier concentration of nano-inclusion is moderately higher than that of micron-matrix. The carrier concentrations of nanocomposite samples with Ni-doped $CoSb_3$ nano-inclusions increased as the amount of nano-inclusions increases and are in the level of 10^{20} cm^{-3}. Similar to the results of p-type F-C nanocomposite systems, the carrier concentration of nanocomposite samples is very close to that of matrix due to their comparable carrier concentration between the micron-matrix and nano-inclusions. This agrees with the results of the p-type nanocomposite that the carrier concentration of nanocomposite samples increases after introducing nano-inclusion whose carrier concentration is higher than that of matrix and varies moderately when the micron-sized matrix and nano-inclusion have comparable carrier concentration.

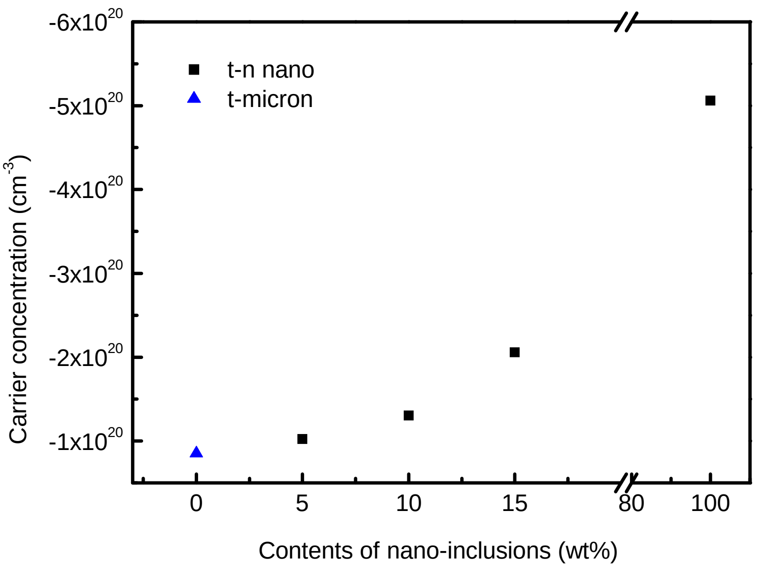

Figure 6.2-3: The dependence of the carrier concentration versus the content of nano-inclusions for the n-type nanocomposite samples with $Ni_{1.25}Co_{6.75}Sb_{24}$ as nano-inclusions and $Te_{0.03}Co_{0.97}Sb_3$ as micron-sized matrix at room temperature.

6.2.3.2 Electrical resistivity

The electrical resistivity plotted as a function of temperature for the nanocomposite samples with various amount of nano-inclusions with $Ni_{1.25}Co_{6.75}Sb_{24}$ as nano-inclusions and $Te_{0.03}Co_{0.97}Sb_3$ as micron-sized matrix are as shown in Figure 6.2-4. The electrical resistivity of all the samples are observed to increase with temperature for the whole temperature range measured, which indicates a metallic behaviour. After mixing, the composite samples (t-n nano 5%, t-n nano 10% and t-n nano 15%), decreases with increasing nano-inclusion contents whose electrical resistivity is smaller than that of micron-sized matrix. In general, the resistivity displays the same trend as the carrier concentration. Similar to the results of carrier concentration, the n- and p-type nanocomposites have the same conclusion that the overall resistivity decreases with content of nano-inclusion when the nano-inclusion has lower resistivity than that of micron-sized matrix and varies moderately when the nano-inclusion and micron-sized matrix have comparable electrical resistivity.

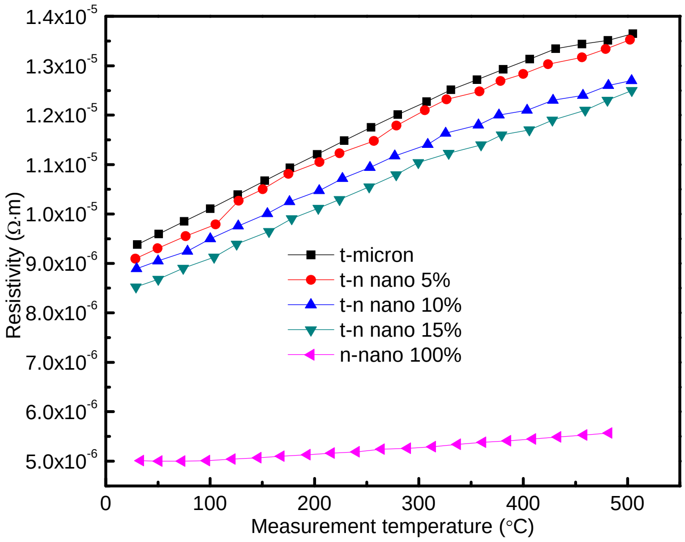

Figure 6.2-4: Temperature dependences of resistivity for the n-type nanocomposite samples with various amount of nano-inclusions with $Ni_{1.25}Co_{6.75}Sb_{24}$ as nano-inclusions and $Te_{0.03}Co_{0.97}Sb_3$ as micron-sized matrix.

6.2.3.3 Seebeck coefficient

The Seebeck coefficient plotted as a function of temperature for the nanocomposite samples with various amount of nano-inclusions with $Ni_{1.25}Co_{6.75}Sb_{24}$ as nano-inclusions and $Te_{0.03}Co_{0.97}Sb_3$ as micron-sized matrix are as shown in Figure 6.2-5. The negative values indicate that the samples are n-type which is in good agreement with the carrier concentration results. The absolute Seebeck values of all the metallic behaviour samples are observed to increase with increasing temperature within the measured temperature range. The n-nano 100% sample possesses the lowest absolute Seebeck coefficient value due to its highest carrier concentration and the impurity of elemental Sb discussed in Chapter 4. Normally, there are three factors to affect the Seebeck coefficient of the final nanocomposite samples, carrier concentration, the Seebeck coefficient value of nano-inclusion and filter effect of nano-inclusions [122]. For our case, the previous two factors have a negative effect on the Seebeck coefficient due to the nano-inclusions having higher carrier concentration but lower absolute value of Seebeck coefficient than that of micron-sized matrix which was already discussed in

Chapter 4. However, the filter effect of nano-inclusion can scatter electron with low energy and increase the absolute value of Seebeck coefficient. The final Seebeck coefficient values of the nanocomposite samples are the results of combining all these three factors. However, these three factors cannot be quantitatively separated. Overall, the nanocomposite samples have very similar Seebeck coefficient values without obvious trend. And similar to the case of p-type F-C nanocomposite system, the Seebeck coefficient values of these nanocomposite samples are closer to the micron-sized matrix than that of nano-inclusion indicating that the high Seebeck coefficient of micron-sized matrix is kind of maintained. Among the composite samples, the t-n nano15% sample possesses the lowest Seebeck coefficient, especially at high temperature range. Here, one can see that further increasing the amount of nano-inclusion does not have a good effect on the Seebeck coefficient.

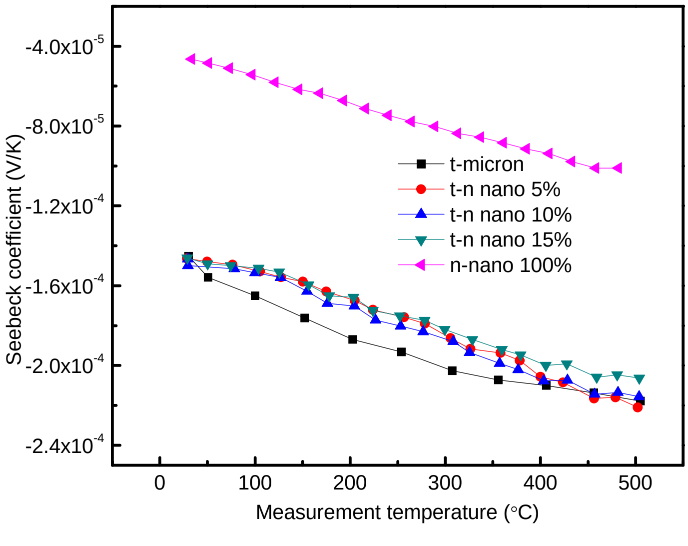

Figure 6.2-5: Temperature dependences of Seebeck coefficient for the n-type nanocomposite samples with various amounts of nano-inclusions with $Ni_{1.25}Co_{6.75}Sb_{24}$ as nano-inclusions and $Te_{0.03}Co_{0.97}Sb_3$ as micron-sized matrix.

6.2.3.4 Power factor

Based on the Seebeck coefficient and electrical resistivity, the power factor (α^2/ρ) of these samples are calculated and are shown in Figure 6.2-6. Due to its relatively low electrical resistivity but high Seebeck coefficient, the sample t-n nano 10% possesses the best electrical property with a maximum power factor of 3.71×10^{-3} $Wm^{-1}K^{-2}$ at about 450 °C. This value is much higher than the value of around 1×10^{-3} $Wm^{-1}K^{-2}$ reported for the nanocomposite samples with the same composition of matrix but undoped n-type $CoSb_3$ as nano-inclusion in Mi's work [77]. Comparing with the nanocomposites in Mi's work, even though the two matrix possess very similar electrical resistivity value, our nano-inclusion with lower electrical conductivity than that of micron-sized matrix reduced electrical resistivity of nanocomposite samples and improve the overall power factor. But for the n-nano 100%, even though it possesses lowest electrical resistivity among all the samples, their carrier concentrations are too high to obtain high Seebeck coefficient and power factor.

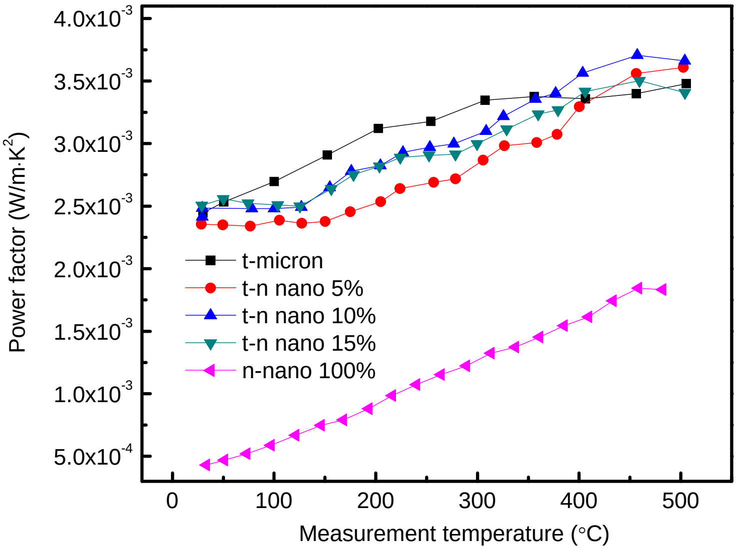

Figure 6.2-6: Temperature dependences of power factor for the n-type nanocomposite samples with various amount of nano-inclusions with $Ni_{1.25}Co_{6.75}Sb_{24}$ as nano-inclusions and $Te_{0.03}Co_{0.97}Sb_3$ as micron-sized matrix.

6.2.4 Thermal properties

Figures 6.2-7(a) and (b) show the total and lattice thermal conductivity for the n-type nanocomposite samples with various amounts of nano-inclusions as a function of temperature. After mixing, both the total and lattice thermal conductivity decrease with increasing amount of nano-inclusions within the measured temperature range which indicates the increased phonon scattering by grain boundaries through the introduction of the nano-inclusions. As compared to the results of Mi's work, the reduction in the total thermal conductivity after nanocompositing in our work is not so obvious. This is due to the high total thermal conductivity of our nano-inclusions. According to Equation (5.6), the much lower thermal conductivity of nano-inclusion than the matrix, the more obvious is the reduction in the final thermal conductivity of nanocomposite samples. Comparing with the thermal conductivity of nano-inclusion in Mi's work (~2 $Wm^{-1}K^{-1}$), the total thermal conductivity of sample n-nano 100% is nearly doubled and too high to reduce the overall total thermal conductivity of nanocomposite samples. The densities of all the samples are in the range of 90% to 92% of the theoretical value and decreases with the increasing nano-inclusion content. From our previous calculation, the effect of similar porosity on the thermal conductivity will not be significant.

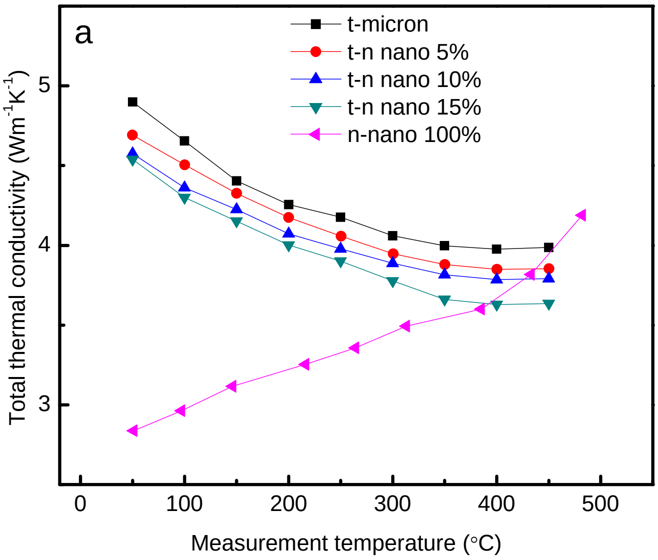

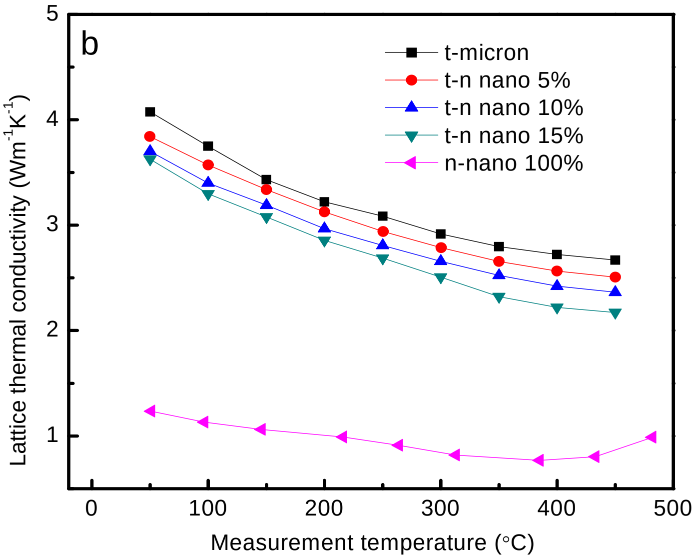

Figure 6.2-7: Temperature dependences of experimental (a) total thermal conductivity and (b) lattice thermal conductivity for the n-type nanocomposite samples with various amount of nano-inclusions with $Ni_{1.25}Co_{6.75}Sb_{24}$ as nano-inclusions and $Te_{0.03}Co_{0.97}Sb_3$ as micron-sized matrix.

6.2.5 Figure-of-merit *ZT* value

With the electrical resistivity, Seebeck coefficient and thermal conductivity results, the dimensionless figure of merit *ZT* values for the samples are calculated and presented in Figure 6.2-8. The highest *ZT* value of 0.71 was attained at about 450 °C for the t-n nano 10% sample which is much higher than that of 0.57 in Mi's work [77]. To the best of my knowledge, this is the highest *ZT* value of unfilled $CoSb_3$. As compared to the t-micron sample, whose highest *ZT* value is 0.59, the value has increased about 20%. The improvement is comparable with other n-type nanocomposite system [125,126]. The reduction in the electrical resistivity as well as maintaining the Seebeck coefficient leads to the remarkable improvement in electrical property. Meanwhile, nano-inclusion also resulted in a reduction in the thermal conductivity. Hence, due to the improvement in both the electrical and thermal properties, the *ZT* values of the T-C nanocomposites are greatly increased.

Within a relatively low content of nano-inclusion (≤10wt%), the *ZT* value increased with the increasing content of nano-inclusion. However, with the content of nano-inclusion further increased, the increase in *ZT* value was not as obvious as that of the relatively low content nano-inclusion samples (sample t-n nano 10% and t-n nano 15% have almost same *ZT* value within the measurement temperature range). Further increasing the amount of nano-inclusion can slightly decrease the thermal conductivity, but the power factor also decrease (the power factor of sample t-n nano 15% is lower than that of t-n nano 10%). The improvement of thermal conductivity is offset by the reduction in the power factor and cannot further increase the overall figure-of-merit *ZT* value.

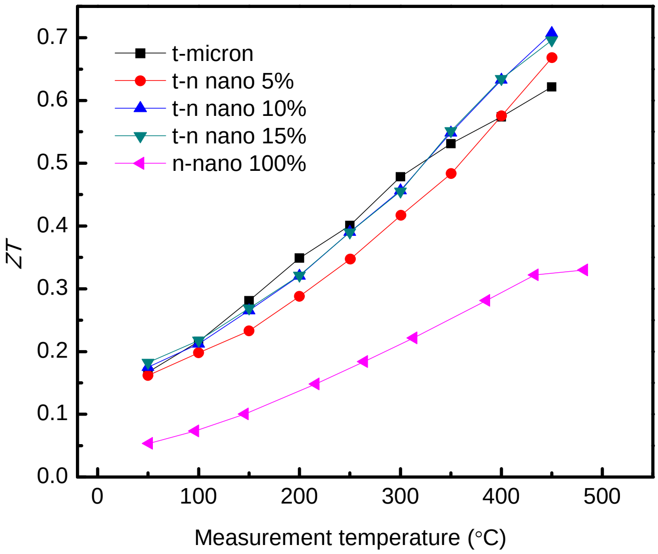

Figure 6.2-8: Temperature dependences of Figure-of-merit *ZT* value of the n-type nanocomposite samples with various amount of nano-inclusions with $Ni_{1.25}Co_{6.75}Sb_{24}$ as nano-inclusions and $Te_{0.03}Co_{0.97}Sb_3$ as micron-sized matrix.

6.3 Conclusions

1. N-type nanocomposites of Te-doped skutterudite matrix ($Te_{0.03}Co_{0.97}Sb_3$) with Ni-doped $CoSb_3$ nano-inclusions ($Ni_{1.25}Co_{6.75}Sb_{24}$) have been prepared. The *ZT* value has

reached to 0.71 at 450 °C for the nanocomposite sample with 10wt% nano-inclusions which is the highest figure-of-merit of unfilled $CoSb_3$ so far.

2. For the electrical properties, the results are very same as that of p-type nanocomposite samples. The overall electrical properties of the nano-composite samples mostly depend on the property difference between the micron-sized matrix and nano-inclusions. When the electrical resistivity of the nano-inclusion is lower than that of micron-sized matrix, the overall resistivity will decrease with the increasing content of nano-inclusion. For nanocomposite samples, Seebeck coefficient did not change too much and the high value of Seebeck coefficient of micron-sized matrix is kind of maintained.

3. For the nano-composite with nano-inclusions whose total and lattice thermal conductivity are smaller than those of the micron-sized matrix, both total thermal conductivity and lattice thermal conductivity decrease with the increasing amount of nano-inclusions which are in a good agreement with the theoretical predictions.

Chapter 7
Conclusions and future work

7.1 Conclusions

The goal of this work is to improve the overall thermoelectric properties i.e. Figure-of-merit *ZT* value of $CoSb_3$-based materials through nanocomposite method. Both p- and n-type $CoSb_3$-based nanocomposites were prepared. The results showed that the nanocomposite approach is effective in reducing thermal conductivity through the introduction of nano-inclusions with high density of grain boundaries. Meanwhile, it was found that the difference in electrical properties between the nano-inclusion and micron-sized matrix can play an important role on the final properties of the nanocomposite samples. The main conclusions are reached as followed:

Nano-particles were first synthesized to be used as the nano-inclusions in the nanocomposites. High purity p-type undoped $CoSb_3$ nanoparticles were successfully synthesized via a polyol process at a relative low temperature, which is a rapid, one-pot synthesis route. The optimized reaction conditions were determined to be at a temperature of 195 °C for 15 mins. The average particle-size of as-synthesized nano-powders is around 30 nm which is smaller than the reported particle-size of around 100 nm obtained by solvothermal method. The polyol method was also applied to synthesize doped $CoSb_3$. N-type Ni-doped $CoSb_3$ nanoparticles were successfully synthesized under the same reaction conditions. After doping, the electrical resistivity has been greatly reduced with major carrier changed. The electrical resistivity of sample $Ni_{1.25}Co_{6.75}Sb_{24}$ is as low as 5×10^{-6} Ω·m which is comparable with the value of metal ($\times10^{-7}$ Ω·m). However, comparing with the electrical resistivity, doping has less impact on absolute value of Seebeck coefficient. In addition, due to the introduced dopants, the lattice thermal conductivity of the Ni-doped samples was also reduced as compared to the undoped samples. And the lowest lattice thermal conductivity of sample $Ni_{1.5}Co_{6.5}Sb_{24}$ is 0.64 W/m·K which is very near the lowest theoretical lattice thermal conductivity of ~0.3 W/m·K. As a result, the highest *ZT* value of sample $Ni_{1.25}Co_{6.75}Sb_{24}$ reached 0.33, which is nearly 4 times higher than that of undoped $CoSb_3$ (highest *ZT* value is only 0.067).

To investigate the effect of nano-inclusion on the final thermoelectric properties of nanocomposite, three different types of p-type nanocomposites were prepared. For thermal properties, both total thermal conductivity and lattice thermal conductivity decrease with increasing amount of nano-inclusions. In order to reduce the effective thermal conductivity of the mixed nanocomposite, the nanostructure with lower thermal conductivity than that of the matrix, and preferably much lower than the matrix phase is a good candidate to be used as nano-inclusion. For the overall electrical properties of nanocomposite, the cases are more complicated. When the carrier concentration (resistivity) of nano-inclusion is much lower (higher) than that of micron-sized matrix, the nano-inclusion has a negative effect on the power factor of nanocomposite samples. When the nano-inclusion and micron-sized matrix have comparable carrier concentration or resistivity, the improvement in the power factor is not obvious. However, when the carrier concentration (resistivity) of nano-inclusion is much higher (lower) than that of micron-sized matrix, comparing to the matrix, the values of power factor of nanocomposites have increased greatly. Hence, in order to improve the electrical properties, the nano-inclusion must possess much high carrier concentration or much lower resistivity than that of micron-sized matrix. Combined with thermal properties, we can conclude that the nanostructures with much higher (lower) carrier concentration (resistivity) and much lower thermal conductivity than that of micron-sized matrix are the most suitable for use as nano-inclusions. For the nanocomposites with the same percentage of same type of nano-inclusions, the nano-inclusions with a smaller size gives a better performance on the final thermoelectric properties of nanocomposites.

Besides p-type nanocomposite, N-type nanocomposite was also prepared. The results of n-type nancomposite are in a good agreement with the conclusion of p-type nanocomposites. The highest *ZT* value has reached to 0.71 at 450 °C for the n-type nanocomposite sample with 10wt% nano-inclusions which is the highest figure-of-merit of unfilled $CoSb_3$ so far.

7.2 Future work

This work has illustrated the interests of following works:

1. Multiple doping

The results of Ni-doped $CoSb_3$ indicate both electrical resistivity and lattice thermal conductivity have been greatly reduced after substitution of Co by Ni. The dopant can bring extra electron to the conduction band and meanwhile cause point defect in lattice to improve both electrical and thermal properties. In addition to n-type doping, Fe is a promising p-type dopant substituting at Co site, since it has one less electron than Co at outer shell but similar valence radii and electronegativities. Similar to substitution at Co site, doping at Sb site can also reduce the electrical resistivity and lattice thermal conductivity in the same way. Furthermore, substitution of Co and Sb at the same is even more effective to improve the overall thermoelectric properties of $CoSb_3$. Meanwhile the introduction of second dopant may compensate the distortion caused by the first dopant and result in a more stable crystal structure. The multiple doping can be achieved by polyol method.

2. Thick film nanocomposite

Besides bulk materials, thick film also shows great potential for the application of thermoelectric device. Based on our study, the thick film nanocomposite is promising to improve the thermoelectrical properties of $CoSb_3$-based materials. Pulsed laser deposition (PLD) has already been proven to be a successful processing in high-quality film preparing. The nano-inclusion can be periodically and uniformly embedded into the micron-sized matrix film by controlling the deposition condition. The weight percentages and distribution site of nano-inclusion need to be optimized in order to achieve high TE performance of $CoSb_3$-based thick film nanocomposites.

References:

[1] Jaumot, F.E., *Proceedings of the IRE,* vol. 46, 538-554, 1958.

[2] Riffat, S. b. and Ma, X. L., *Applied Thermal Engineering,* vol. 23, 913-935, 2003.

[3] Riffat, S. b. and Ma, X. L., *International Journal of Energy Research,* vol. 28, 753-768, 2004.

[4] Rowe, D. M., *Renewable Energy,* vol. 5, 1470-1478, 1994.

[5] Rowe, D. M., "Thermoelectrics handbook: macro to nano," CRC/Taylor & Francis, 2006.

[6] Nolas, G. S., Cohn, J. L., and Slack, G. A., *Physical Review B,* vol. 58(1), 164-170, 1998.

[7] Rowe, D. M., "CRC handbooks of thermoelectrics," CRC press, Boca Raton FL, 1995.

[8] Caillat, T., Fleurial, J. P., and Borshchevsky, A., *15th International Conference on thermoelectric,* 100-106, 1996.

[9] Nolas, G. S., Morelli, D. T., and Tritt, T. M., *Annual Review of Materials Science,* vol. 29, 89-116, 1999.

[10] Zhang, B., He, J., Ji, X. H., Terry, M. T., and Amar, K., *Applied Physics Letters,* vol. 89, 163114, 2006.

[11] Zhao, X. B., Ji, X. H., Zhang, Y. H., Zhu, T. J., Tu, J. P., and Zhang, X. B., *Applied Physics Letters,* vol. 86, 062111, 2005.

[12] Goldsmid, H. J., "Thermoelectric Refrigeration, " New York: Plenum Press, 1964.

[13] Terry, M. T., *MRS Bulletin,* vol. 31, 188-194, 2006.

[14] Garrido, J., *Journal of Phyics: Condensed Matter,* vol. 21, 155802, 2009.

[15] Ioffe, A. F., "Semiconductor thermoelements and thermoelectric cooling," London: Infosearch, 1957.

[16] Snyder, S. J., and Toberer, E. S., *Nature Materials,* vol. 7, 105-114, 2008.

[17] Goldsmid, H. J., "Thermoelectric Refrigeration, " London: Pion Limited, 1986.

[18] Zhao, Xueying, PhD thesis, Shanghai Institute of Ceramics, Chinese Academy of Sciences, 2006.

[19] Sootsman, J. R., Chung, D. Y., and Kanatzidis, M. G., *Angewandte Chemie International Edition,* Vol 48, 8616-8639, 2009.

[20] Kim, W., Zide, J., Gossard, A., Klenov, D., Stemmer, S., Shakouri, A., and Majumdar, A., *Physical Review Letters,* vol. 96, 045901, 2006.

[21] Snyder, J. G., and Ursell, T. S., *Physical Review Letters,* vol. 91, 148301, 2003.

[22] Chung, D. Y., Hogan, T. P., Rocci-Lane, M., Brazis, P., Ireland, J. R., Kannewurf, C. R., Bastea, M., Uher, C., and Kanatzidis, M. G., *Journal of American Chemical Society*, vol. 126, 6414-6428, 2004.

[23] Chung, D. Y., Hogan, T. P., Brazis, P., Rocci-Lane, M., Kannewurf, C., Bastea, M., Uher, C., and Kanatzidis, M. G., *Science*, vol. 287, 1024-1027, 2000.

[24] Vedernikov, M. V., Kutasov, V. A., Luk'yanova, L. N., and Konstantinov, P. P., “Optimization of (Bi,Sb)2(Te,Se)3 - based thermoelectrics for low-temperature applications,” *16th International Conference on Thermoelectrics,* 1997.

[25] Yamashita, O, and Sugihara, S., *Journal of Materials Science*, Vol. 40, 6439-6444, 2005.

[26] Caillat, T., J. Fleurial, J., and Borshchevsk, A., *Journal of Physics and Chemistry of Solids*, vol. 58, 1119-1125, 1997.

[27] Poudeu, P., D'Angelo, J., Downey, A. D., Short, J. L., Hogan, T. P., and Kanatzidis M. G., *Angewandte Chemie International Edition,* Vol. 45, 3835-3839, 2006.

[28] Androulakis, J., Hsu, K-F., Pcionek, R., Kong, H., Uher, C., D'Angelo, J.J., Downey, A., T. Hogan, T., and Kanatzidis M. G., *Advanced Materials*, vol. 18(9), 1170-1173, 2006.

[29] Hsu, K-F., Loo, S., Guo, F., Chen, W., Dyck, J. S., Uher, C., Hogan, T., Polychroniadis, E. K., and Kanatzidis M. G., *Science,* vol. 303. 818 – 821, 2004.

[30] Androulakis, J., Lin, C.-H., Kong, Uher, C., Wu, C.-I., Hogan, T., Cook, B.A., Caillat, T., Paraskevopoulos, K.M., and Kanatzidis M. G., *Journal of American Chemical Society,* Vol. 129(31); 9780-9788, 2007.

[31] Caillat, T., Borshchevsky, S., Snyder, J., Fleurial J-P.,El-Genk, M., editor. *Proceedings of Space Technology and Applications International Forum.* AIP Conference Proceedings No. 504. Melville, NY: American Institute of Physics, 1508-1512, 2000.

[32] Goldsmid, H. J., and Nolas, G. S., *20th International Conference on Thermoelectrics,* 1-6, 2001.

[33] Dismukes, J. P., Ekstrom, L., Steigmeier, E. F., Kudman, I. ,and Beers, D. S., *Journal of Applied Physics,* vol. 35, 2899-2907, 1964.

[34] http://chemgroups.northwestern.edu/kanatzidis/greatthermo.html

[35] Dresselhaus, M. S., Chen, G., Tang, M. Y., Yang, R., Lee, H., Wang, D., Ren Z., FLeurial, J-P., and Gogna, P., *Advanced Materials,* vol. 19, 1043-1053, 2007.

[36] Fleurial, J. P., Caillat, T., and Borshchevsky, A., *19th International Conference on Thermoelectrics*, 1-11, 2007.

[37] Uher, C., *32nd International Conference on Thermoelectrics*, 42-47, 2003.

[38] Uher, C., *Recent Trends in Thermoelectric Materials Research I.* vol. 69, 139-253, 2001.

[39] Uher, C., *21st International Conference on thermoelectric*, 35-41, 2002.

[40] Pauling, L., *Nature of the chemical bond*. New York: Cornell University Press, 1960.

[41] Chen, G., Dresselhaus, M. S., Dresselhaus, G., Fleurial, J. P., and Caillat, T., *International Materials Reviews,* vol. 48, 45-66, 2003.

[42] Caillat, T., Fleurial, J. P., and Borshchevsky, A., *Journal of Crystal Growth,* vol. 166, 722-726, 1996.

[43] Sales, B. C., *International Journal of Applied Ceramic Technology,* vol. 4, 291-296, 2007.

[44] Anno, H., and Matsubara, K., *Journal of the Japan Institute of Metals,* vol. 63, 1407-1411, 1999.

[45] Shi, X., Zhou, Z., Zhang, W., Chen, L. D., Yang, J., and Uher, C., *Journal of Applied Physics,* vol. 101, 123525, 2007.

[46] Shi, X., Chen, L., Yang, J., and Meisner, G. P., *Applied Physics Letters,* vol. 84, 2301-2303, 2004.

[47] Mi, J. L., Zhao, X. B., Zhu, T. J., and Ma, J., *Journal of Alloys and Compounds,* vol. 452, 225-229, 2008.

[48] Mandrus, D., Migliori, A., Darling, T. W., Hundley, M. F., Peterson, E. J., and Thompson, J. D., *Physical Review B,* vol. 52, 4926-4931, 1995.

[49] Yang, J., Morelli, D. T., Meisner, G. P., Chen, W., Dyck, J. S., and Uher, C., *Physical Review B,* vol. 65, 094115, 2002.

[50] Katsuyama, S., Shichijo, Y., Ito, M., Majima, K., and Nagai, H., *Journal of Applied Physics,* vol. 84, 6708-6712, 1998.

[51] Dyck, J. S., Chen, W., Yang, J. H., Meisner, G. P., and Uher, C., *Physical Review B,* vol. 65, 115204, 2002.

[52] Yang, J., Meisner, G. P., Morelli, D. T., and Uher, C., *Physical Review B,* vol. 6301, 014410, 2001.

[53] Anno, H., Tashiro, H., and Matsubara, K., 18th *International Conference on thermoelectrics*, 169-172, 1999.

[54] Zhou, Z. H., Uher, C., Jewell, A., and Caillat, T., *Physical Review B,* vol. 71, 235209, 2005.

[55] Sales, B. C., Mandrus, D., and Williams, R. K., *Science,* vol. 272, 1325-1328, 1996

[56] Xue, Y. J., Liu, K. G., Lia, J. H., and Chen, N., *Materials Research Bulletin,* vol. 40, 1172-1176, 2005.

[57] Braun D. J., and Jeitschko, W., *Journal of the Less Common Metals,* vol. 72, 147-156, 1980.

[58] Nolas, G. S., Cohn, J. L., and Slack, G. A. *Physical Review B,* vol. 58, 164-170, 1998.

[59] Nolas, G. S., Fowler, G., and Yang, J., *Journal of Applied Physics,* vol. 100, 043705, 2006.

[60] Meisner, G. P., Morelli, D. T., Hu, S., Yang, J., and Uher, C., *Physical Review Letters,* vol. 80, 3551-3554, 1998.

[61] Salvador, J. R., Yang, J., Shi, X., Wang, H., Wereszczak, A. A., Kong, H., and Uher, C., *Philosophical Magazine*, vol. 89, 1517, 2009.

[62] Salvador, J. R., Yang, J., Wang, H., Shi, X., *Journal of Applied Physics*, vol. 107, 043705, 2010.

[63] Bai, S. Q., Shi, X., and Chen, L. D., *Applied Physics Letter,* vol. **96**, 202102, 2010.

[64] Zhao, W., Wei, P., Zhang, Q., Dong, C., Liu L., and Tang, X., *Journal of the American Chemical Society*, vol. 131 (10), 3713-3720, 2009.

[65] Toprak, M. S., Stiewe, C., Platzek, D., Williams, S., Bertini, L., Muller, E. C., Gatti, C., Zhang, Y., Rowe, M., and Muhammed, M., *Advanced Functional Materials,* vol. 14, 1189-1196, 2004.

[66] Yang, L., Hng, H. H., Cheng, H., Sun, T., and Ma, J., *Materials Letters,* vol 62, 2483-2485, 2008.

[67] Wojciechowski M. J., *the 22nd international conference on thermoelectric,* 97-100, 2003.

[68] Wang, M., Zhang, Y., and Muhammed, M., *Nanostructured Materials,* vol. 12, 237-240, 1999.

[69] Chu, Y., Tang, X. F., Zhao, W. Y., and Zhang, Q. J., *Crystal Growth & Design,* vol. 8, 208-210, 2008.

[70] Mi, J. L., Zhao, X. B., Zhu, T. J., and Ma, J., *Journal of Applied Physics,* vol. 101, 054314, 2007.

[71] Zheng, X. J., Zhu, L. L., and Zhou, Y. H., *Applied Physics Letters,* vol. 87, 00036951, 2005.

[72] Yu, B. L., Tang, X. F., Zhang, Q. J., *22nd International Conference on thermoelectric,* 101-104, 2003.

[73] He, Z. M., Stiewe, C., Platzek, D., Karpinski, G., Muller, E., Li, S. H., Toprak, M., and Muhammed, M., *Journal of Applied Physics,* vol. 101, 235602, 2007.

[74] Alboni, P. N., Ji, X., He, J., Gothard, N., Hubbard, J., and Tritt, T. M., *Journal of Electronic Materials,* vol. 36, 711-715, 2007.

[75] He, Z. M., Stiewe, C., Platzek, D., Karpinski, G., Mueller, E., Li, S. H., Toprak, M., and Muhammed, M., *Nanotechnology,* vol. 18, 235602, 2007.

[76] Ji, X., He, J., Alboni, P., Su, Z., Gothard, N., Zhang, B., Tritt, T. M., and Kolis, J. W., *Physica Status Solidi-Rapid Research Letters,* vol. 1, 229-231, 2007.

[77] Mi, J. L., Zhao, X. B., Zhu, T. J., and Tu, J. P., *Applied Physics Letters,* vol. 91, 172116, 2007.

[78] Zhao, X. B., Ji, X. H., Zhang, Y. H., Zhu, T. J., Tu, J. P., and Zhang, X. B., *Applied Physics Letters,* vol. 86, 2005.

[79] Mi, J. L., Zhao, X. B., Zhu, T. J., Tu, J. P., and Cao, G. S., *Journal of Alloys and Compounds,* vol. 417, 269-272, 2006.

[80] Ni, H. L., Zhu, T. J., and Zhao, X. B., *Physica B,* vol. 364, 50-54, 2005.

[81] Sun, T., Zhao, X. B., Zhu, T. J., and Tu, J. P., *Materials Letters,* vol 60, 2534-2537, 2006.

[82] Sun, T., Zhu, T. J., and Zhao, X. B., *Acta Chimica Sinica*, vol 63, 1515-1519, 2005.

[83] Zheng, Y. Y., Zhu, T. J., Zhao, X. B., Tu, J. P., and Cao, G. S., *Materials Letters,* vol 59, 2886-2888, 2005.

[84] Ni, H. L., Zhao, X. B., Zhu, T. J., Ji, X. H., and Tu, J. P., *Journal of Alloys and Compounds*. vol. 397, 317-321, 2005.

[85] Poudel, B., Hao, Q., Ma, Y., Lan, Y. C., Minnich, A., Yu, B., Yan, X. A., Wang,D. Z., Muto, A., Vashaee, D., Chen, X. Y., Liu, J. M., Dresselhaus, M. S., Chen, G., and Ren, Z. F., *Science,* vol. 320, 634-638, 2008.

[86] Li, J. F., Liu, W. S., Zhao, L. D., and Zhou, M., *NPG Asia Materials,* vol. 2(4), 152-158, 2010.

[87] Zhao, L. D., Zhang, B. P., Liu, W. S., Li, J. F., *Journal of Applied Physics,* vol. 105, 023704, 2009.

[88] Zhang, B. He, J., Ji, X., Terry, M. T., and Amar, K., *Applied Physics Letters,* vol. 89, 163114, 2006.

[89] Stiewe, C., He, Z., Platzek, D., Karpinski, G., Muller, E., Li, S., Toprak, M., and Muhammed, M., *Materialwissenschaft Und Werkstofftechnik,* vol. 38, 773-776, 2007.

[90] Zhao, X. Y., Shi, X., Chen, L. D., Zhang, W. Q., Bai, S. Q., Pei, Y. Z., Li, X. Y., and Goto, T., *Applied Physics Letters,* vol. 89, 092121, 2006.

[91] Alleno, E., Chen, L., Chubilleau, C., Lenoir, B., Rouleau, O., Trichet, M. F., and Villeroy, B., *Journal of Electronic Materials*, vol. 39, 1966-1970, 2010.

[92] Xiong, Z., Chen, X., Zhao, X., Bai, S., Huang, X., and Chen, L., *Solid State Science*, vol. 11, 1612-1616, 2009.

[93] Katsuyama, S., Kanayama, Y., Ito, M., Majima, K., and Nagai, H., *Journal of Applied Physics,* vol. 88, 3484-3489, 2000.

[94] Luo, X., Li, Z., Yuan, C., and Chen, Y., *Materials Chemistry and Physics,* vol. 128, 77-82, 2011.

[95] Park, K. H., Im, S. H., and Park, O. O., *Nanotechnology,* vol. 22, 045602, 2011.

[96] Lim, B., and Xia, Y., *Angewandte Chemie International Edition,* vol. 50, 76-85, 2011.

[97] Wu, C. W., Mosher, B. P., Lyons, K., and Zeng, T. F., *Journal of Nanoscience and Nanotechnology*, vol. 10, 2342-2347, 2010.

[98] Md, J. A., Masaharu, and T., Mika, M., *Bulletin of the Chemical Society of Japan,* vol. 83, 92-100, 2010.

[99] Yuan, Q., and Wang, X., *Nanoscale*, vol. 2, 2328-2335, 2010.

[100] Anucha Watchrapasorn, Phd Thesis, Stanford University, 2003.

[101] Liu, W. S., Zhang, B. P., Li, J. F., and Liu, J., Acta Physica Sinica, vol. 55, 465-471, 2006.

[102] Wang, M., Zhao, H., He, J., Wang, R., Chen, J., and Chen, Ni., *Journal of Alloys and Compounds*, vol. 484, 864-869, 2009.

[103] Zhang, Y., Li, C., Du, Z., and Geng, T., *Computer coupling of Phase Diagrams and Thermochemistry*, vol. 32, 56-63, 2008.

[104] Pongsaton, A., Sumetha, S., Tanakorn, R., and Tanattha, R., *Journal of Alloys and Compounds*, vol. 501, 100-103, 2010.

[105] Li, H., Yabuuchi, N., Meng, Y. S., Kumar, S., Breger, J., Grey, C. P., and Yang, S. H., *Chemistry of Materials,* vol. 19, 2551-2565, 2007.

[106] Williams, J. R., and Johnson, D. C., Inorganic Chemistry, vol. 41, 4127-4130, 2002.

[107] Itoh, T., and Isogai, K., *Materials Research Society Symposium Proceedings,* vol. 1166, N03-16, 2009.

[108] Liu, W. S., Zhang, B. P., Li, J. F., and Zhao, L. D., *Journal of Physics D: Applied Physics,* vol. 40, 6784-6790, 2007.

[109] He, Q., Hao, Q., Wang, X., Yang, J., Lan, C., Yan, X., Yu, B., Ma, Y., Poudel, B., Joshi, G., Wang, D., and Chen, G., Journal of Nanoscience and Nanotechnology, vol. 8, 4003-4006, 2008.

[110] Pichanusakorn, P., and Bandaru, P., *Materials Science & Engineering R-Reports*, vol. 67, 19-63, 2010.

[111] Heremans, J. P., Jovovic, V., Toberer, E. S., Saramat, A., Kurosaki, K.,Charoenphakdee, A., Yamanaka, S., and Snyder, G. J., *Science*, vol. 321, 554-557, 2008.

[112] Takeuchi, T., Kondo, T., Takami, T., Takahashi, H., Ikuta, H., Mizutani, U., Soda, K., Funahashi, R., Shikano, M., Mikami, M., Tsuda, S., Yokoya, T., Shin, S., and

Muro, T., *Physics Review B*, vol. 69, 125410, 2004.

[113] Yang, C. C., and Li, S., *Journal of Electronic Materials,* DOI: 10.1007/s11664-010-1467-y, 2010.

[114] Omar, M. S., and Taha, H. T., *Sahana*, vol. 35, 177-193, 2010.

[115] Liu, W. S., Zhang, B. P., Zhao, L. D., and Li, J. F., *Chemistry of Materials*, vol. 20, 7526-7531, 2008.

[116] Qiu, P., Shi, X., Chen, X., Huang, X., Liu, R., and Chen, L., *Journal of Alloys and Compounds*, vol. 509, 1101-1105, 2011.

[117] Yang, J., Morelli, D. T., Meisner, G. P., Chen, W., Dyck, J. S., and Uher, C., *Physical Review B,* vol. 65, 094115, 2002.

[118] Puyet, M., Candolfi, C., Chaput, L., Dos, V. A., Dauscher, A., Lenoir, B., and Hejtmanek, J., *Journal of Physics: Condensed Matter,* vol. 18, 11301-11308, 2006.

[119] Kim, M. J., You, S. W., Ur, S. C., and Kim, I. H., *25th International Conference on thermoelectric,* 439-442, 2006.

[120] Durkan. C, and Welland. M. E., *Physical Review B*, vol. 61, 14215, 2000.

[121] Pei, J., Chen, G., Lu, D. Q., Liu, P. S., and Zhou, N., *Solid State Communication*, vol. 146, 283-286, 2008.

[122] He, Z. M., Stiewe, C., Platzek, D., Karpinski, G., Muller, E., Li, S. H., Toprak, M., and Muhammed, M., *Journal of Applied Physics*, vol. 101, 2007.

[123] Lawrence, W.E., and Wilkins, J. W., *Physics Review B*, vol.7, 2317-2332, 1973.

[124] Yang Kai, Phd Thesis, Nanyang Technological University, 2010.

[125] Mi, J. L., Zhao, X. B., Zhu, T. J., and Tu, J. P., *Journal of Physics D: Applied Physics,* vol. 41, 205403, 2008.

[126] Alboni, P. N., Ji, X., He, J., Gothard, N., and Tritt, T. M., *Journal of Applied Physics*, vol. 103, 113707, 2008.

[127] Keblinski, P., Phillpot, S. R., Choi, S. U. S., and Eastman, J. A., *International Journal of Heat and Mass Transfer*, vol. 45, 855, 2002.

[128] Hamilton, R. L., and Crosser, O. K. *I&EC. Fundamentals,* Vol. 1, 187, 1962.

[129] Durkan. C, and Welland. M. E., *Physical Review B*, vol. 61, 14215, 2000.

Publication list

- 1.**Yang L**, Hng HH, Ma J, et al. JOURNAL OF ELECTRONIC MATERIALS Volume: 39 Issue: 9 Pages: 1543-1548 Published: SEP 2010
- 2. **Yang L**, Hng HH, Li D, et al. JOURNAL OF APPLIED PHYSICS Volume: 106 Issue: 1 Article Number: 013705 Published: JUL 1 2009
- 3. **Yang L**, Hng HH, Cheng H, et al. MATERIALS LETTERS Volume: 62 Issue: 15 Pages: 2483-2485 Published: MAY 31 2008
- 4. **Yang L**, Hug HH, Sun T, et al. 26th International Conference on Thermoelectrics (ICT'07), JUN 03-05, 2007 Jeju Isl, SOUTH KOREA

  Book Series: International Conference on Thermoelectrics Pages: 188-190 Published: 2008
- 5. **Yang L**, Hng HH, Sun T, et al.4th International Conference on Materials for Advanced Technologies, JUL 01-06, 2007 Singapore, SINGAPORE

  Book Series: SOLID STATE PHENOMENA Volume: 136 Pages: 57-61 Published: 2008